

Density Model for Risso's Dolphin (*Grampus griseus*) for the U.S. East Coast: Supplementary Report

Model Version 5.1

Duke University Marine Geospatial Ecology Laboratory*

2023-05-27


Citation

When citing our methodology or results generally, please cite Roberts et al. (2016, 2023). The complete references appear at the end of this document. We are preparing a new article for a peer-reviewed journal that will eventually replace those. Until that is published, those are the best general citations.

When citing this model specifically, please use this reference:

Roberts JJ, Yack TM, Cañadas A, Fujioka E, Halpin PN, Barco SG, Boisseau O, Chavez-Rosales S, Cole TVN, Cotter MP, Cummings EW, Davis GE, DiGiovanni Jr. RA, Garrison LP, Gowan TA, Jackson KA, Kenney RD, Khan CB, Lockhart GG, Lomac-MacNair KS, McAlarney RJ, McLellan WA, Mullin KD, Nowacek DP, O'Brien O, Pabst DA, Palka DL, Quintana-Rizzo E, Redfern JV, Rickard ME, White M, Whitt AD, Zoidis AM (2022) Density Model for Risso's Dolphin (*Grampus griseus*) for the U.S. East Coast, Version 5.1, 2023-05-27, and Supplementary Report. Marine Geospatial Ecology Laboratory, Duke University, Durham, North Carolina.

Copyright and License

 This document and the accompanying results are © 2023 by the Duke University Marine Geospatial Ecology Laboratory and are licensed under a [Creative Commons Attribution 4.0 International License](https://creativecommons.org/licenses/by/4.0/).

Model Version History

Version	Date	Description
1	2014-10-19	Initial version.
2	2014-11-21	Reconfigured detection hierarchy and adjusted NARWSS detection functions based on additional information from Tim Cole. Removed CumVGPM180 predictor. Updated documentation.
3	2014-12-05	Fixed bug that applied the wrong detection function to segments NE_narwss_1999_widgeon_hapo dataset. Refitted model. Updated documentation.
3.1	2015-03-06	Updated the documentation. No changes to the model.
3.2	2015-05-14	Updated calculation of CVs. Switched density rasters to logarithmic breaks. No changes to the model.
3.3	2016-04-21	Switched calculation of monthly 5% and 95% confidence interval rasters to the method used to produce the year-round rasters. (We intended this to happen in version 3.2 but I did not implement it properly.) No changes to the other rasters or the model itself. Model files released as supplementary information to Roberts et al. (2016).

*For questions or to offer feedback please contact Jason Roberts (jason.roberts@duke.edu) and Tina Yack (tina.yack@duke.edu)

(continued)

Version	Date	Description
4	2018-04-14	Began update to Roberts et al. (2015) model. Introduced new surveys from AMAPPS, NARWSS, UNCW, VAMSC, and the SEUS NARW teams. Updated modeling methodology. Refitted detection functions and spatial models from scratch using new and reprocessed covariates. Model released as part of a scheduled update to the U.S. Navy Marine Species Density Database (NMSDD).
5	2022-06-20	This model is a major update over the prior version, with substantial additional data, improved statistical methods, and an increased spatial resolution. It was released as part of the final delivery of the U.S. Navy Marine Species Density Database (NMSDD) for the Atlantic Fleet Testing and Training (AFTT) Phase IV Environmental Impact Statement. Several new collaborators joined and contributed survey data: New York State Department of Environmental Conservation, TetraTech, HDR, and Marine Conservation Research. We incorporated additional surveys from all continuing and new collaborators through the end of 2020. (Because some environmental covariates were only available through 2019, certain models only extend through 2019.) We increased the spatial resolution to 5 km and, at NOAA's request, we extended the model further inshore from New York through Maine. We reformulated and refitted all detection functions and spatial models. We updated all environmental covariates to newer products, when available, and added several covariates to the set of candidates. For models that incorporated dynamic covariates, we estimated model uncertainty using a new method that accounts for both model parameter error and temporal variability.
5.1	2023-05-27	Completed the supplementary report documenting the details of this model. Corrected the 5 and 95 percent rasters so that they contain the value 0 where the taxon was assumed absent, rather than NoData. Nothing else was changed.

1 Survey Data

We built this model from data collected between 1998-2019 (Table 1, Figure 1). In keeping with our primary strategy for the 2022 modeling cycle, we excluded data prior to 1998 in order to utilize biological covariates derived from satellite ocean color observations, which were only available for a few months before 1998. We excluded data after 2019 in order to utilize micronekton biomass estimates from SEAPODYM (Lehodey et al. 2008), distance to eddies, and kinetic energy covariates, which preliminary modeling indicated were effective spatial covariates, but were only available through 2019. We restricted the model to aerial survey transects with sea states of Beaufort 5 or less (for a few surveys we used Beaufort 4 or less) and shipboard transects with Beaufort 5 or less (for a few we used Beaufort 4 or less). We also excluded transects with poor weather or visibility for surveys that reported those conditions.

Table 1: Survey effort and observations considered for this model. Effort is tallied as the cumulative length of on-effort transects. Observations are the number of groups and individuals encountered while on effort. Off effort observations and those lacking an estimate of group size or distance to the group were excluded.

Institution	Program	Period	Effort	Observations		
			1000s km	Groups	Individuals	Mean Group Size
Aerial Surveys						
HDR	Navy Norfolk Canyon	2018-2019	11	38	971	25.6
NEAq	CNM	2017-2019	2	40	761	19.0
NEAq	MMS-WEA	2017-2019	31	0	0	
NEAq	NLPSC	2011-2015	43	2	2	1.0
NEFSC	AMAPPS	2010-2019	83	93	463	5.0
NEFSC	NARWSS	2003-2016	380	108	618	5.7
NEFSC	Pre-AMAPPS	1999-2008	45	141	1,161	8.2
NJDEP	NJEBS	2008-2009	9	0	0	
NYS-DEC/TT	NYBWM	2017-2019	74	161	1,821	11.3
SEFSC	AMAPPS	2010-2019	110	62	653	10.5
SEFSC	MATS	2002-2005	27	0	0	
UNCW	Navy Cape Hatteras	2011-2017	34	21	273	13.0
UNCW	Navy Jacksonville	2009-2017	92	48	744	15.5
UNCW	Navy Norfolk Canyon	2015-2017	14	16	316	19.8
UNCW	Navy Onslow Bay	2007-2011	49	5	28	5.6
VAMSC	MD DNR WEA	2013-2015	15	0	0	
VAMSC	Navy VACAPES	2016-2017	19	0	0	
VAMSC	VA CZM WEA	2012-2015	21	0	0	
		Total	1,059	735	7,811	10.6
Shipboard Surveys						
MCR	SOTW Visual	2012-2019	8	3	16	5.3
NEFSC	AMAPPS	2011-2016	15	325	1,982	6.1
NEFSC	Pre-AMAPPS	1998-2007	10	251	2,323	9.3
SEFSC	AMAPPS	2011-2016	16	31	290	9.4
SEFSC	Pre-AMAPPS	1998-2006	30	89	1,251	14.1
		Total	80	699	5,862	8.4
		Grand Total	1,139	1,434	13,673	9.5

Table 2: Institutions that contributed surveys used in this model.

Institution	Full Name
HDR	HDR, Inc.
MCR	Marine Conservation Research
NEAq	New England Aquarium
NEFSC	NOAA Northeast Fisheries Science Center
NJDEP	New Jersey Department of Environmental Protection
NYS-DEC/TT	New York State Department of Environmental Conservation and Tetra Tech, Inc.

Table 2: Institutions that contributed surveys used in this model. (*continued*)

Institution	Full Name
SEFSC	NOAA Southeast Fisheries Science Center
UNCW	University of North Carolina Wilmington
VAMSC	Virginia Aquarium & Marine Science Center

Table 3: Descriptions and references for survey programs used in this model.

Program	Description	References
AMAPPS	Atlantic Marine Assessment Program for Protected Species	Palka et al. (2017), Palka et al. (2021)
CNM	Northeast Canyons Marine National Monument Aerial Surveys	Redfern et al. (2021)
MATS	Mid-Atlantic Tursiops Surveys	
MD DNR WEA	Aerial Surveys of the Maryland Wind Energy Area	Barco et al. (2015)
MMS-WEA	Marine Mammal Surveys of the MA and RI Wind Energy Areas	Quintana-Rizzo et al. (2021), O’Brien et al. (2022)
NARWSS	North Atlantic Right Whale Sighting Surveys	Cole et al. (2007)
Navy Cape Hatteras	Aerial Surveys of the Navy’s Cape Hatteras Study Area	McLellan et al. (2018)
Navy Jacksonville	Aerial Surveys of the Navy’s Jacksonville Study Area	Foley et al. (2019)
Navy Norfolk Canyon	Aerial Surveys of the Navy’s Norfolk Canyon Study Area	Cotter (2019), McAlarney et al. (2018)
Navy Onslow Bay	Aerial Surveys of the Navy’s Onslow Bay Study Area	Read et al. (2014)
Navy VACAPES	Aerial Survey Baseline Monitoring in the Continental Shelf Region of the VACAPES OPAREA	Mallette et al. (2017)
NJEBS	New Jersey Ecological Baseline Study	Geo-Marine, Inc. (2010), Whitt et al. (2015)
NLPSC	Northeast Large Pelagic Survey Collaborative Aerial Surveys	Leiter et al. (2017), Stone et al. (2017)
NYBWM	New York Bight Whale Monitoring Surveys	Zoidis et al. (2021)
Pre-AMAPPS	Pre-AMAPPS Marine Mammal Abundance Surveys	Mullin and Fulling (2003), Garrison et al. (2010), Palka (2006)
SOTW Visual	R/V Song of the Whale Visual Surveys	Ryan et al. (2013)
VA CZM WEA	Virginia CZM Wind Energy Area Surveys	Mallette et al. (2014), Mallette et al. (2015)

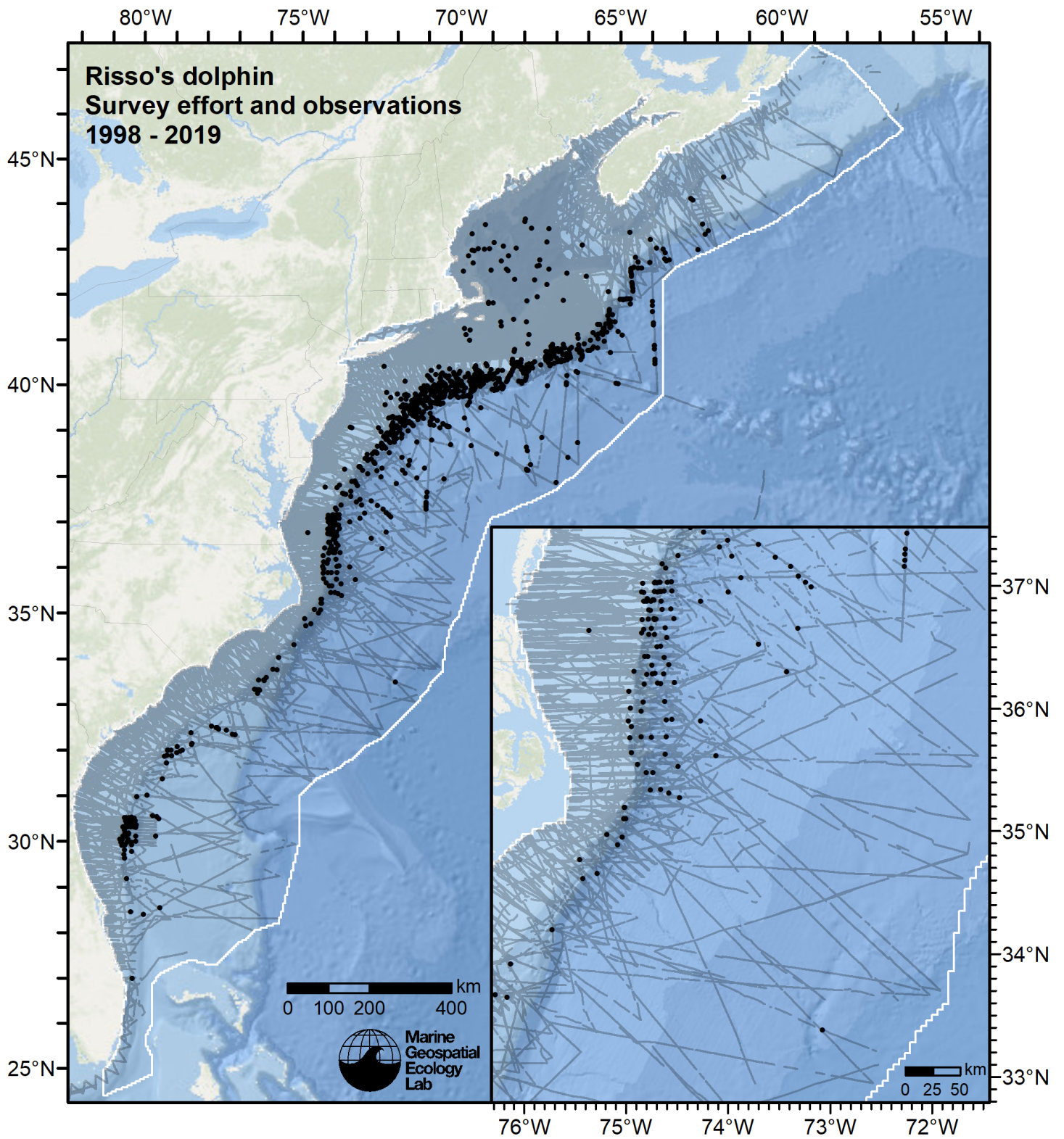


Figure 1: Survey effort and Risso's dolphin observations available for density modeling, after detection functions were applied, and excluded segments and truncated observations were removed.

2 Detection Functions

2.1 Taxon Specific

We fitted the detection functions in this section to Risso's dolphin observations exclusively, without pooling in other species. We usually adopted this approach when we had enough sightings of this taxon to fit a detection function without pooling and we judged that this taxon's detectability differed in important respects from others that pooling should be avoided if possible. We also occasionally used this approach for certain taxa that had similar detectability to others but for which we had so many sightings that pooling in other species provided little benefit.

2.1.1 Aerial Surveys

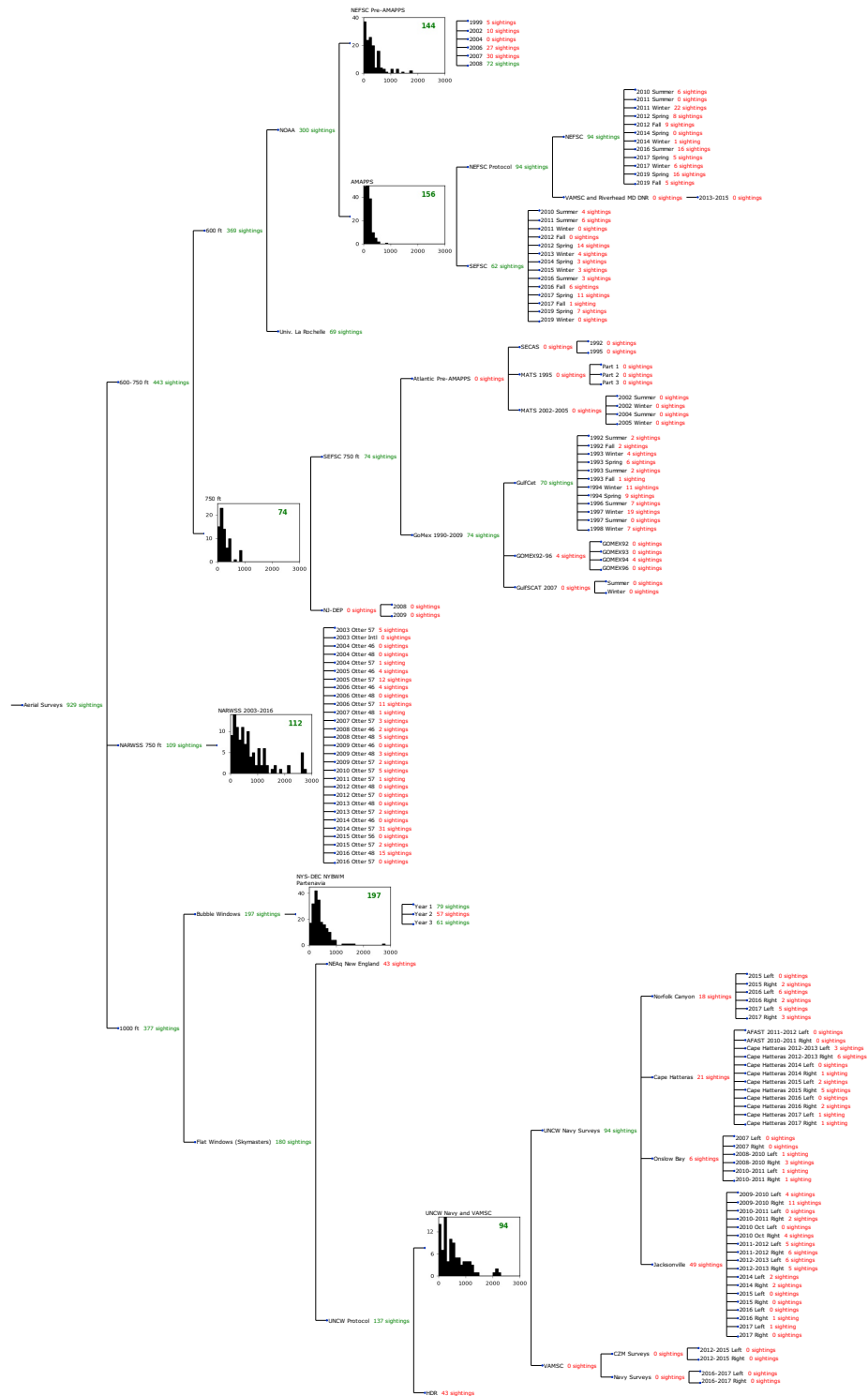


Figure 2: Detection hierarchy for aerial surveys, showing how they were pooled during detectability modeling, for taxon-specific detection functions. Each histogram represents a detection function and summarizes the perpendicular distances of observations that were pooled to fit it, prior to truncation. Observation counts, also prior to truncation, are shown in green when they met the recommendation of Buckland et al. (2001) that detection functions utilize at least 60 sightings, and red otherwise. For rare taxa, it was not always possible to meet this recommendation, yielding higher statistical uncertainty. During the spatial modeling stage of the analysis, effective strip widths were computed for each survey using the closest detection function above it in the hierarchy (i.e. moving from right to left in the figure). Surveys that do not have a detection function above them in this figure were either addressed by a detection function presented in a different section of this report, or were omitted from the analysis.

2.1.1.1 NEFSC Pre-AMAPPS

After right-truncating observations greater than 1300 m, we fitted the detection function to the 141 observations that remained. The selected detection function (Figure 3) used a hazard rate key function with no covariates.

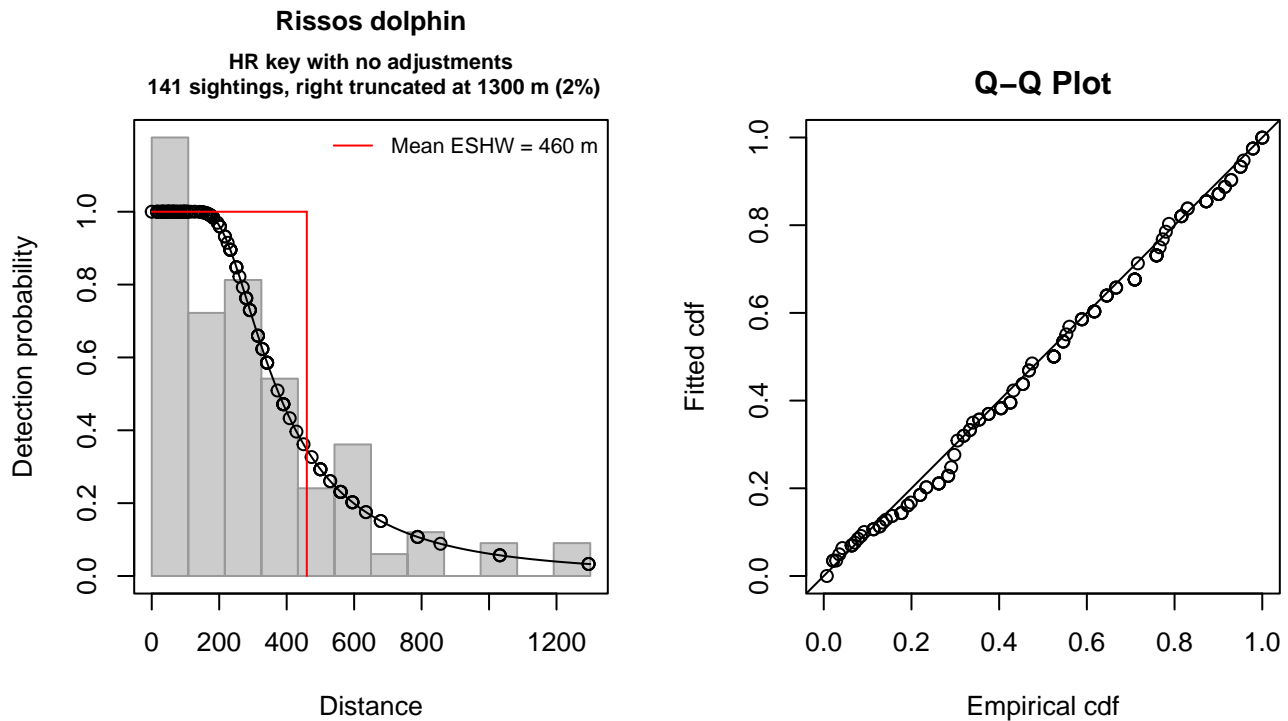


Figure 3: NEFSC Pre-AMAPPS detection function and Q-Q plot showing its goodness of fit.

Statistical output for this detection function:

```
Summary for ds object
Number of observations : 141
Distance range       : 0 - 1300
AIC                  : 1888.705

Detection function:
Hazard-rate key function

Detection function parameters
Scale coefficient(s):
      estimate      se
(Intercept) 5.783018 0.1393253

Shape coefficient(s):
      estimate      se
(Intercept) 0.8979121 0.1575566

      Estimate      SE      CV
Average p      0.3536124 0.03282537 0.09282867
N in covered region 398.7416729 45.81448388 0.11489766

Distance sampling Cramer-von Mises test (unweighted)
Test statistic = 0.041768 p = 0.923827
```

2.1.1.2 AMAPPS

After right-truncating observations greater than 600 m, we fitted the detection function to the 155 observations that remained. The selected detection function (Figure 4) used a hazard rate key function with Beaufort (Figure 5), Provider (Figure 6) and Season (Figure 7) as covariates.

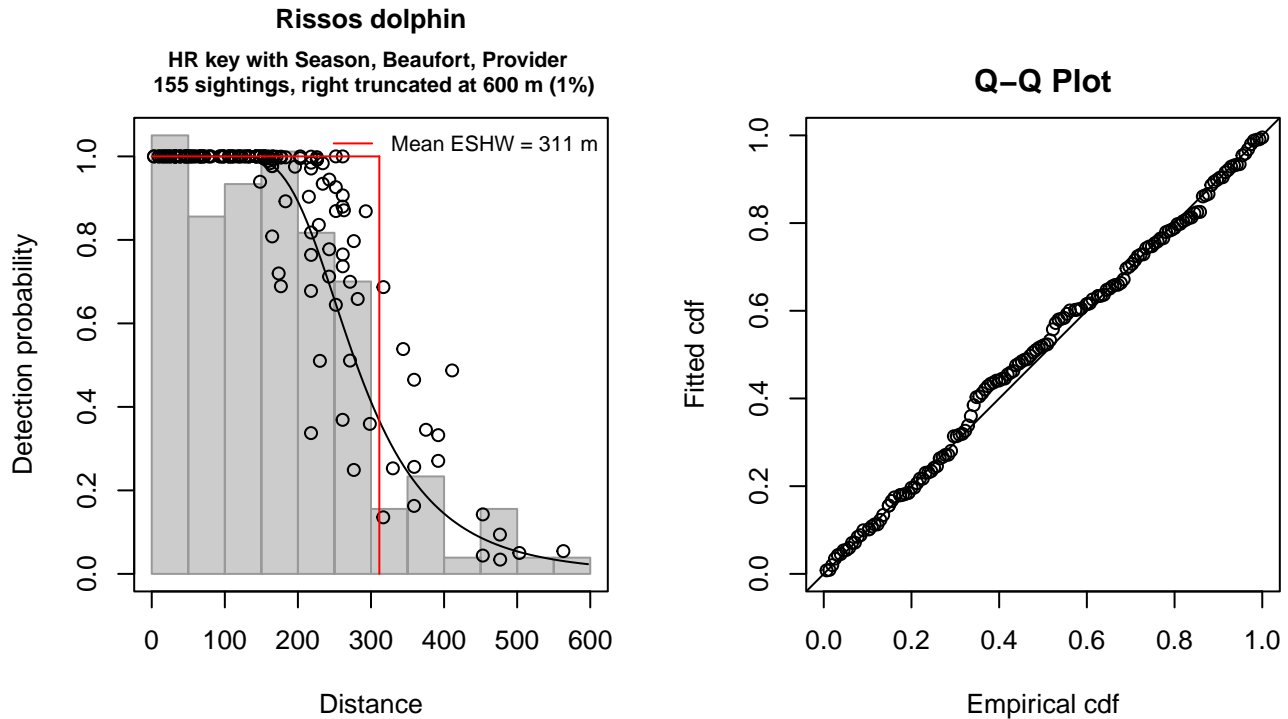


Figure 4: AMAPPS detection function and Q-Q plot showing its goodness of fit.

Statistical output for this detection function:

```
Summary for ds object
Number of observations : 155
Distance range       : 0 - 600
AIC                  : 1866.649

Detection function:
Hazard-rate key function

Detection function parameters
Scale coefficient(s):
      estimate      se
(Intercept)  6.0366032 0.17762330
SeasonSummer  0.1802786 0.13721927
Beaufort     -0.1650827 0.06395012
ProviderSEFSC -0.1706089 0.11019046

Shape coefficient(s):
      estimate      se
(Intercept) 1.604171 0.1939995

      Estimate      SE      CV
Average p      0.5025078 0.0288734 0.05745860
N in covered region 308.4529003 25.0928195 0.08135057
```

Distance sampling Cramer-von Mises test (unweighted)
 Test statistic = 0.074634 p = 0.723455

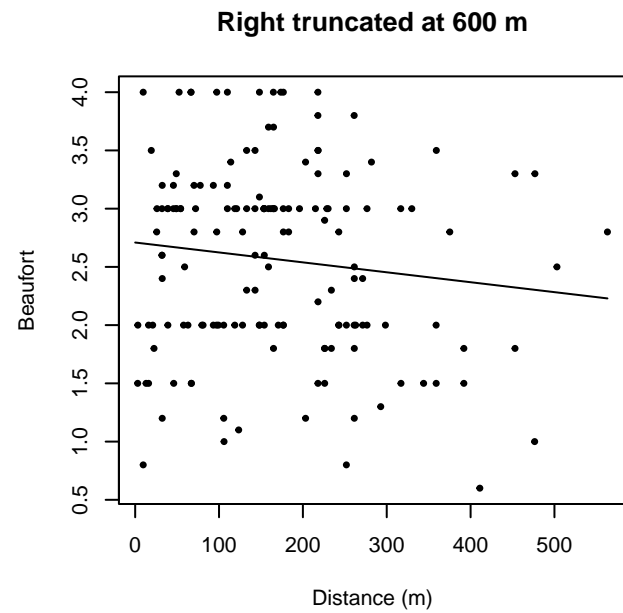
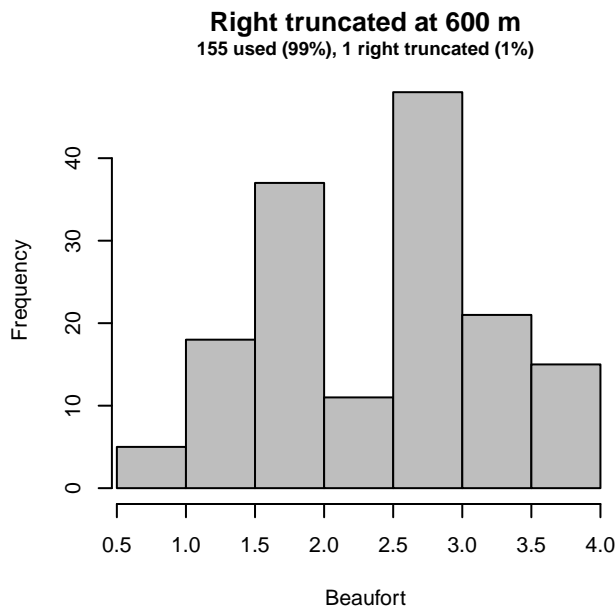
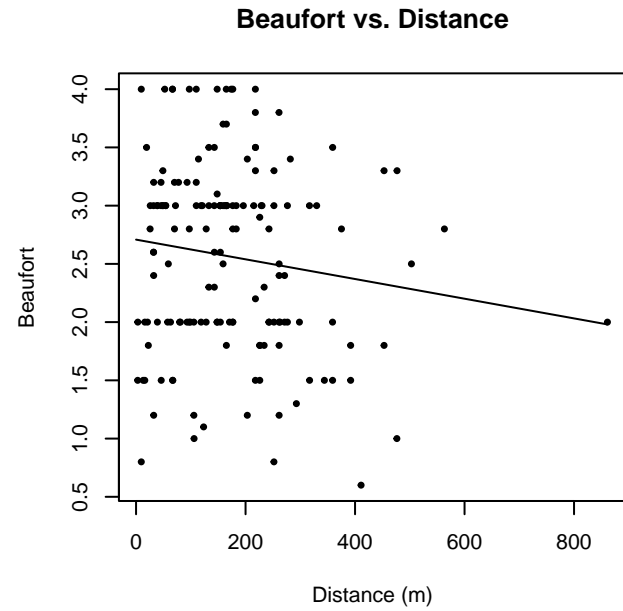
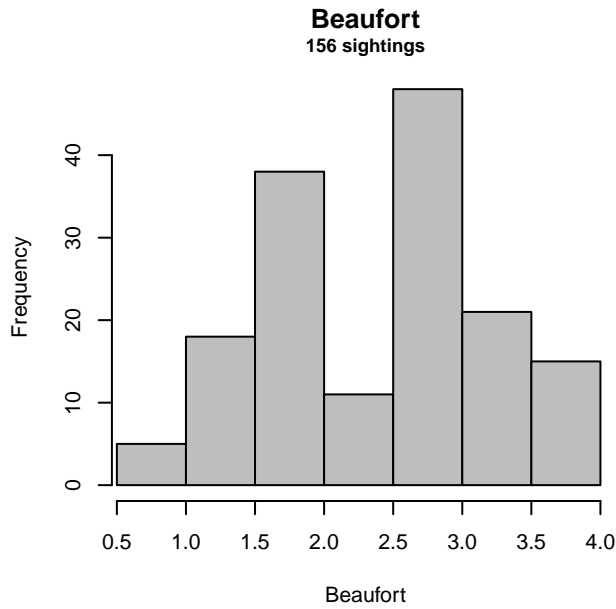


Figure 5: Distribution of the Beaufort covariate before (top row) and after (bottom row) observations were truncated to fit the AMAPPS detection function.

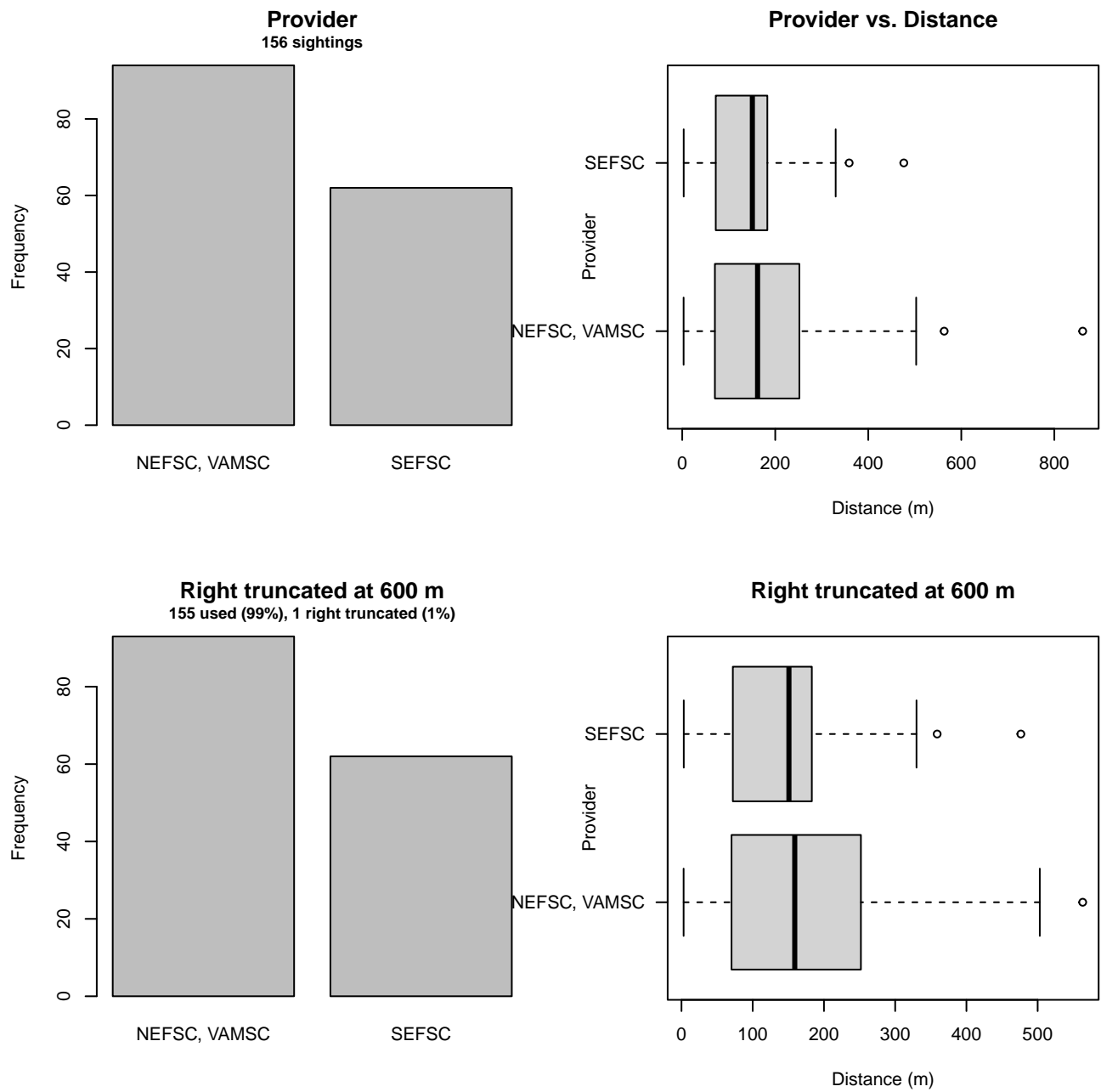


Figure 6: Distribution of the Provider covariate before (top row) and after (bottom row) observations were truncated to fit the AMAPPS detection function.

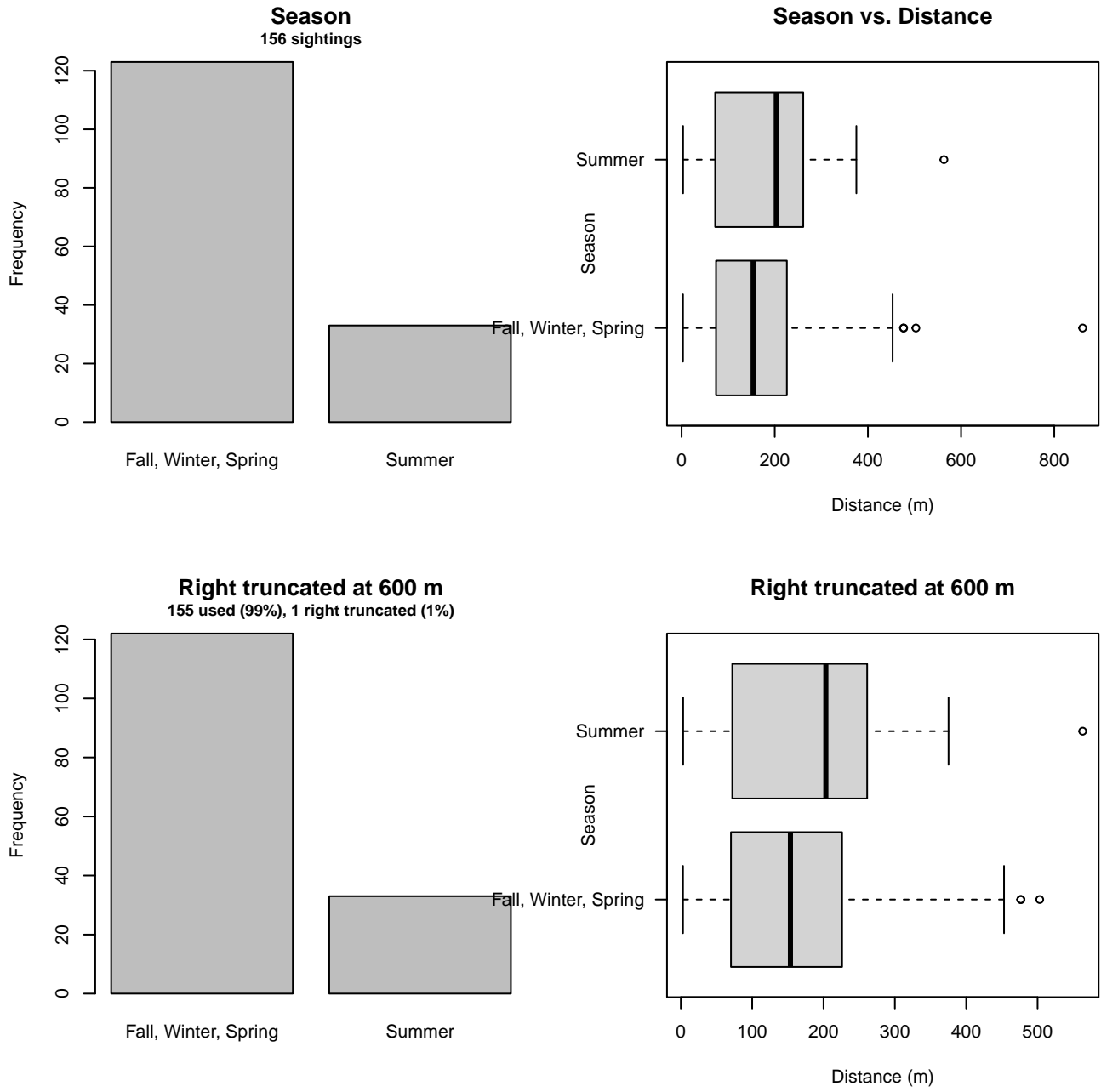


Figure 7: Distribution of the Season covariate before (top row) and after (bottom row) observations were truncated to fit the AMAPPS detection function.

2.1.1.3 750 ft

After right-truncating observations greater than 629 m, we fitted the detection function to the 69 observations that remained. The selected detection function (Figure 8) used a half normal key function with no covariates.

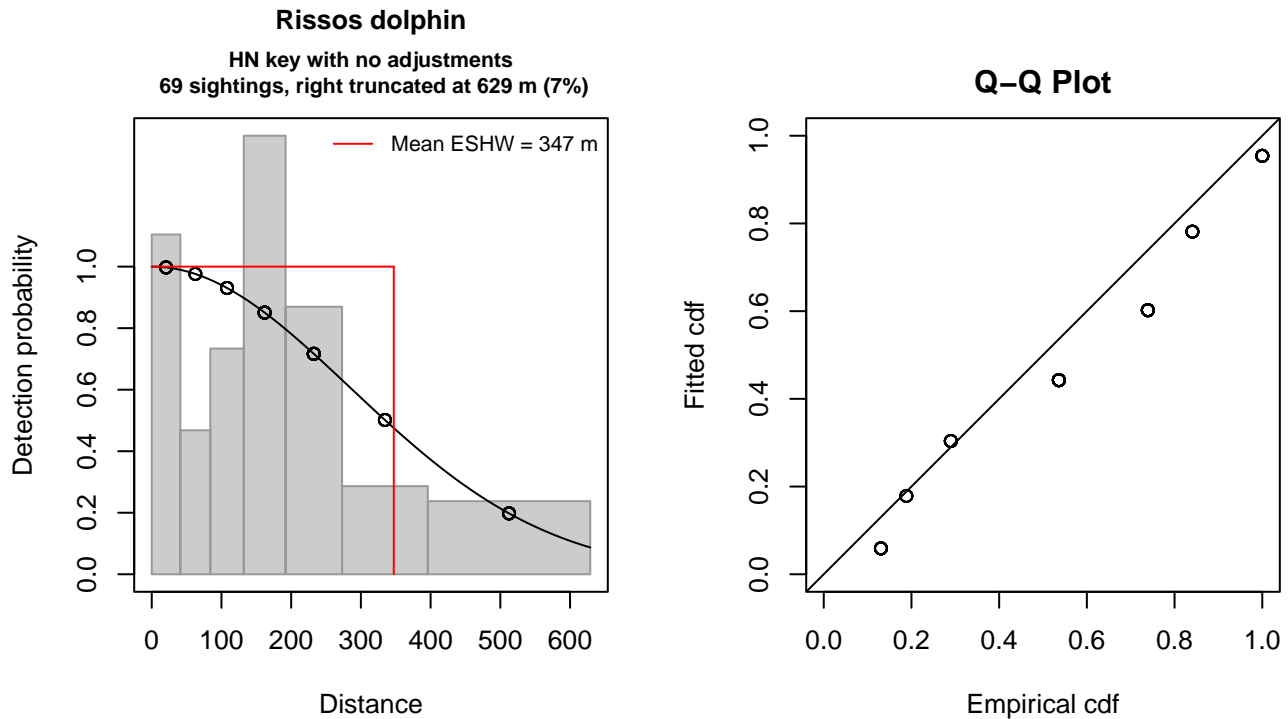


Figure 8: 750 ft detection function and Q-Q plot showing its goodness of fit.

Statistical output for this detection function:

Summary for ds object

Number of observations : 69
Distance range : 0 - 629
AIC : 268.7436

Detection function:

Half-normal key function

Detection function parameters

Scale coefficient(s):

	estimate	se
(Intercept)	5.651496	0.1211091

	Estimate	SE	CV
Average p	0.5519047	0.05628833	0.1019892
N in covered region	125.0215774	16.25085030	0.1299844

Distance sampling Cramer-von Mises test (unweighted)

Test statistic = 0.259911 p = 0.176148

2.1.1.4 NARWSS 2003-2016

After right-truncating observations greater than 2905 m, we fitted the detection function to the 109 observations that remained. The selected detection function (Figure 9) used a hazard rate key function with QualityCode (Figure 10) and Season (Figure 11) as covariates.

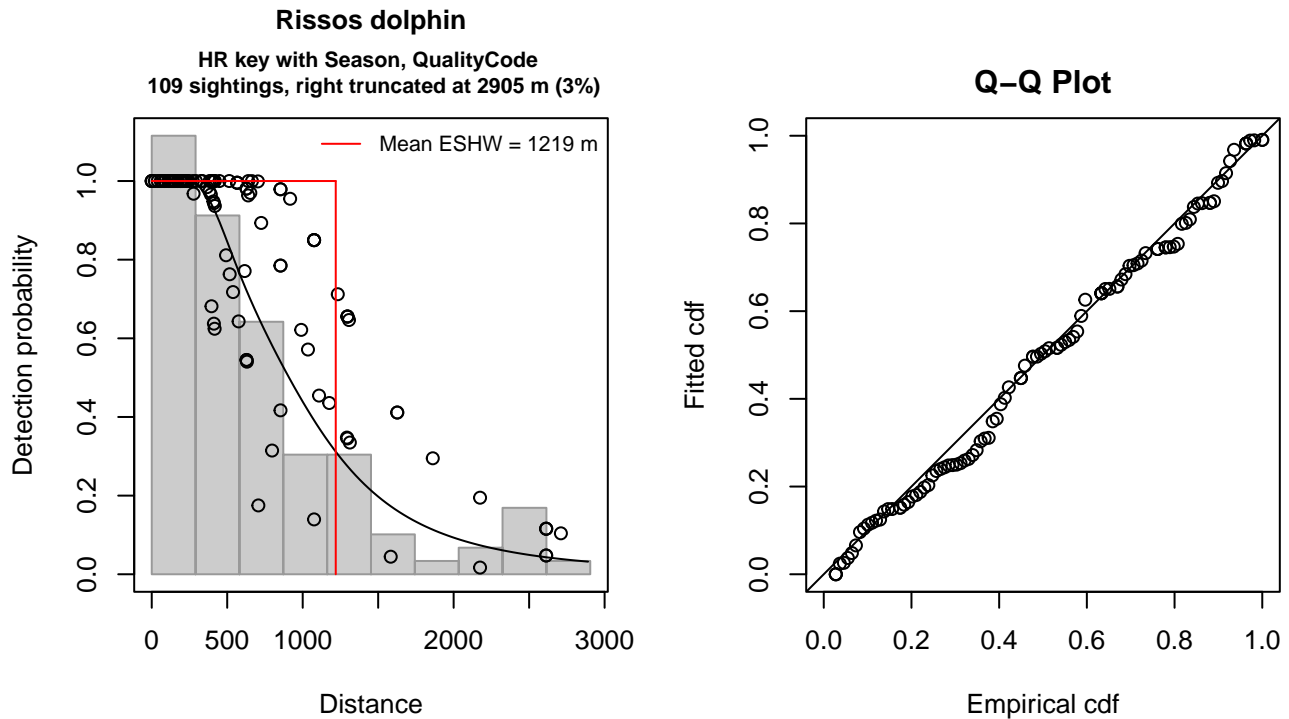


Figure 9: NARWSS 2003-2016 detection function and Q-Q plot showing its goodness of fit.

Statistical output for this detection function:

Summary for ds object

Number of observations : 109
 Distance range : 0 - 2905
 AIC : 1639.18

Detection function:

Hazard-rate key function

Detection function parameters

Scale coefficient(s):

	estimate	se
(Intercept)	6.3650810	0.2068446
SeasonSpring	0.5234198	0.2376887
SeasonSummer	0.8229384	0.2196057
QualityCodeModerate, Good	-0.3400065	0.2869091

Shape coefficient(s):

	estimate	se
(Intercept)	1.124971	0.1769014

	Estimate	SE	CV
Average p	0.3683485	0.0382738	0.1039065
N in covered region	295.9154459	38.6527824	0.1306210

Distance sampling Cramer-von Mises test (unweighted)

Test statistic = 0.071264 p = 0.743830

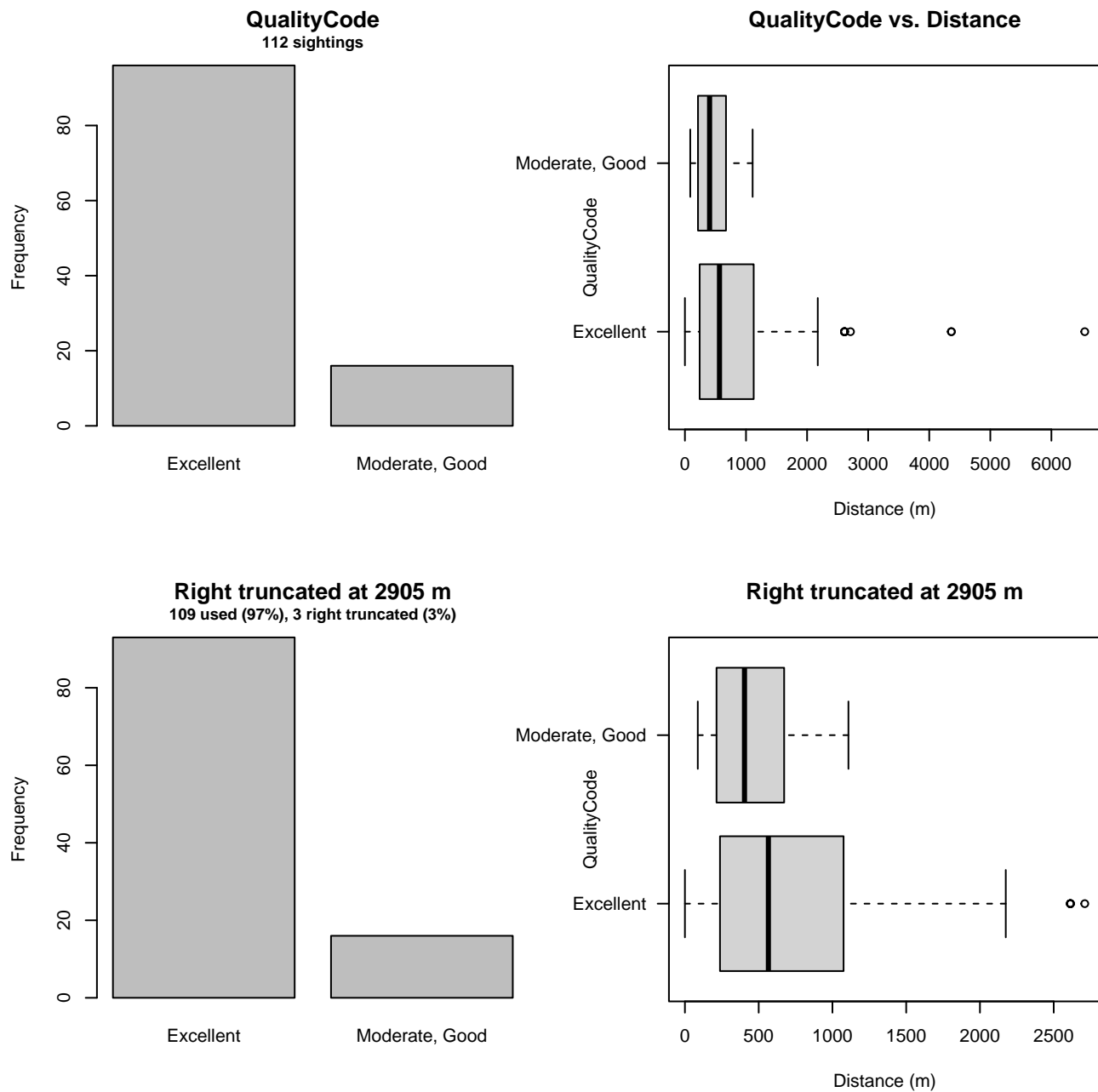


Figure 10: Distribution of the QualityCode covariate before (top row) and after (bottom row) observations were truncated to fit the NARWSS 2003-2016 detection function.

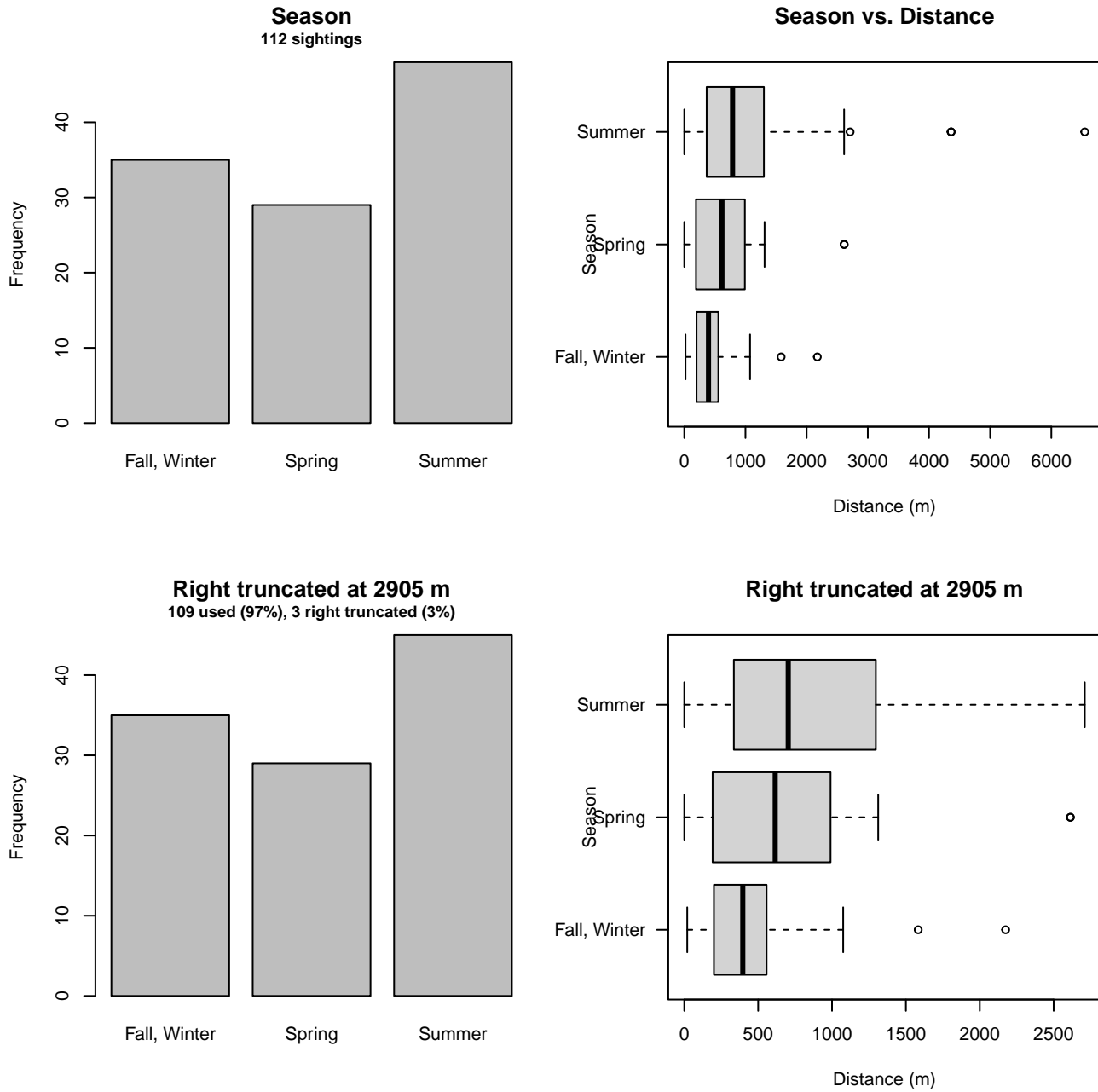


Figure 11: Distribution of the Season covariate before (top row) and after (bottom row) observations were truncated to fit the NARWSS 2003-2016 detection function.

2.1.1.5 NYS-DEC NYBWM Partenavia

After right-truncating observations greater than 1000 m and left-truncating observations less than 125 m (Figure 13), we fitted the detection function to the 169 observations that remained. The selected detection function (Figure 12) used a half normal key function with Beaufort (Figure 14) as a covariate.

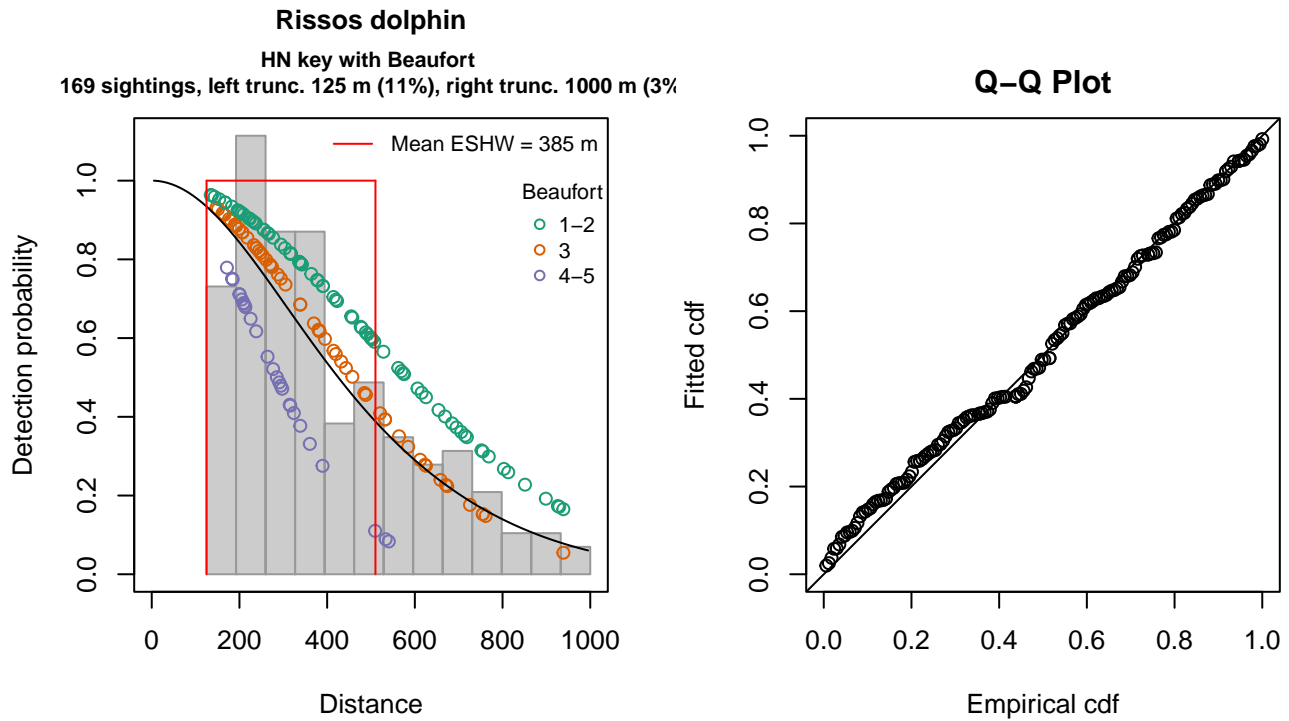


Figure 12: NYS-DEC NYBWM Partenavia detection function and Q-Q plot showing its goodness of fit.

Statistical output for this detection function:

Summary for ds object

Number of observations : 169
 Distance range : 125 - 1000
 AIC : 2200.122

Detection function:

Half-normal key function

Detection function parameters

Scale coefficient(s):

	estimate	se
(Intercept)	6.2039137	0.1207221
Beaufort3	-0.2389864	0.1614072
Beaufort4-5	-0.7126758	0.1974434

	Estimate	SE	CV
Average p	0.3960252	0.03972109	0.1002994
N in covered region	426.7405688	50.30313947	0.1178776

Distance sampling Cramer-von Mises test (unweighted)
 Test statistic = 0.106475 p = 0.554053

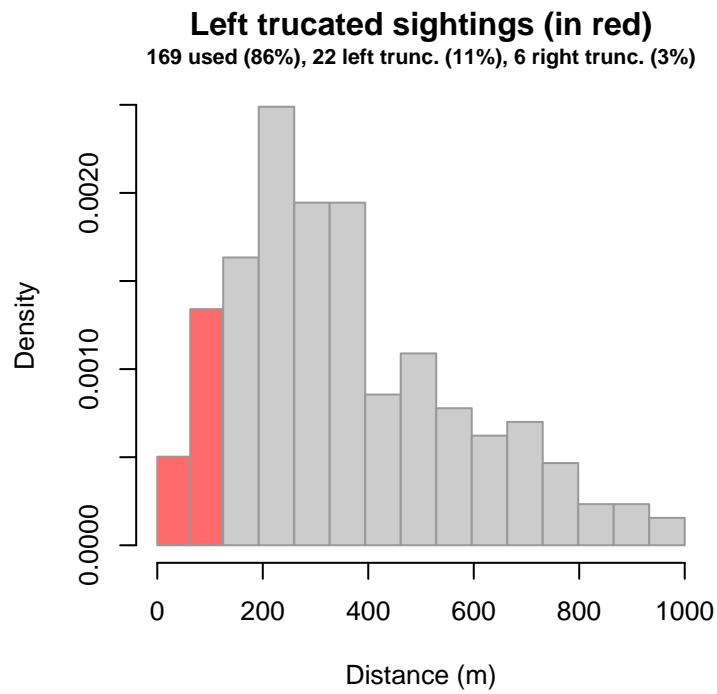


Figure 13: Density histogram of observations used to fit the NYS-DEC NYBWM Partenavia detection function, with the left-most bar showing observations at distances less than 125 m, which were left-truncated and excluded from the analysis [Buckland et al. (2001)]. (This bar may be very short if there were very few left-truncated sightings, or very narrow if the left truncation distance was very small; in either case it may not appear red.)

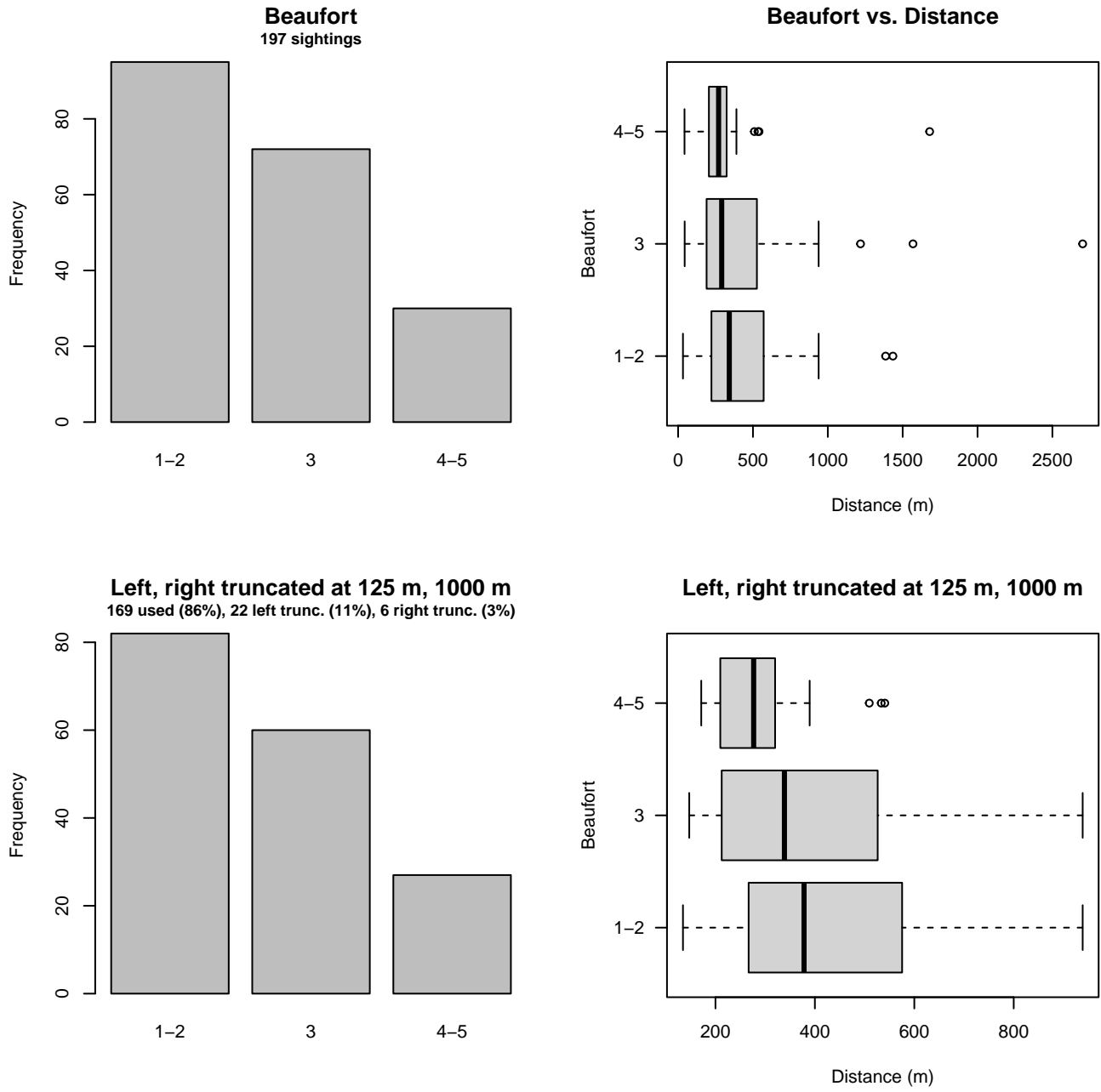


Figure 14: Distribution of the Beaufort covariate before (top row) and after (bottom row) observations were truncated to fit the NYS-DEC NYBWM Partenavia detection function.

2.1.1.6 UNCW Navy and VAMSC

After right-truncating observations greater than 1500 m, we fitted the detection function to the 90 observations that remained. The selected detection function (Figure 15) used a hazard rate key function with Clouds (Figure 16) and Season (Figure 17) as covariates.

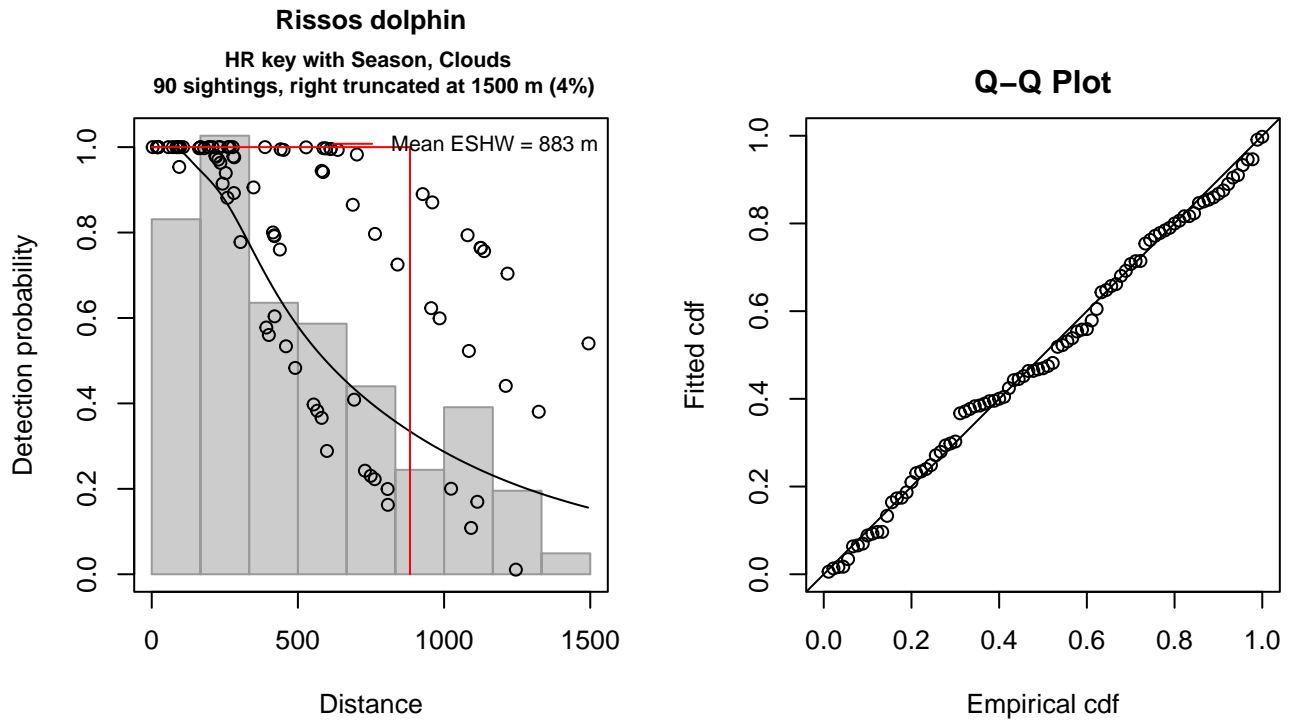


Figure 15: UNCW Navy and VAMSC detection function and Q-Q plot showing its goodness of fit.

Statistical output for this detection function:

Summary for ds object

Number of observations : 90
Distance range : 0 - 1500
AIC : 1284.779

Detection function:

Hazard-rate key function

Detection function parameters

Scale coefficient(s):

	estimate	se
(Intercept)	6.0056311	0.3035881
SeasonSpring	0.8456171	0.4102252
SeasonSummer	1.1884279	0.4533264
CloudsHaze	-0.9484006	0.4044859

Shape coefficient(s):

	estimate	se
(Intercept)	0.7816279	0.2776556

	Estimate	SE	CV
Average p	0.4888842	0.07459626	0.1525847
N in covered region	184.0926770	31.92421540	0.1734138

Distance sampling Cramer-von Mises test (unweighted)

Test statistic = 0.037830 p = 0.944001

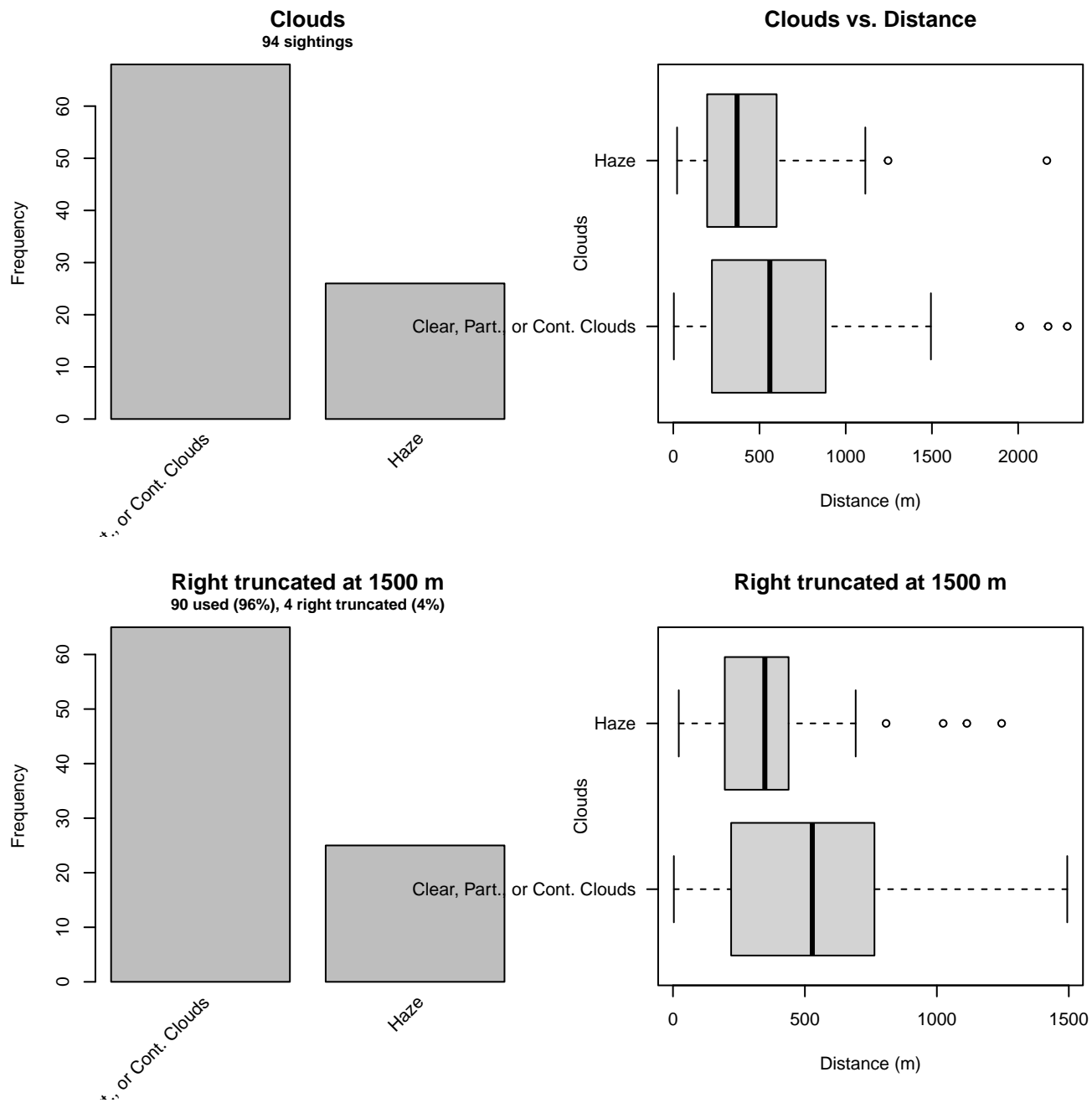


Figure 16: Distribution of the Clouds covariate before (top row) and after (bottom row) observations were truncated to fit the UNCW Navy and VAMSC detection function.

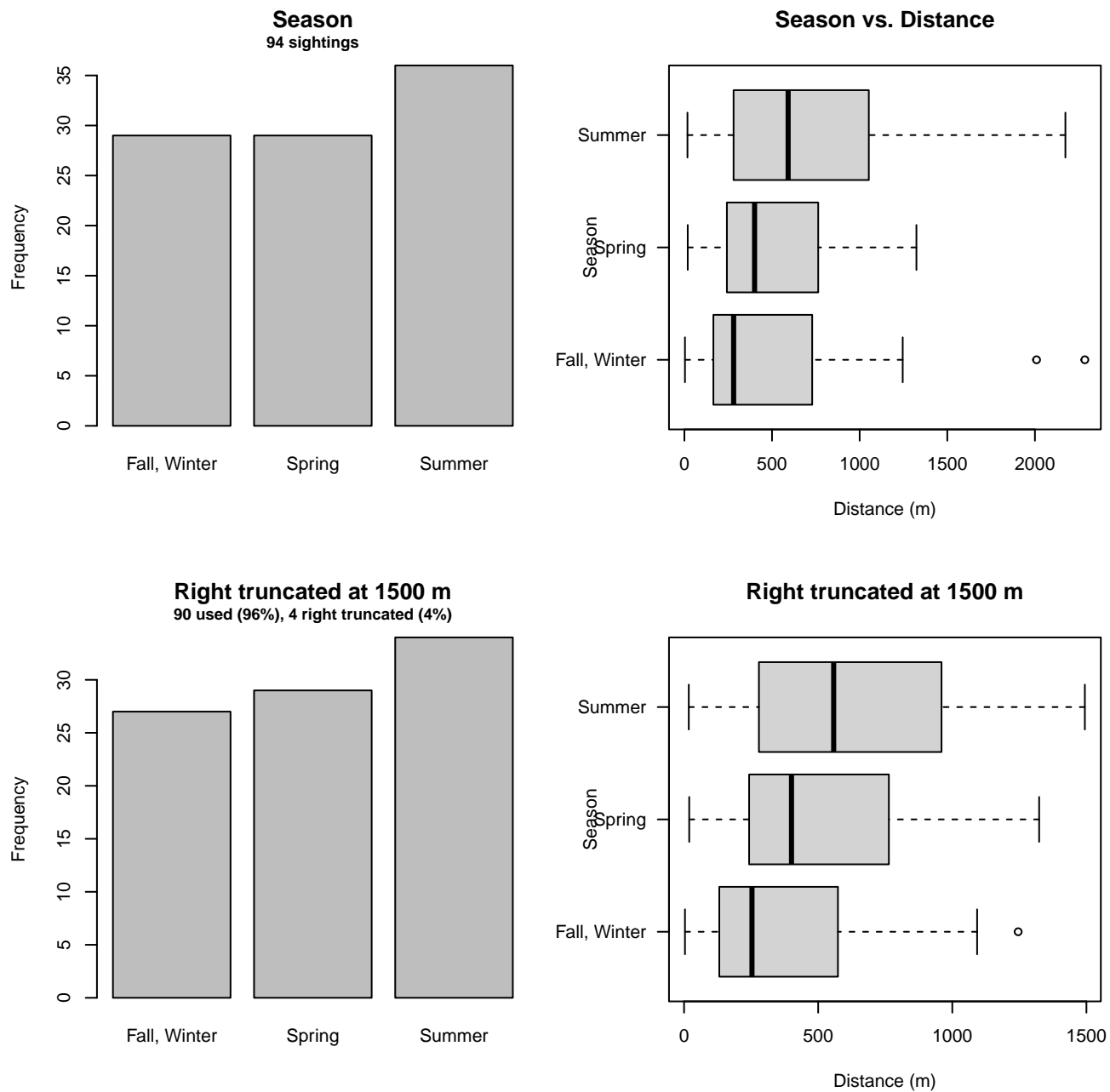


Figure 17: Distribution of the Season covariate before (top row) and after (bottom row) observations were truncated to fit the UNCW Navy and VAMSC detection function.

2.1.2 Shipboard Surveys

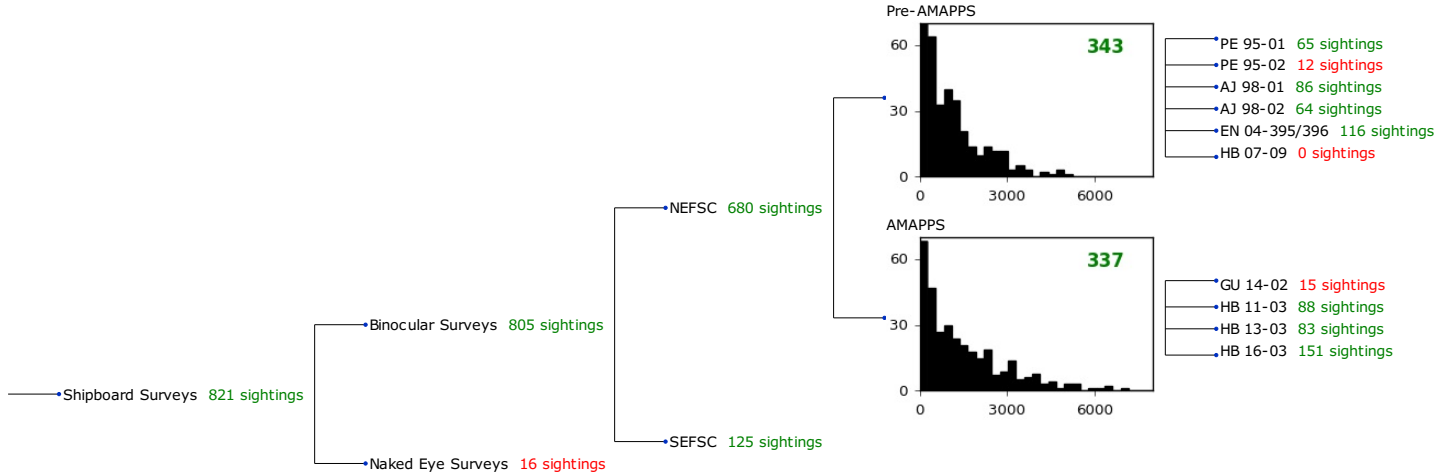


Figure 18: Detection hierarchy for shipboard surveys, showing how they were pooled during detectability modeling, for taxon-specific detection functions. Each histogram represents a detection function and summarizes the perpendicular distances of observations that were pooled to fit it, prior to truncation. Observation counts, also prior to truncation, are shown in green when they met the recommendation of Buckland et al. (2001) that detection functions utilize at least 60 sightings, and red otherwise. For rare taxa, it was not always possible to meet this recommendation, yielding higher statistical uncertainty. During the spatial modeling stage of the analysis, effective strip widths were computed for each survey using the closest detection function above it in the hierarchy (i.e. moving from right to left in the figure). Surveys that do not have a detection function above them in this figure were either addressed by a detection function presented in a different section of this report, or were omitted from the analysis.

2.1.2.1 NEFSC Pre-AMAPPS

After right-truncating observations greater than 3200 m, we fitted the detection function to the 328 observations that remained. The selected detection function (Figure 19) used a hazard rate key function with Beaufort (Figure 20) and VesselName (Figure 21) as covariates.

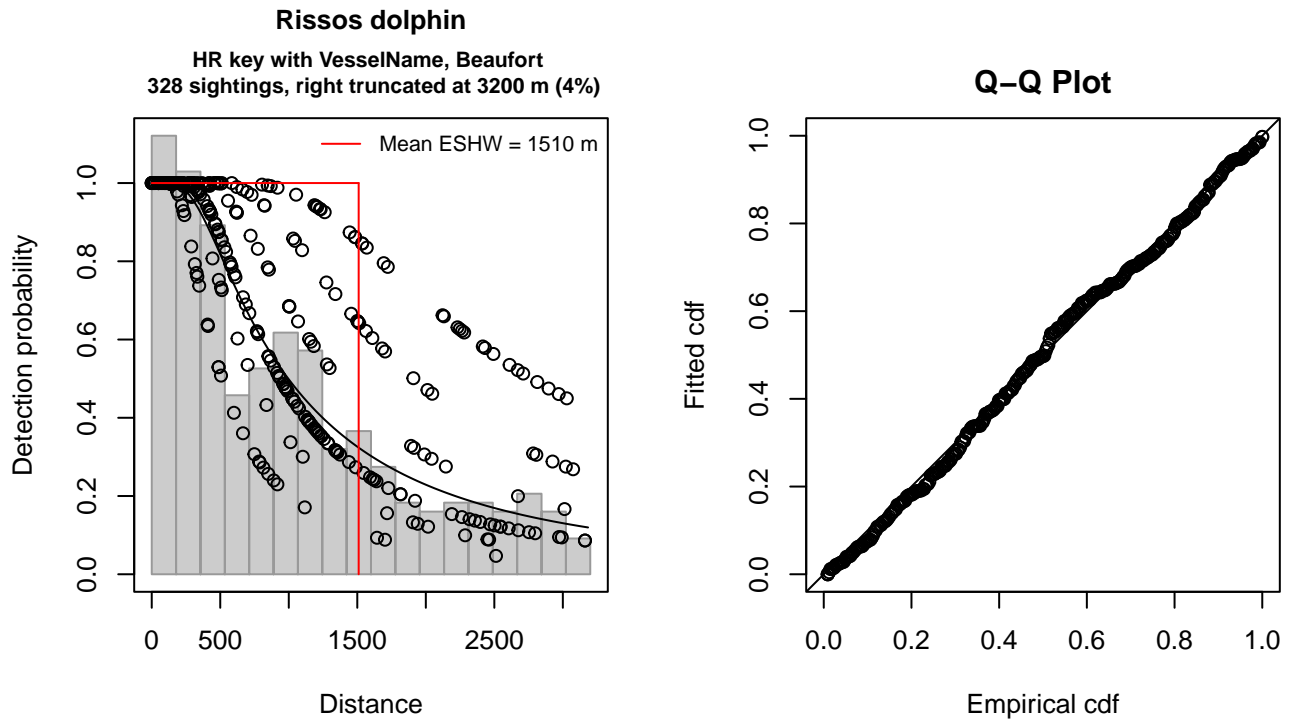


Figure 19: NEFSC Pre-AMAPPS detection function and Q-Q plot showing its goodness of fit.

Statistical output for this detection function:

Summary for ds object

Number of observations : 328
Distance range : 0 - 3200
AIC : 5133.385

Detection function:

Hazard-rate key function

Detection function parameters

Scale coefficient(s):

	estimate	se
(Intercept)	7.3380833	0.2397354
VesselNameEndeavor, Bigelow	0.3708193	0.2236364
Beaufort2-3	-0.7126647	0.2624438
Beaufort3-4	-1.3169939	0.3221948

Shape coefficient(s):

	estimate	se
(Intercept)	0.5179626	0.1388253

	Estimate	SE	CV
Average p	0.4168668	0.03634946	0.08719682
N in covered region	786.8220667	76.88728921	0.09771878

Distance sampling Cramer-von Mises test (unweighted)

Test statistic = 0.080373 p = 0.689698

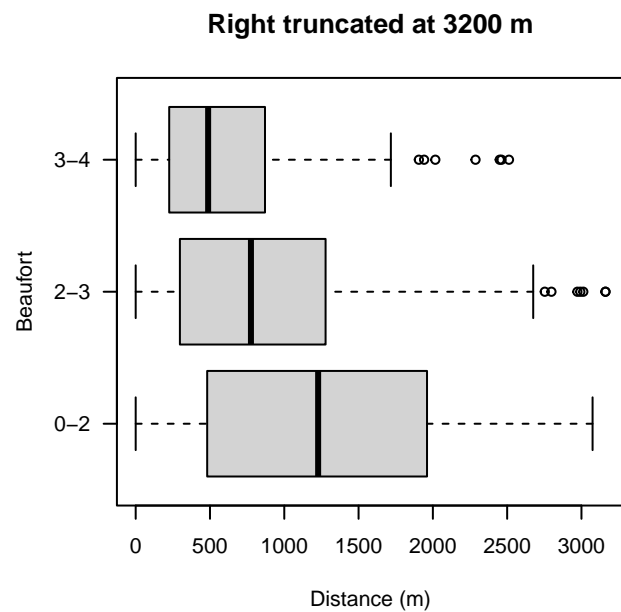
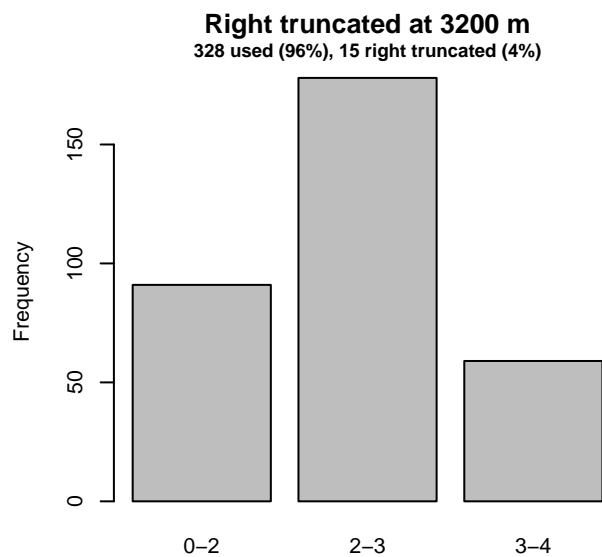
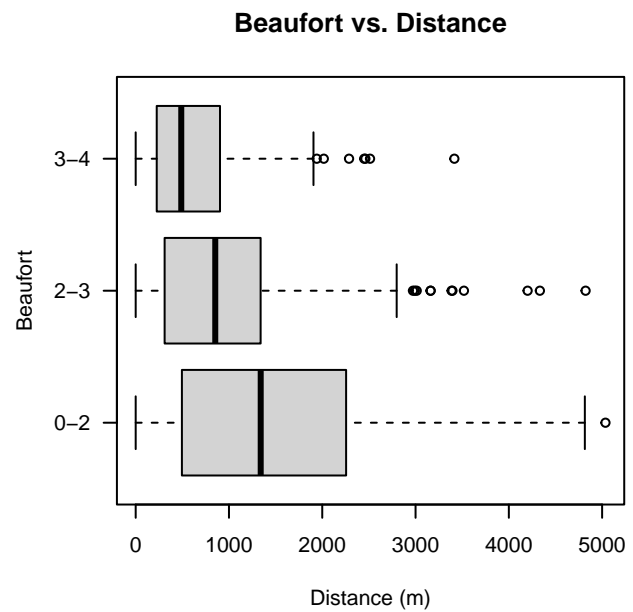
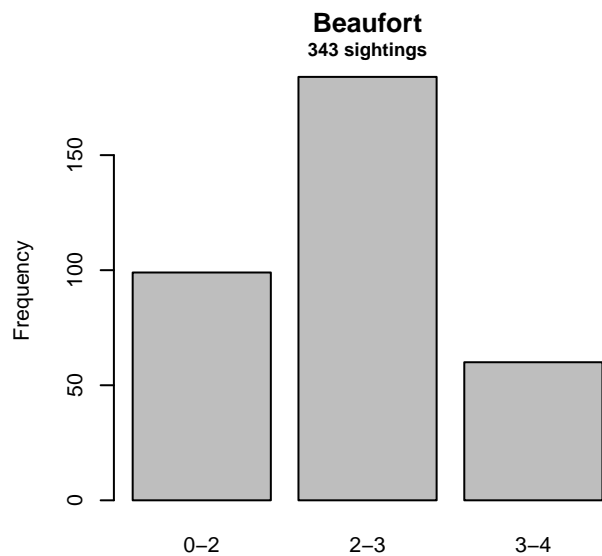


Figure 20: Distribution of the Beaufort covariate before (top row) and after (bottom row) observations were truncated to fit the NEFSC Pre-AMAPPS detection function.

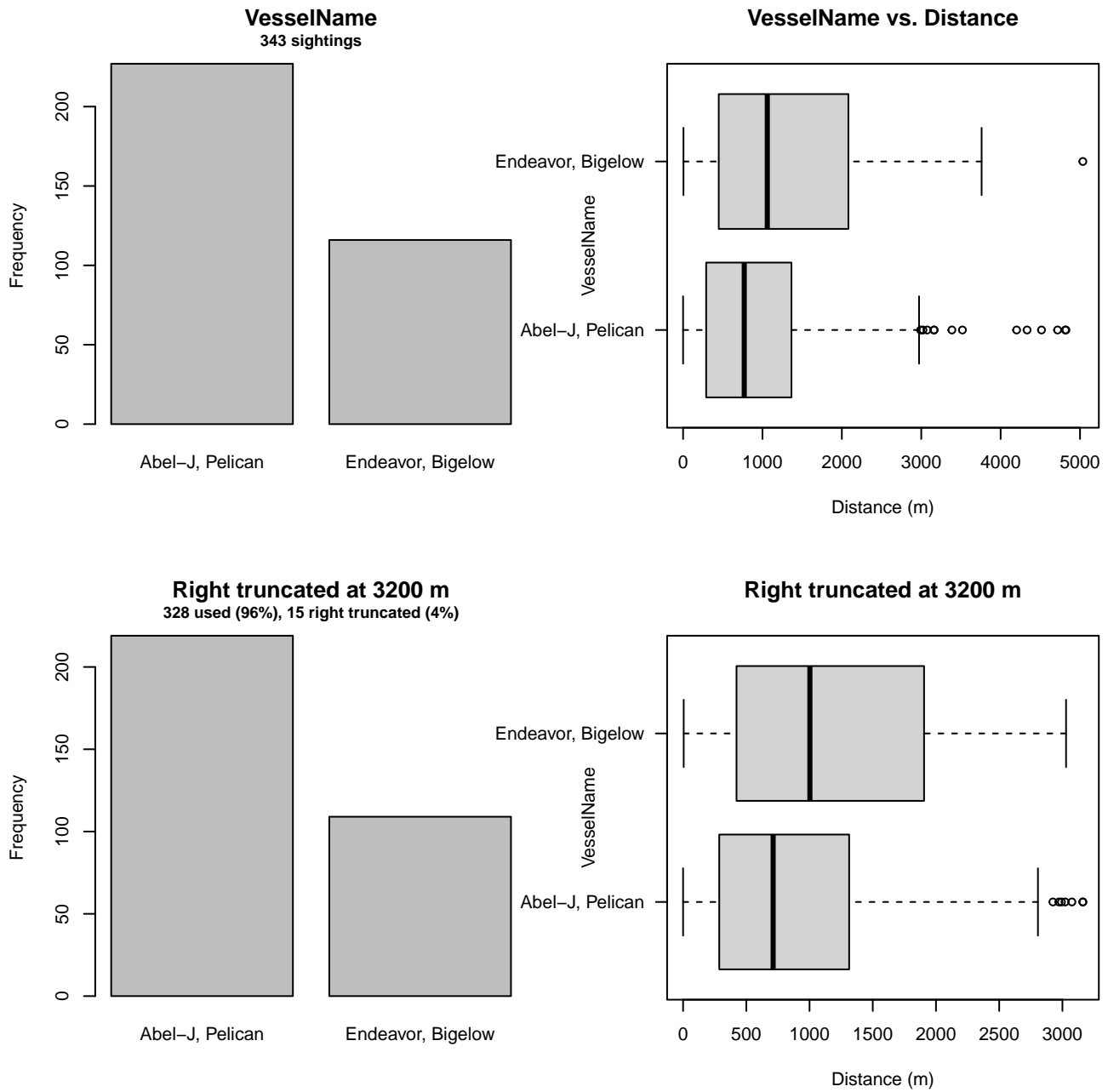


Figure 21: Distribution of the VesselName covariate before (top row) and after (bottom row) observations were truncated to fit the NEFSC Pre-AMAPPS detection function.

2.1.2.2 NEFSC AMAPPS

After right-truncating observations greater than 4600 m, we fitted the detection function to the 325 observations that remained. The selected detection function (Figure 22) used a hazard rate key function with Beaufort (Figure 23) as a covariate.

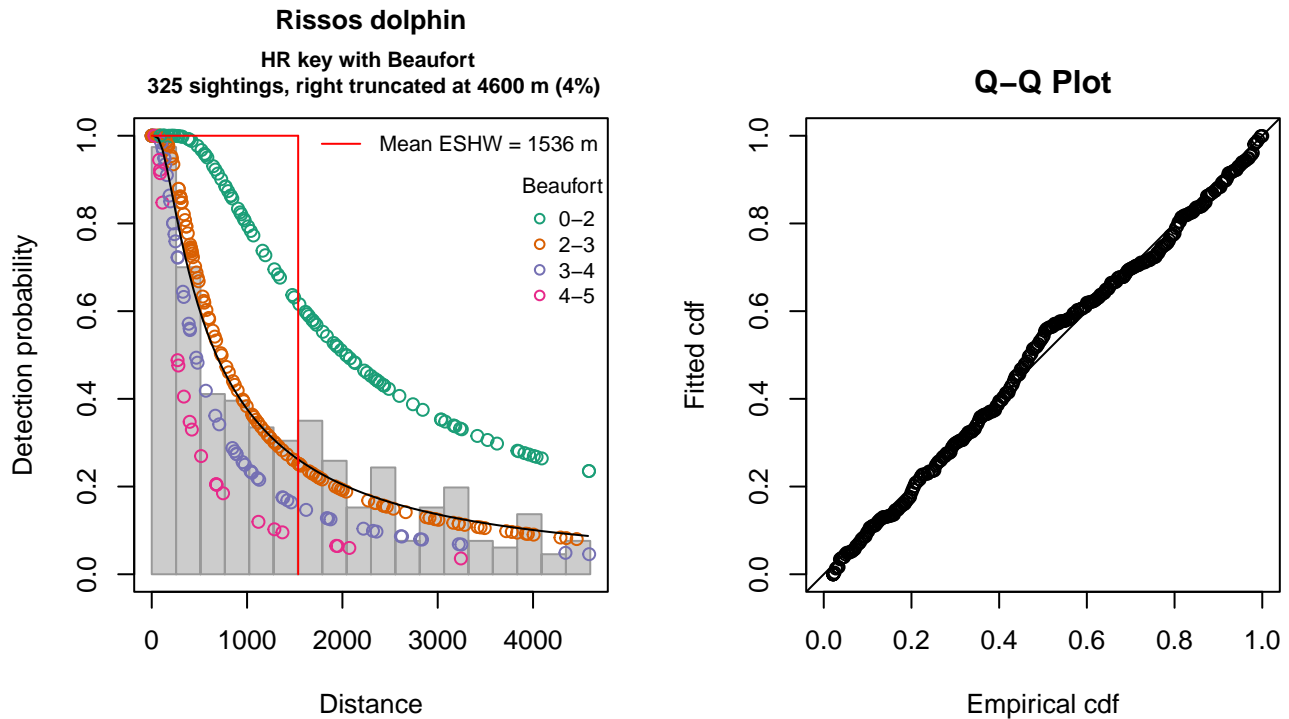


Figure 22: NEFSC AMAPPS detection function and Q-Q plot showing its goodness of fit.

Statistical output for this detection function:

Summary for ds object

Number of observations : 325
 Distance range : 0 - 4600
 AIC : 5290.397

Detection function:

Hazard-rate key function

Detection function parameters

Scale coefficient(s):

	estimate	se
(Intercept)	7.307447	0.2885097
Beaufort2-3	-1.024384	0.3650648
Beaufort3-4	-1.488882	0.4685369
Beaufort4-5	-2.046895	0.6275945

Shape coefficient(s):

	estimate	se
(Intercept)	0.1578318	0.1235713

	Estimate	SE	CV
Average p	0.2748169	0.03819416	0.1389804
N in covered region	1182.6057416	174.32412247	0.1474068

Distance sampling Cramer-von Mises test (unweighted)

Test statistic = 0.099287 p = 0.588382

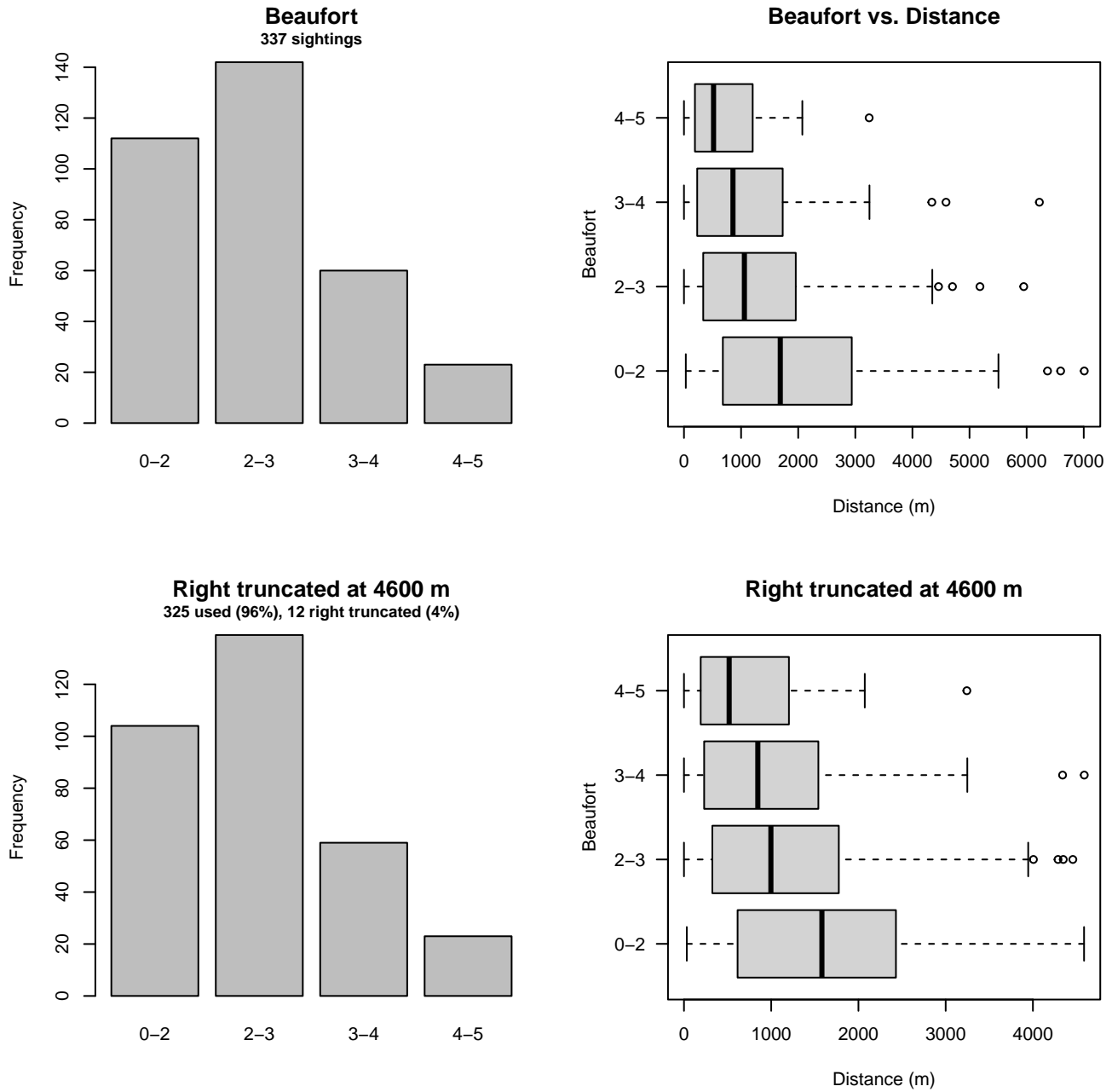


Figure 23: Distribution of the Beaufort covariate before (top row) and after (bottom row) observations were truncated to fit the NEFSC AMAPPS detection function.

2.2 Without a Taxonomic Covariate

We fitted the detection functions in this section to pools of species with similar detectability characteristics but could not use a taxonomic identification as a covariate to account for differences between them. We usually took this approach after trying the taxonomic covariate and finding it had insufficient statistical power to be retained. We also resorted to it when the focal taxon being modeled had too few observations to be allocated its own taxonomic covariate level and was too poorly known for us to confidently determine which other taxa we could group it with.

2.2.1 Blackfish

2.2.1.1 Shipboard Surveys

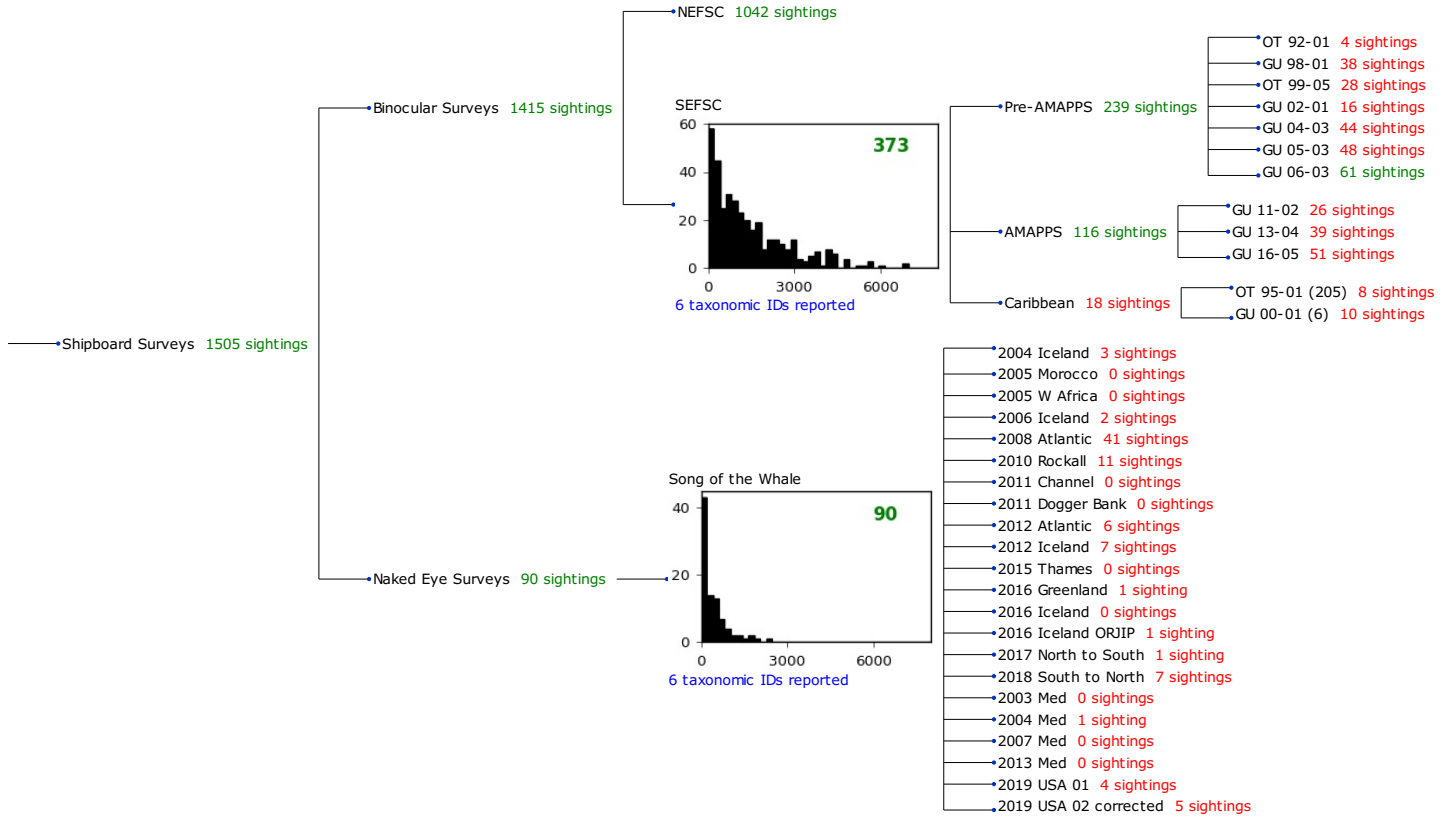


Figure 24: Detection hierarchy for shipboard surveys, showing how they were pooled during detectability modeling, for detection functions that pooled multiple taxa but could not use a taxonomic covariate to account for differences between them. Each histogram represents a detection function and summarizes the perpendicular distances of observations that were pooled to fit it, prior to truncation. Observation counts, also prior to truncation, are shown in green when they met the recommendation of Buckland et al. (2001) that detection functions utilize at least 60 sightings, and red otherwise. For rare taxa, it was not always possible to meet this recommendation, yielding higher statistical uncertainty. During the spatial modeling stage of the analysis, effective strip widths were computed for each survey using the closest detection function above it in the hierarchy (i.e. moving from right to left in the figure). Surveys that do not have a detection function above them in this figure were either addressed by a detection function presented in a different section of this report, or were omitted from the analysis.

2.2.1.1.1 SEFSC

After right-truncating observations greater than 4500 m, we fitted the detection function to the 361 observations that remained (Table 4). The selected detection function (Figure 25) used a hazard rate key function with Beaufort (Figure 26) and VesselName (Figure 27) as covariates.

Table 4: Observations used to fit the SEFSC detection function.

ScientificName	n
Feresa attenuata/Peponocephala electra	7
Globicephala	227
Grampus griseus	121
Orcinus orca	1
Peponocephala electra	3
Pseudorca crassidens	2
Total	361

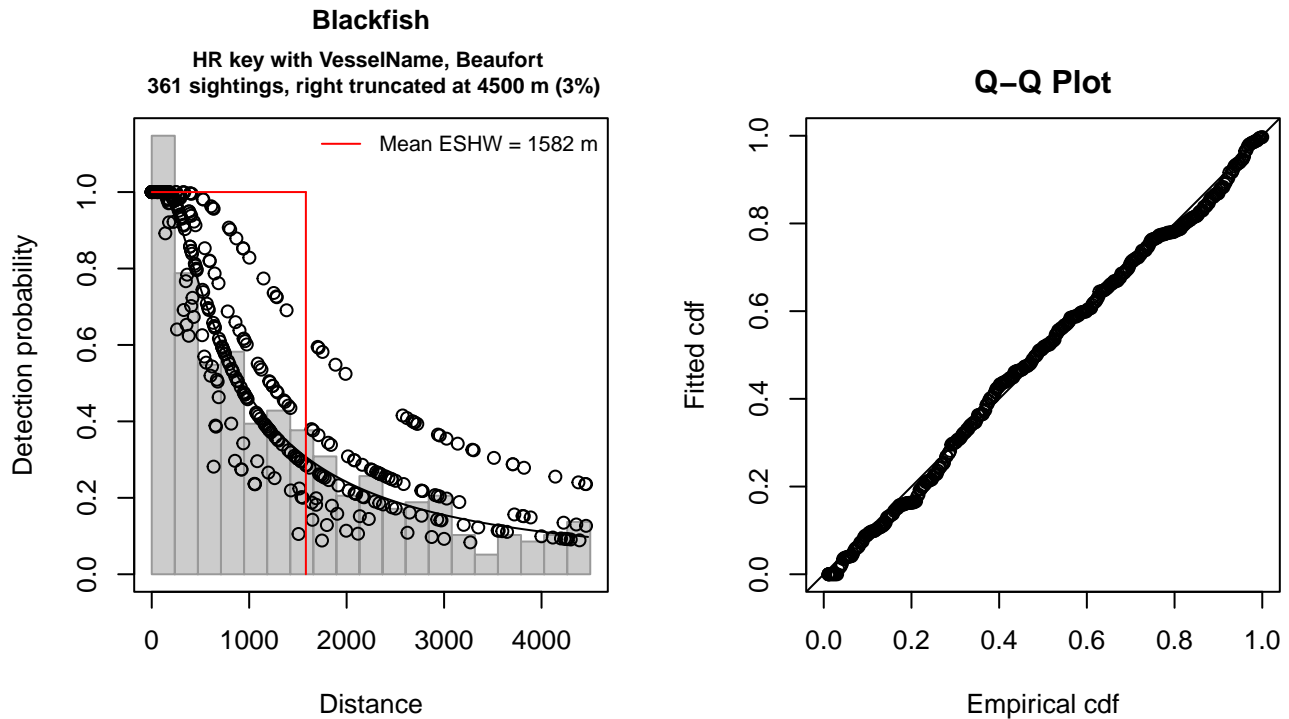


Figure 25: SEFSC detection function and Q-Q plot showing its goodness of fit.

Statistical output for this detection function:

Summary for ds object

Number of observations : 361
 Distance range : 0 - 4500
 AIC : 5876.279

Detection function:

Hazard-rate key function

Detection function parameters

Scale coefficient(s):

	estimate	se
(Intercept)	7.3597538	0.3426685
VesselNameOregon II	-0.5805409	0.4158932
Beaufort2	-0.5439643	0.4011114
Beaufort3-4	-0.8577400	0.3820711
Beaufort5	-1.2038982	0.5170081

Shape coefficient(s):

	estimate	se
(Intercept)	0.2309157	0.1254747

	Estimate	SE	CV
Average p	0.3253837	0.03477386	0.1068703
N in covered region	1109.4594048	128.24893603	0.1155959

Distance sampling Cramer-von Mises test (unweighted)

Test statistic = 0.112666 p = 0.526278

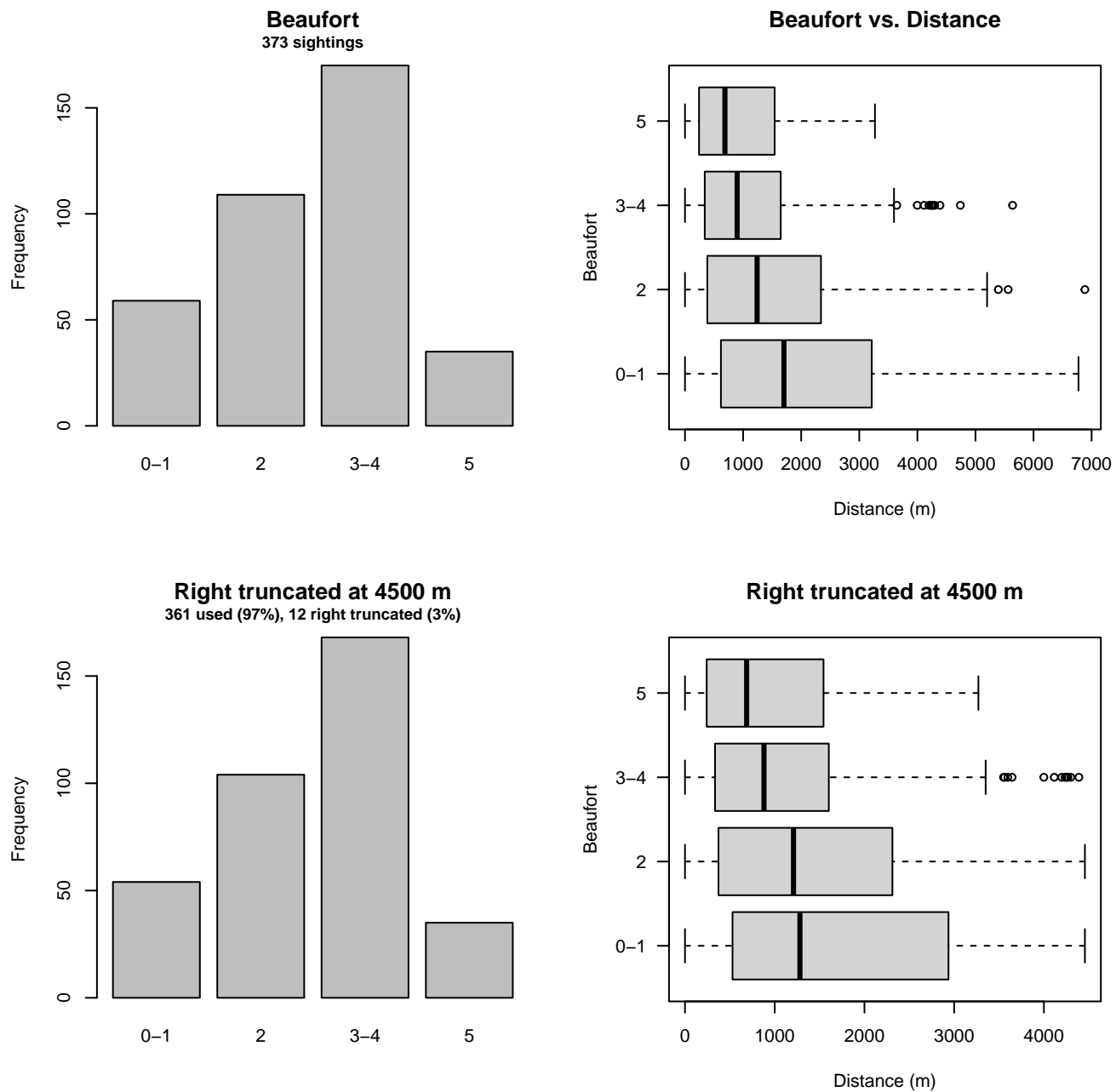


Figure 26: Distribution of the Beaufort covariate before (top row) and after (bottom row) observations were truncated to fit the SEFSC detection function.

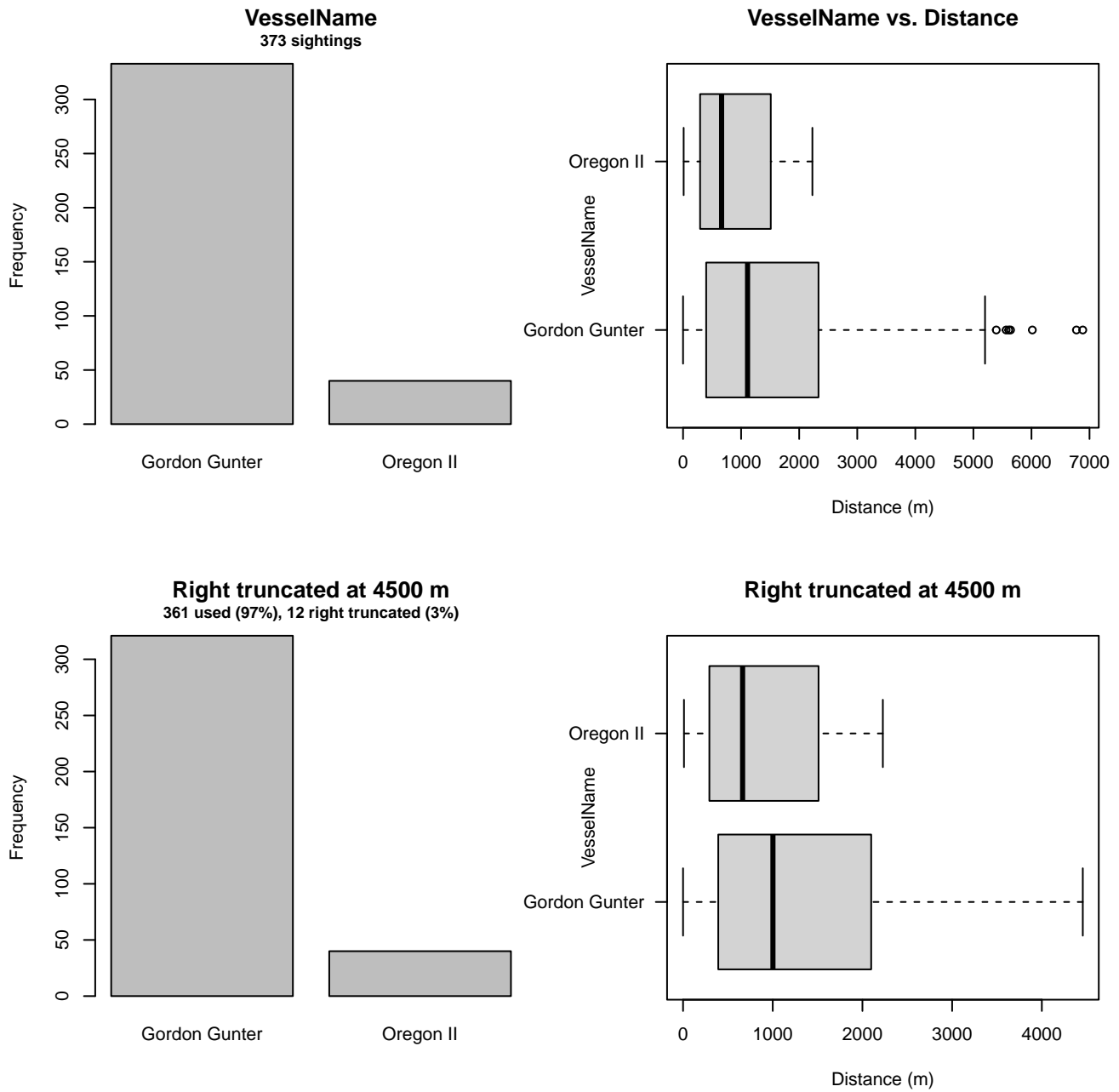


Figure 27: Distribution of the VesselName covariate before (top row) and after (bottom row) observations were truncated to fit the SEFSC detection function.

2.2.1.1.2 Song of the Whale

After right-truncating observations greater than 1500 m, we fitted the detection function to the 86 observations that remained (Table 5). The selected detection function (Figure 28) used a hazard rate key function with Beaufort (Figure 29) and Clouds (Figure 30) as covariates.

Table 5: Observations used to fit the Song of the Whale detection function.

ScientificName	n
Globicephala	48
Globicephala macrorhynchus	10
Globicephala melas	3
Grampus griseus	15
Orcinus orca	6
Pseudorca crassidens	4
Total	86

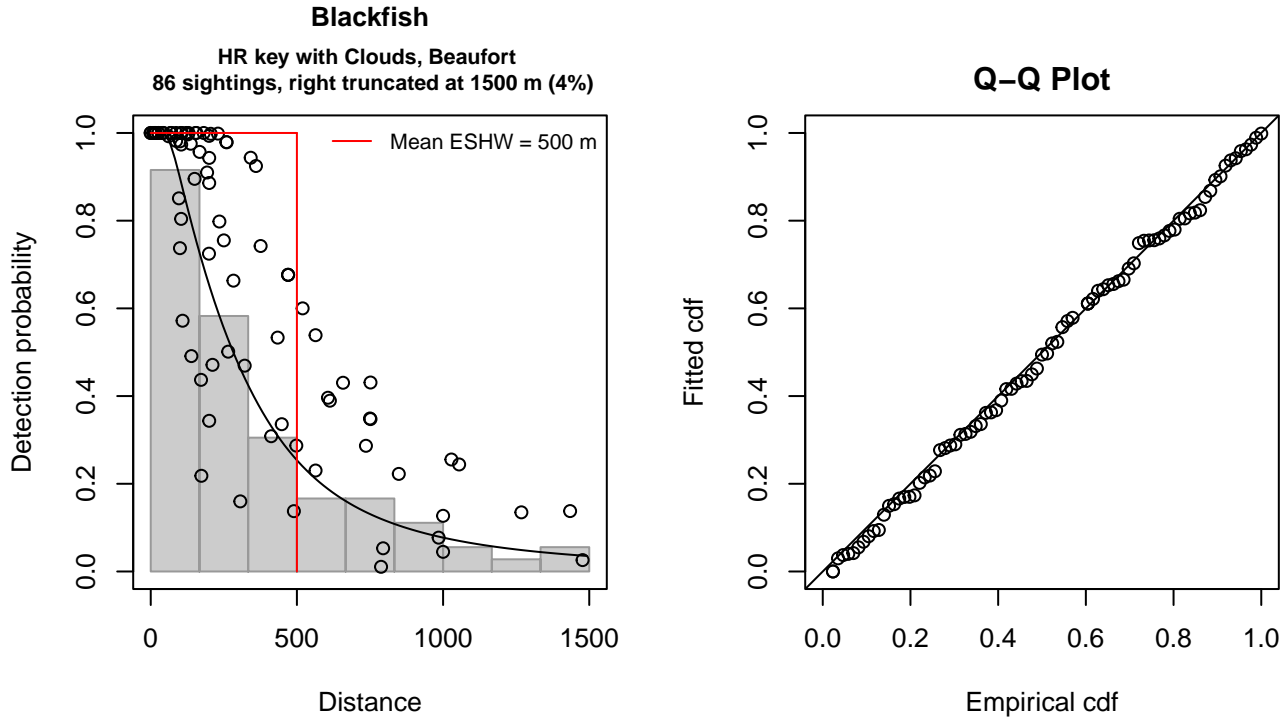


Figure 28: Song of the Whale detection function and Q-Q plot showing its goodness of fit.

Statistical output for this detection function:

```
Summary for ds object
Number of observations : 86
Distance range       : 0 - 1500
AIC                  : 1170.598
```

```
Detection function:
Hazard-rate key function
```

```
Detection function parameters
Scale coefficient(s):
      estimate      se
(Intercept) 6.4796997 0.26905817
Clouds      -0.1344265 0.04822789
Beaufort3-4 -0.6588095 0.31406041
```

```
Shape coefficient(s):
      estimate      se
(Intercept) 0.7265327 0.1798353
```

	Estimate	SE	CV
Average p	0.265116	0.04508089	0.1700421
N in covered region	324.386340	63.44454836	0.1955833

Distance sampling Cramer-von Mises test (unweighted)
 Test statistic = 0.019751 p = 0.997226

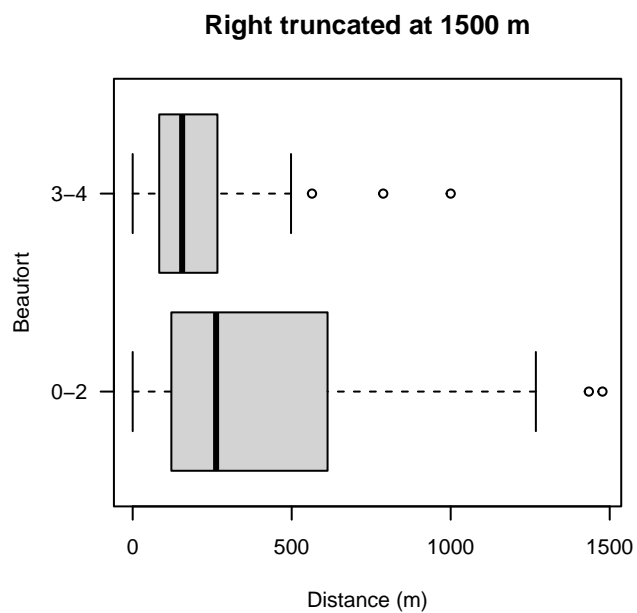
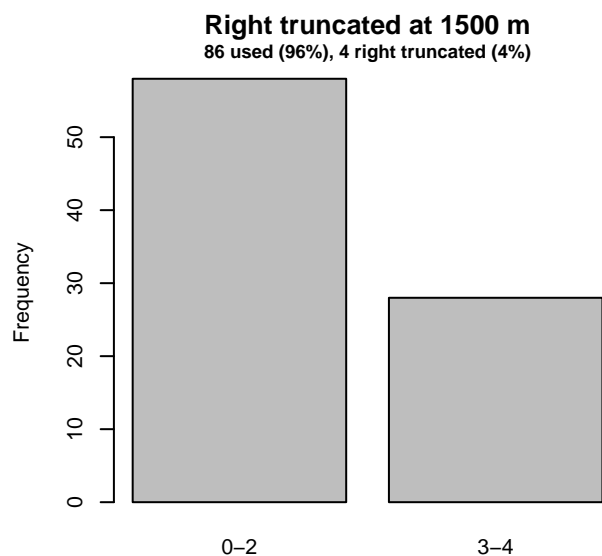
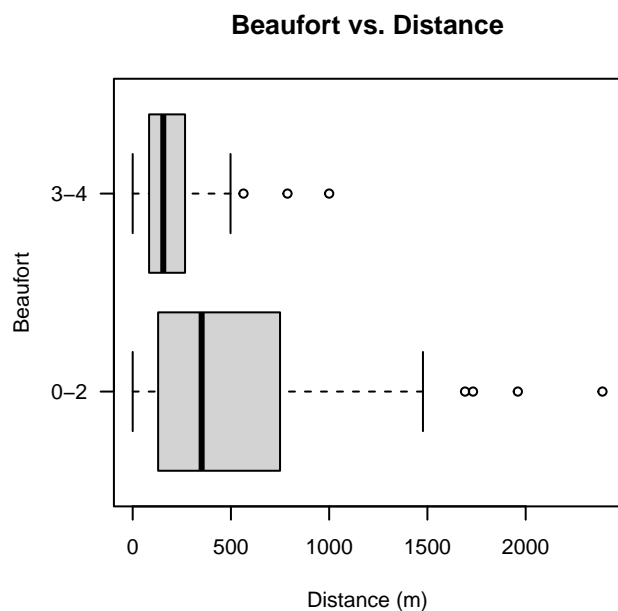
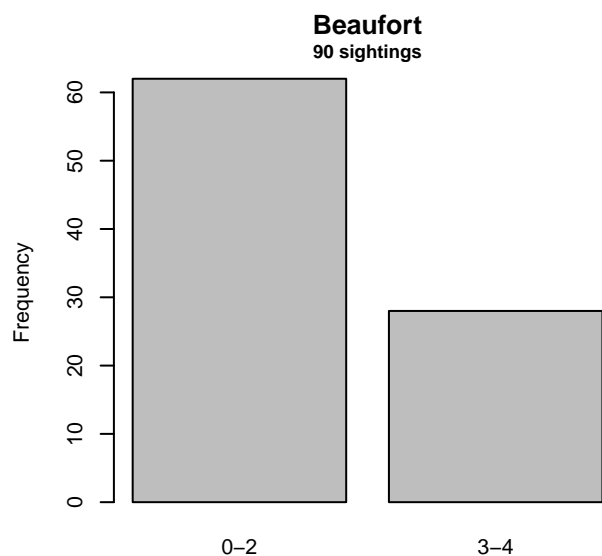


Figure 29: Distribution of the Beaufort covariate before (top row) and after (bottom row) observations were truncated to fit the Song of the Whale detection function.

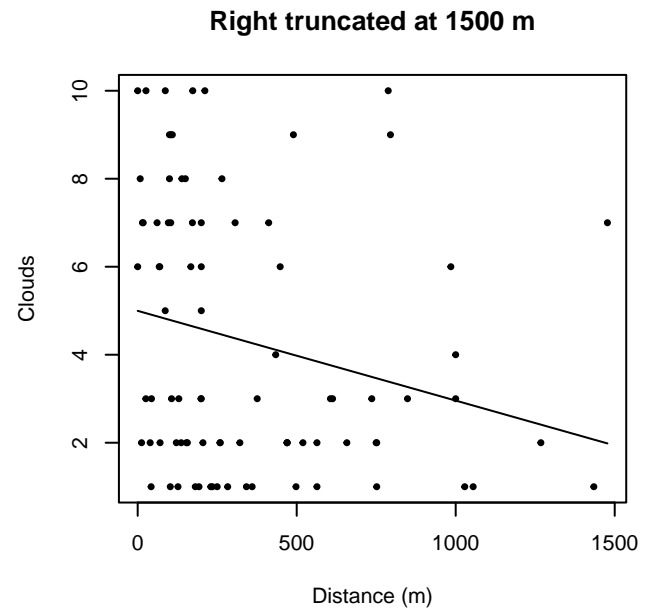
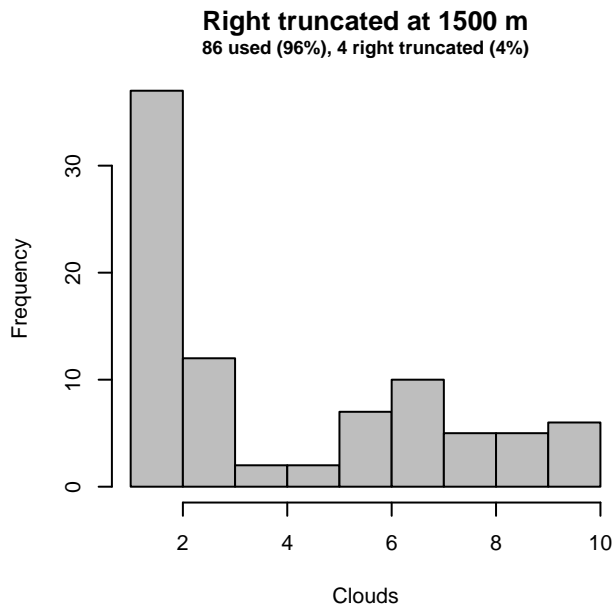
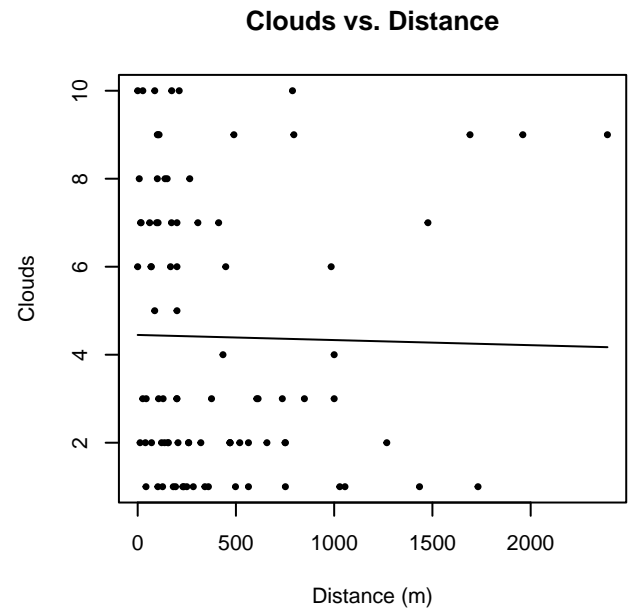
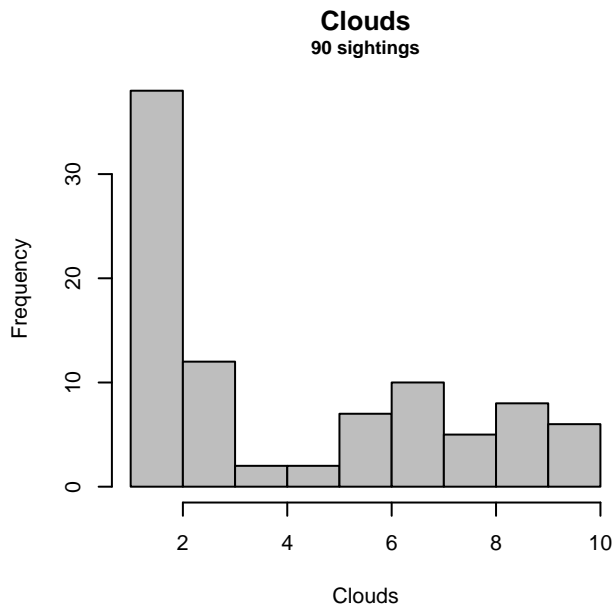


Figure 30: Distribution of the Clouds covariate before (top row) and after (bottom row) observations were truncated to fit the Song of the Whale detection function.

2.2.2 Pilot Whales and Risso’s Dolphin

2.2.2.1 Aerial Surveys

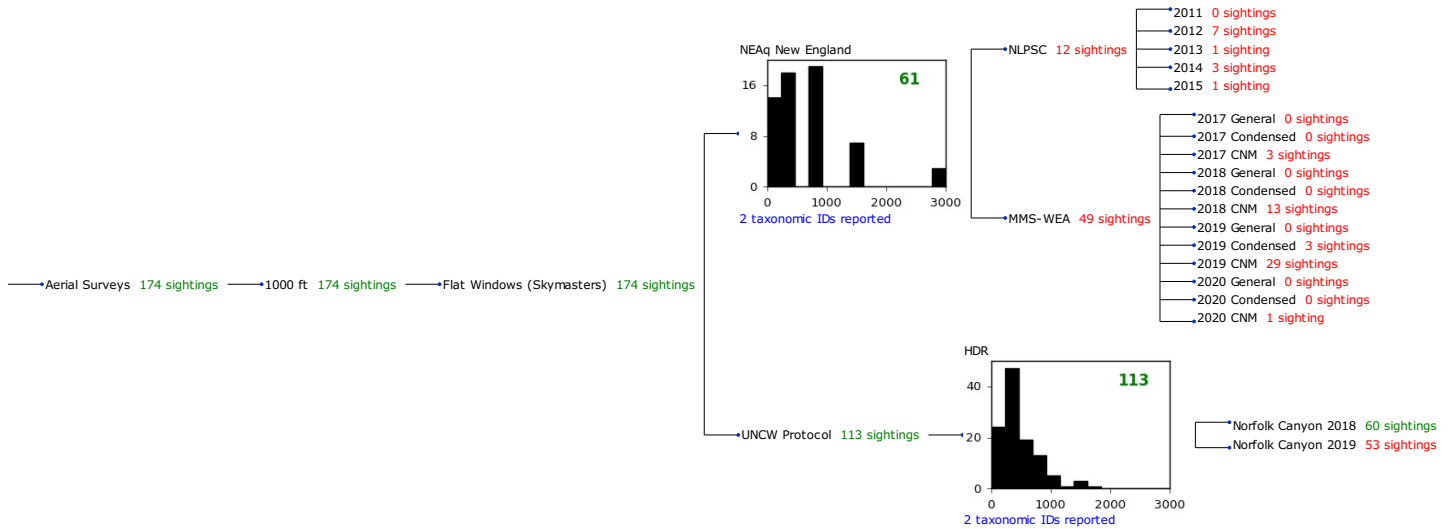


Figure 31: Detection hierarchy for aerial surveys, showing how they were pooled during detectability modeling, for detection functions that pooled multiple taxa but could not use a taxonomic covariate to account for differences between them. Each histogram represents a detection function and summarizes the perpendicular distances of observations that were pooled to fit it, prior to truncation. Observation counts, also prior to truncation, are shown in green when they met the recommendation of Buckland et al. (2001) that detection functions utilize at least 60 sightings, and red otherwise. For rare taxa, it was not always possible to meet this recommendation, yielding higher statistical uncertainty. During the spatial modeling stage of the analysis, effective strip widths were computed for each survey using the closest detection function above it in the hierarchy (i.e. moving from right to left in the figure). Surveys that do not have a detection function above them in this figure were either addressed by a detection function presented in a different section of this report, or were omitted from the analysis.

2.2.2.1.1 NEAq New England

After right-truncating observations greater than 1852 m and left-truncating observations less than 71 m (Figure 33), we fitted the detection function to the 58 observations that remained (Table 6). The selected detection function (Figure 32) used a half normal key function with no covariates.

Table 6: Observations used to fit the NEAq New England detection function.

ScientificName	n
Globicephala	16
Grampus griseus	42
Total	58

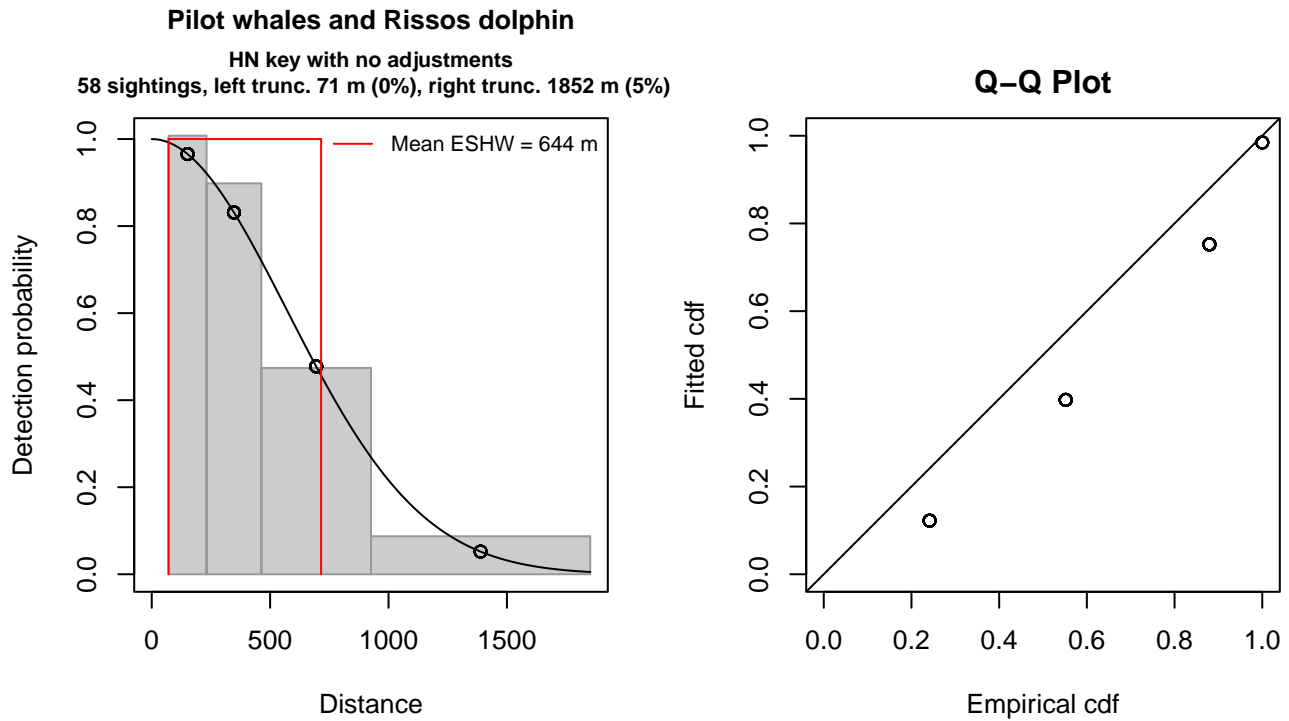


Figure 32: NEAq New England detection function and Q-Q plot showing its goodness of fit.

Statistical output for this detection function:

Summary for ds object

Number of observations : 58
Distance range : 71 - 1852
AIC : 156.0466

Detection function:

Half-normal key function

Detection function parameters

Scale coefficient(s):

	estimate	se
(Intercept)	6.347853	0.1032999

	Estimate	SE	CV
Average p	0.3617668	0.04089634	0.1130461
N in covered region	160.3242530	24.72501947	0.1542188

Distance sampling Cramer-von Mises test (unweighted)

Test statistic = 0.430759 p = 0.060002

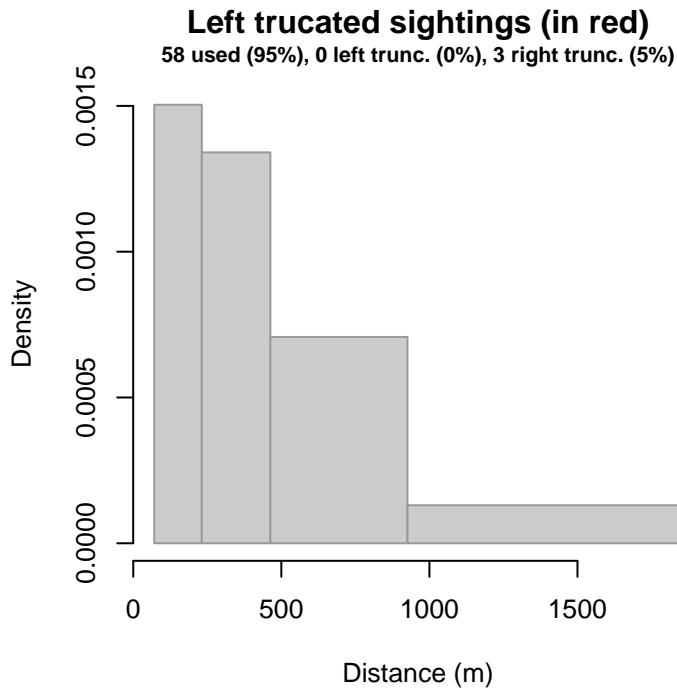


Figure 33: Density histogram of observations used to fit the NEAq New England detection function, with the left-most bar showing observations at distances less than 71 m, which were left-truncated and excluded from the analysis [Buckland et al. (2001)]. (This bar may be very short if there were very few left-truncated sightings, or very narrow if the left truncation distance was very small; in either case it may not appear red.)

2.2.2.1.2 HDR

After right-truncating observations greater than 1500 m and left-truncating observations less than 111 m (Figure 35), we fitted the detection function to the 108 observations that remained (Table 7). The selected detection function (Figure 34) used a hazard rate key function with Swell (Figure 36) as a covariate.

Table 7: Observations used to fit the HDR detection function.

ScientificName	n
Globicephala	66
Grampus griseus	42
Total	108

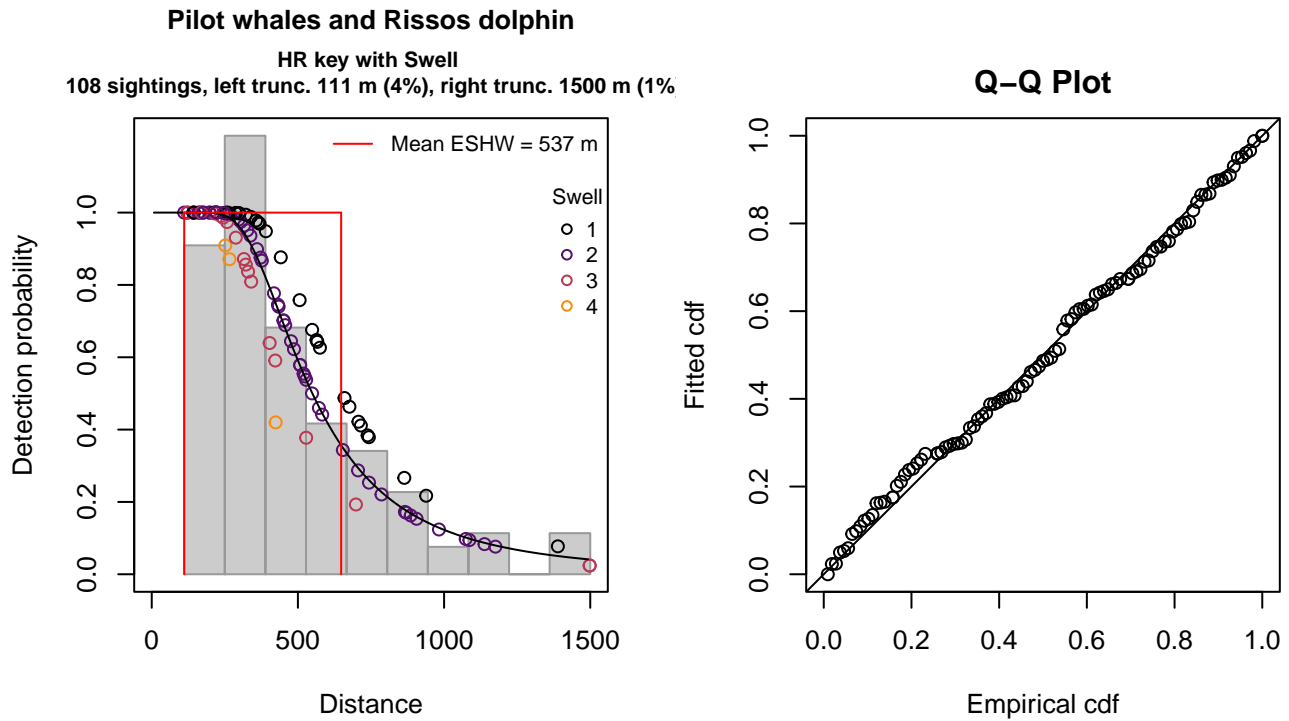


Figure 34: HDR detection function and Q-Q plot showing its goodness of fit.

Statistical output for this detection function:

Summary for ds object

Number of observations : 108
Distance range : 111 - 1500
AIC : 1479.102

Detection function:

Hazard-rate key function

Detection function parameters

Scale coefficient(s):

	estimate	se
(Intercept)	6.5207075	0.2852850
Swell	-0.1712662	0.1474231

Shape coefficient(s):

	estimate	se
(Intercept)	1.044626	0.1820091

	Estimate	SE	CV
Average p	0.3789427	0.04750114	0.1253518
N in covered region	285.0035382	41.82280744	0.1467449

Distance sampling Cramer-von Mises test (unweighted)

Test statistic = 0.045799 p = 0.901252

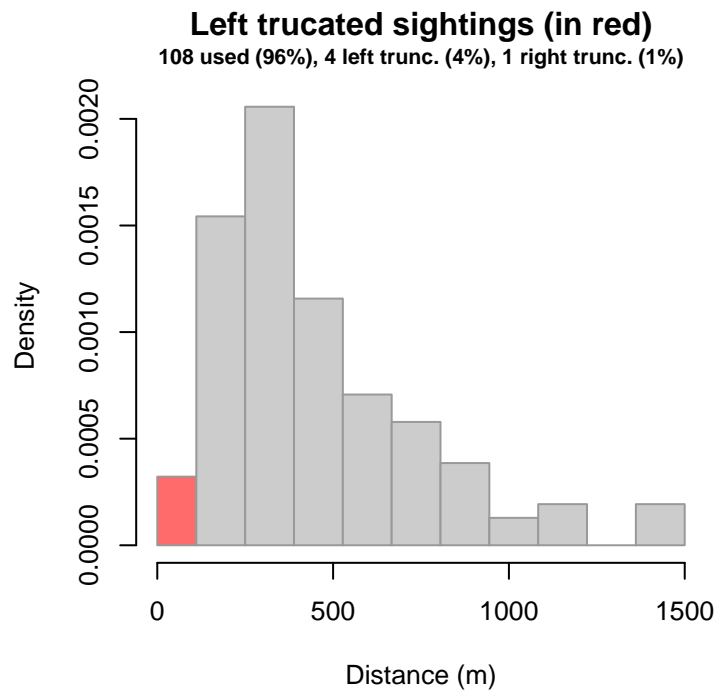


Figure 35: Density histogram of observations used to fit the HDR detection function, with the left-most bar showing observations at distances less than 111 m, which were left-truncated and excluded from the analysis [Buckland et al. (2001)]. (This bar may be very short if there were very few left-truncated sightings, or very narrow if the left truncation distance was very small; in either case it may not appear red.)

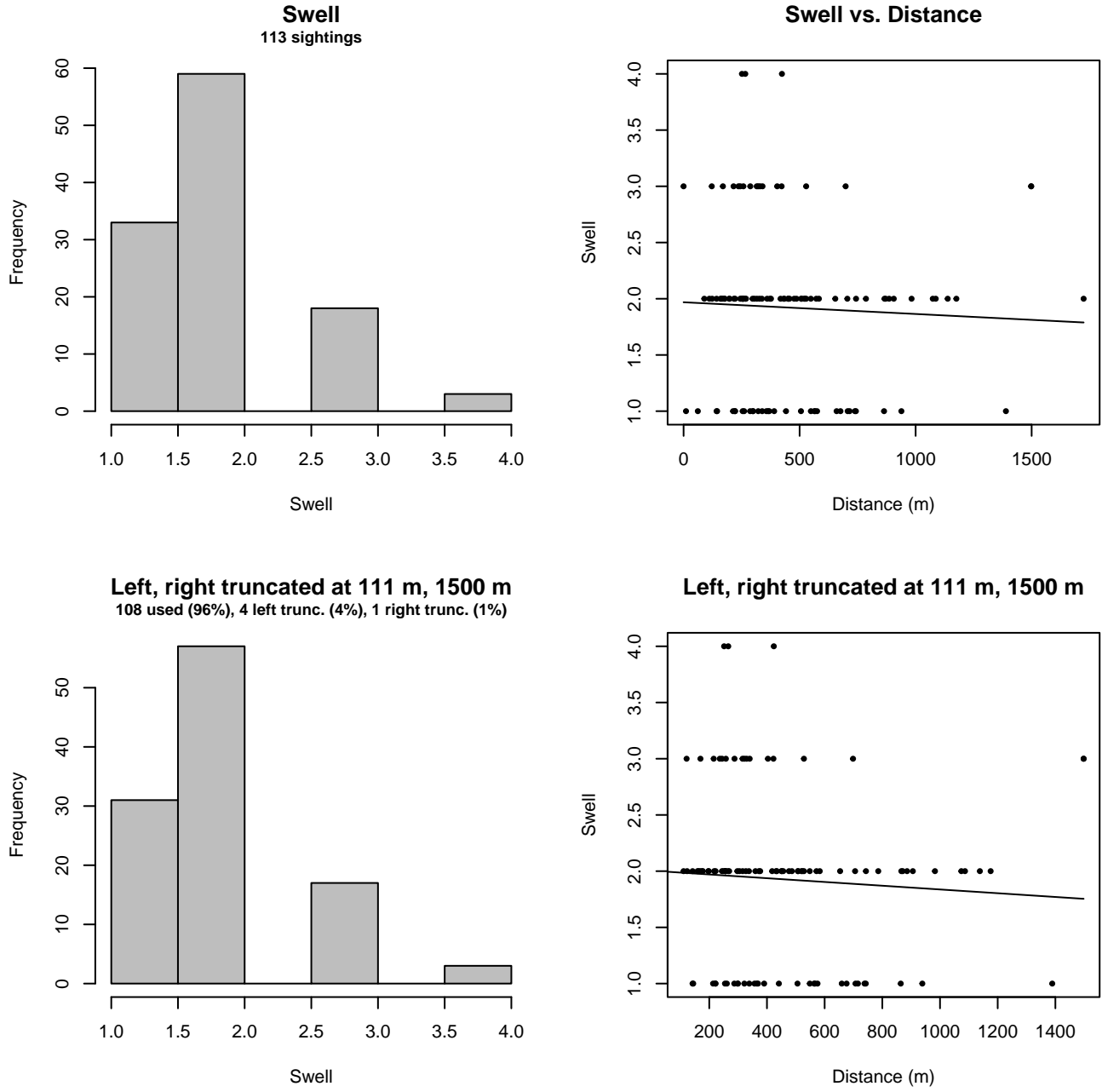


Figure 36: Distribution of the Swell covariate before (top row) and after (bottom row) observations were truncated to fit the HDR detection function.

3 Bias Corrections

Density surface modeling methodology uses *distance sampling* (Buckland et al. 2001) to model the probability that an observer on a line transect survey will detect an animal given the perpendicular distance to it from the transect line. Distance sampling assumes that detection probability is 1 when perpendicular distance is 0. When this assumption is not met, detection probability is biased high, leading to an underestimation of density and abundance. This is known as the $g_0 < 1$ problem, where g_0 refers to the detection probability at distance 0. Modelers often try to address this problem by estimating g_0 empirically and dividing it into estimated density or abundance, thereby correcting those estimates to account for the animals that were presumed missed.

Two important sources of bias for visual surveys are known as *availability bias*, in which an animal was present on the transect line but impossible to detect, e.g. because it was under water, and *perception bias*, in which an animal was present and available but not noticed, e.g. because of its small size or cryptic coloration or behavior (Marsh and Sinclair 1989). Modelers often

estimate the influence of these two sources of bias on detection probability independently, yielding two estimates of g_0 , hereafter referred to as g_{0A} and g_{0P} , and multiply them together to obtain a final, combined estimate: $g_0 = g_{0A} \cdot g_{0P}$.

Our overall approach was to perform this correction on a per-observation basis, to have the flexibility to account for many factors such as platform type, surveyor institution, group size, group composition (e.g. singleton, mother-calf pair, or surface active group), and geographic location (e.g. feeding grounds vs. calving grounds). The level of complexity of the corrections varied by species according to the amount of information available, with North Atlantic right whale having the most elaborate corrections, derived from a substantial set of publications documenting its behavior, and various lesser known odontocetes having corrections based only on platform type (aerial or shipboard), derived from comparatively sparse information. Here we document the corrections used for Risso’s dolphin.

3.1 Aerial Surveys

Palka et al. (2021) developed perception bias corrections using two team, mark recapture distance sampling (MRDS) methodology (Burt et al. 2014) for aerial surveys conducted in 2010-2017 by NOAA NEFSC and SEFSC during the AMAPPS program. These were the only extant perception bias estimates developed from aerial surveys used in our analysis, aside from estimates developed earlier by Palka and colleagues (Palka 2006; Palka et al. 2017). Those earlier efforts utilized older methods and less data than their 2021 analysis, so we applied the Palka et al. (2021) estimates to all aerial survey programs (Table 8).

We applied Palka’s estimate for NEFSC to all programs other than SEFSC on the basis that those programs employed a similar visual scanning protocol that allowed observers to scan from the trackline up to the horizon, while SEFSC’s protocol generally limited scanning only up to 50° from the trackline. In other species, NEFSC usually has a wider right truncation distance, which we interpret as being related to this scanning behavior. Additionally, the NEFSC estimate was made specifically for Risso’s dolphin without pooling other species, while the SEFSC estimate was approximately 50/50 pilot whales and Risso’s dolphin.

For all aerial surveys, to account for the influence of large group sizes on perception bias, we followed Carretta et al. (2000) and set the perception bias correction factor for sightings of more than 25 animals to $g_{0P} = 0.994$. Roughly 96% of NEFSC’s and 88% of SEFSC’s sightings were of 25 animals or less.

We caution that it is possible that perception bias was different on the other aerial programs, as they often used different aircraft, flew at different altitudes, and were staffed by different personnel. Of particular concern are that many programs flew Cessna 337 Skymasters, which had flat windows, while NOAA flew de Havilland Twin Otters, which had bubble windows, which likely afforded a better view of the transect line and therefore might have required less of a correction than the Skymasters. Correcting the other programs using NOAA’s estimate as we have done is likely to yield less bias than leaving them uncorrected, but we urge all programs to undertake their own efforts to estimate perception bias, as resources allow.

We estimated availability bias corrections using the Laake et al. (1997) estimator and dive intervals reported by Palka et al. (2017) (Table 9). To estimate time in view, needed by the Laake estimator, we used results reported by Robertson et al. (2015), rescaled linearly for each survey program according to its target altitude and speed. We caution that Robertson’s analysis was done for a de Havilland Twin Otter, which may have a different field of view than that of the other aircraft used here, which mainly comprised Cessna 337 Skymasters with flat windows but also a Partenavia P-68 with bubble windows (on the NYS-DEC/TT surveys). However, we note that McLellan et al. (2018) conducted a sensitivity analysis on the influence of the length of the “window of opportunity” to view beaked whales from a Cessna Skymaster on their final density estimates and found that they varied by only a few thousandths of an animal per kilometer when the window of opportunity more than doubled. Still, we urge additional program-specific research into estimation of availability bias.

To address the influence of group size on availability bias, we applied the group availability estimator of McLellan et al. (2018) on a per-observation basis. Following Palka et al. (2021), who also used that method, we assumed that individuals in the group dived asynchronously. The resulting g_{0A} corrections ranged from 0.695 to 1 (Figure 37). We caution that the assumption of asynchronous diving can lead to an underestimation of density and abundance if diving is actually synchronous; see McLellan et al. (2018) for an exploration of this effect. However, if future research finds that this species conducts synchronous dives and characterizes the degree of synchronicity, the model can be updated to account for this knowledge.

Table 8: Perception bias corrections for Risso’s dolphin applied to aerial surveys.

Surveys	Group Size	g_{0P}	g_{0P} Source
SEFSC	≤ 25	0.74	Palka et al. (2021): SEFSC
All others	≤ 25	0.62	Palka et al. (2021): NEFSC
All	> 25	0.99	Caretta et al. 2000

Table 9: Surface and dive intervals for Risso’s dolphin used to estimate availability bias corrections.

Surface Interval (s)	Dive Interval (s)	Source
322	175.1	Palka et al. (2017)

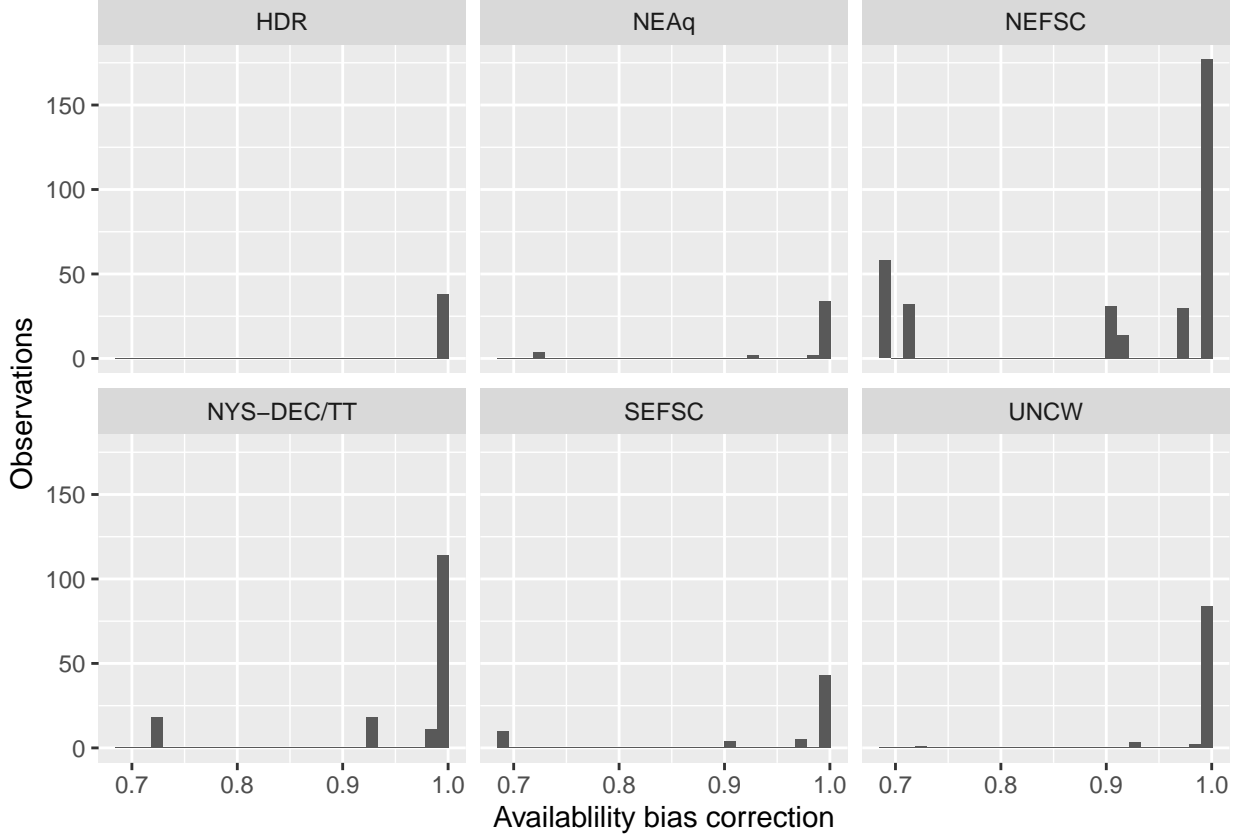


Figure 37: Availability bias corrections for Risso’s dolphin for aerial surveys, by institution.

3.2 Shipboard Surveys

Most of the shipboard surveys in our analysis used high-power (25x150), pedestal-mounted binoculars. Similar to aerial surveys, Palka et al. (2021) developed perception bias corrections using two team, MRDS methodology (Burt et al. 2014) for high-power binocular surveys conducted in 2010-2017 by NOAA NEFSC and SEFSC during the AMAPPS program. These were the only extant perception bias estimates developed from high-power binocular surveys used in our analysis, aside from estimates developed earlier by Palka and colleagues (Palka 2006; Palka et al. 2017). Those earlier efforts utilized older methods and less data than their 2021 analysis, so we applied the Palka et al. (2021) estimates to all shipboard surveys that searched with high-power binoculars (Table 10). Finally, for all shipboard binocular surveys, we set g_{0P} to 0.97 ($CV=0.017$) for sightings of 21 or more animals, following Barlow and Rankin (2007).

For naked eye surveys, we only had Song of the Whale (MCR). We omitted NESFC AJ 99-02 because it did not sight any Risso’s dolphins. For the Song of the Whale surveys, we could not find a perception bias estimate in the literature for Risso’s dolphins from similar surveys. As a proxy, we used the pilot whale perception bias estimate from Cañadas et al. (2021).

Dive times for dolphins are short enough that availability bias is not expected to be significant for dolphins observed from shipboard surveys. Therefore, following prior models (Roberts et al. 2016; Palka et al. 2021), we assumed that $g_{0A} = 1$.

Table 10: Perception and availability bias corrections for Risso’s dolphin applied to shipboard surveys.

Surveys	Searching Method	Group Size	g_{0P}	g_{0P} Source	g_{0A}	g_{0A} Source
NEFSC	Binoculars	≤ 20	0.50	Palka et al. (2021): NEFSC	1	Assumed
SEFSC	Binoculars	≤ 20	0.71	Palka et al. (2021): SEFSC	1	Assumed
All	Binoculars	> 20	0.97	Barlow and Forney (2007)	1	Assumed
MCR	Naked Eye	Any	0.74	Canadas (pers comm)	1	Assumed

4 Density Model

Risso’s dolphin is a widespread species found in tropical and temperate waters, preferring temperate continental shelf and slope waters between 30-45 degrees latitude to oceanic depths (Jefferson et al. 2014). These habitat preferences appear to hold throughout much or all of the species’ range (Jefferson et al. 2014). This description is consistent with the sightings reported by the surveys used in our models: most sightings occurred on the continental slope close to the shelf break, while fewer sightings occurred on the shelf and in waters deeper than the slope. No sightings of Risso’s dolphin occurred along the southeastern shelf of the study region where we had a high concentration of survey effort. As such, we excluded this region from our model, to avoid confounding covariate relationships with data from this region of clear absence, and explicitly set density to zero there.

Off the northeastern U.S. coast, the population is reported to occupy the mid-Atlantic continental shelf year-round. Seasonal variation is reported for this species. Hayes et al. (2022) reports Risso’s dolphin distribution from Cape Hatteras to Georges Bank during spring, summer and fall (Winn 1982; Payne 1984), contracting southward in winter, concentrated in the mid-Atlantic and extending into offshore oceanic waters (Payne 1984). Risso’s dolphin sightings have been reported to be associated with strong oceanographic features such as warm core rings and the north wall of the Gulf Stream (Waring et al. 1992; Waring et al. 1993; Hamazaki 2002). Reporting further evidence of seasonal variation in distribution, Cohen et al. (2022) used machine learning followed by expert review to classify echolocation clicks in acoustic data collected at 11 autonomous monitoring sites in the western North Atlantic between 2016 and 2019. This study found that Risso’s dolphin showed a predominantly northerly distribution, although it was present at every acoustic monitoring site in every season. A clear seasonal pattern was visible, with highest presence at Wilmington Canyon, Babylon Canyon, and Nantucket Canyon in the spring shifting northward to highest presence at Nantucket Canyon, Oceanographer’s Canyon, and Heezen Canyon in the summer and into the fall, and winter presence was found to be lower at all of the northern sites. Risso’s dolphin was present at the southern sites year-round with highest presence in spring and summer (Cohen et al. 2022).

Together, these studies indicate that Risso’s dolphins are present throughout the year, and their distribution shows monthly variability. Given this evidence, we modeled Risso’s dolphin abundance with a single, year-round model and determined it was most appropriate to provide monthly predictions.

Due to the large number of sightings available we eliminated data prior to 1998 and also excluded 2020 from the models in order to utilize micronekton biomass estimates from SEAPODYM (Lehodey et al. 2008), distance to eddies, and kinetic energy covariates, which preliminary modeling indicated were effective spatial covariates but were only available through 2019.

The model selection procedure was straightforward. When ranked by REML score (Wood 2011), the highest ranked models with climatological covariates outranked those with contemporaneous covariates, and explained nearly 1% more deviance.

The final Risso’s dolphin model contained almost 1 million km of segments with 1,062 total sightings of groups. The top model selected with the highest explained deviance and lowest AIC and REML scores was a climatological model that retained 10 covariates (Table 11) (Figure 41). The retained covariates included a bivariate term, distance to the 300m isobath and sea surface salinity (SSS), and univariate terms; depth, slope, SST, bottom temperature, distance to canyons, total kinetic energy (TKE), distance to anticyclonic eddies, distance to front and epipelagic micronekton. The relationship to the bivariate interaction between distance to the 300m isobath and SSS showed that within 200 kilometers on either side of the isobath there was a preference for salinities between 33 and 35, with lower salinities also predicting more animals close to and offshore of the isobath. The relationship with depth showed animals increasing at depths above 100 meters, there was also a positive relationship to slope with more animals predicted at higher slopes. A positive increasing relationship to SST was predicted with abundance increasing above 10°C and again above 25°C. Next, there was a negative relationship to bottom temperature with animals decreasing at temperatures above 10°C. The relationship to distance to canyons showed

two peaks, the first close to canyons and the second beyond 150 kilometers from canyons. There was a negative relationship to total kinetic energy, showing that as total kinetic energy decreases so do the number of Risso’s dolphins predicted. In this study area, places of highest TKE are in the Gulf Stream and the highest numbers of sightings occur in or near the Gulf Stream, especially in the Cape Hatteras region. A negative relationship was also predicted for distance to anticyclonic eddies with decreasing abundance predicted further from eddies, and a similar relationship was shown for distance to fronts. This is consistent with prior studies that have reported Risso’s dolphin sightings associated with strong oceanographic features such as warm core rings and the north wall of the Gulf Stream Hamazaki (2002). Finally, the relationship to epipelagic micronekton showed abundance predictions decreasing at the highest biomass levels. Risso’s dolphins are known to feed on fish, krill, and cephalopods, and it was thought that they feed primarily at night, but recent work by Benoit-Bird et al. (2019) has shown that “Rather than being solely nocturnal . . . as previously suggested”, Risso’s dolphins regularly dove to depths exceeding 500 m both day and night and switched from being surface generalists to squid specialists at depth, often within the course of a single dive. The authors suggest that while shallow prey may provide only small energetic contributions to their diet, overall they play a strong role in determining spatio-temporal habitat use of the species.

4.1 Final Model

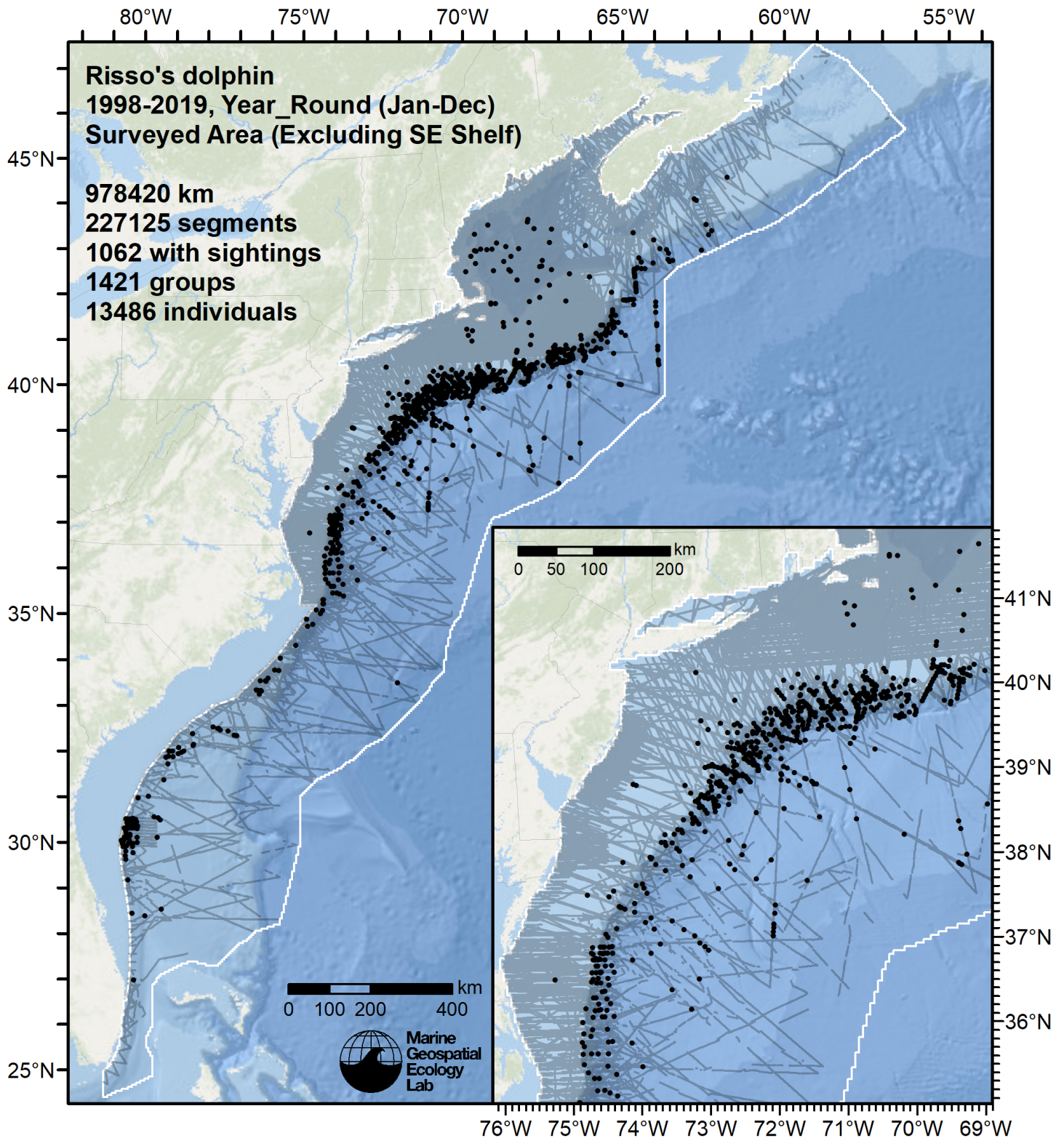


Figure 38: Survey segments used to fit the model for the region Surveyed Area (Excluding SE Shelf). Black points indicate segments with observations.

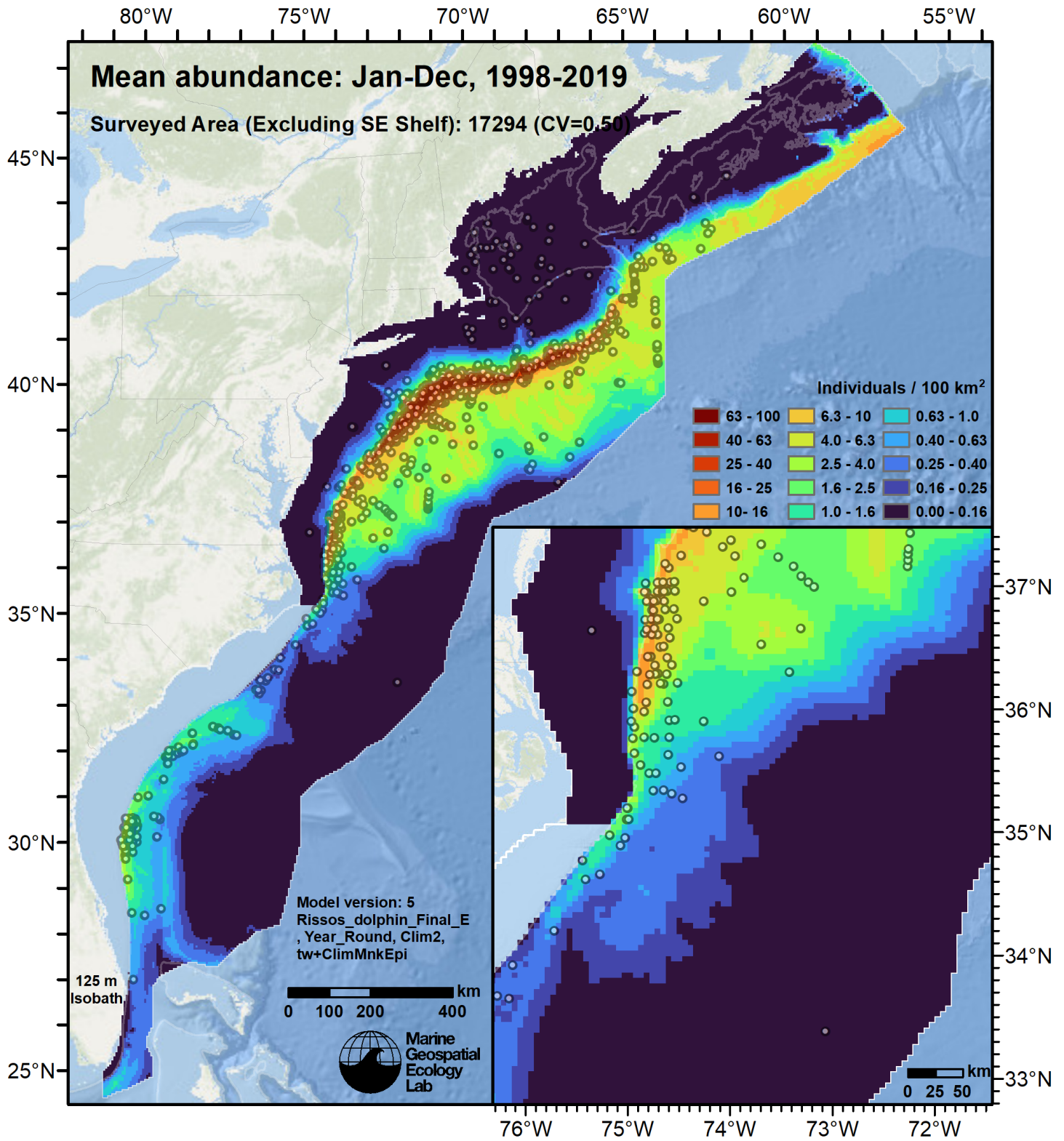


Figure 39: Risso's dolphin mean density for the indicated period, as predicted by the model for the region Surveyed Area (Excluding SE Shelf). Open circles indicate segments with observations. Mean total abundance and its coefficient of variation (CV) are given in the subtitle. Variance was estimated with the analytic approach given by Miller et al. (2022), Appendix S1, and accounts both for uncertainty in model parameter estimates and for seasonal variability in dynamic covariates but not interannual variability in them, as these covariates were monthly climatological averages.

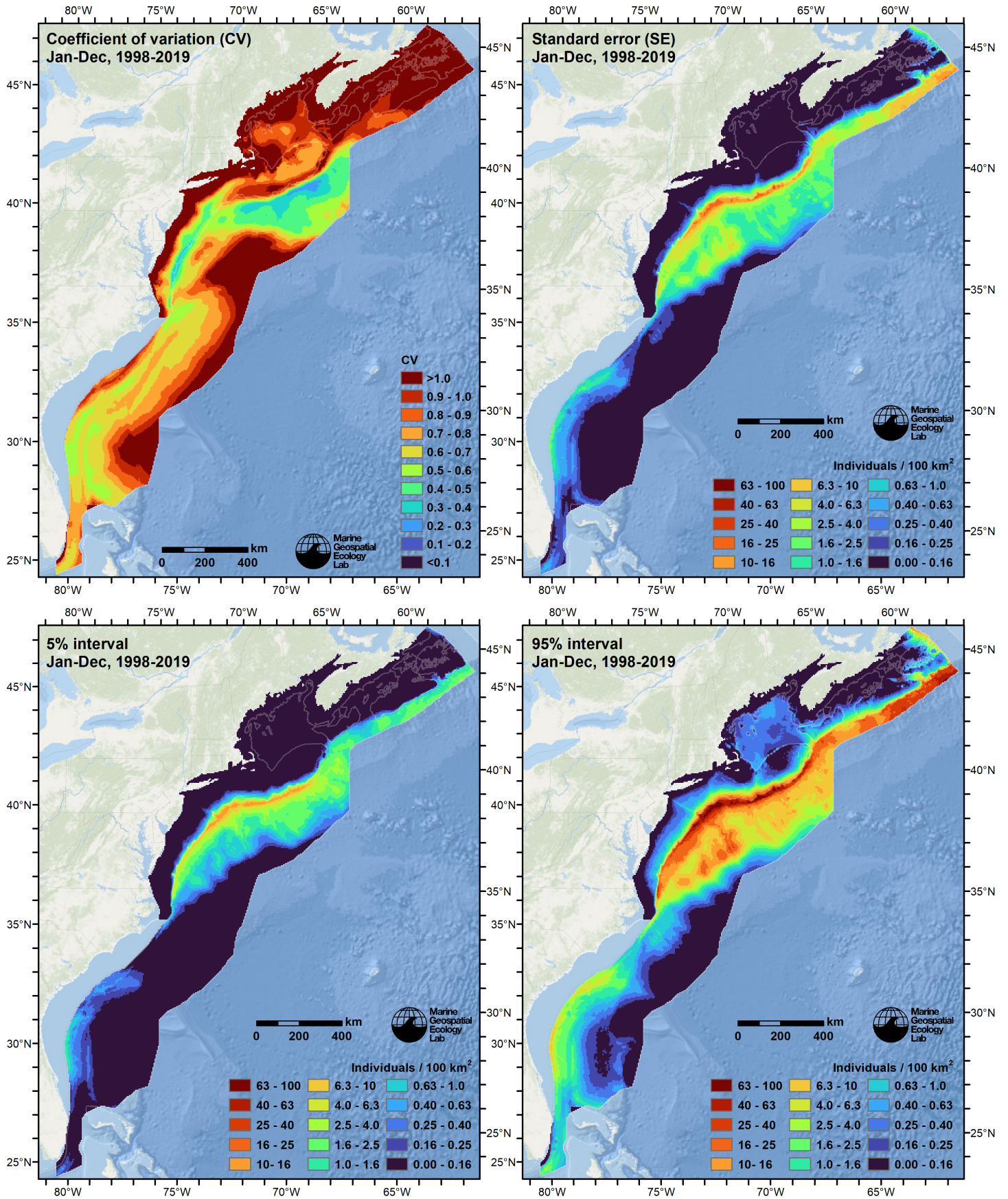


Figure 40: Uncertainty statistics for the Risso's dolphin mean density surface (Figure 39) predicted by the model for the region Surveyed Area (Excluding SE Shelf). Variance was estimated with the analytic approach given by Miller et al. (2022), Appendix S1, and accounts both for uncertainty in model parameter estimates and for seasonal variability in dynamic covariates but not interannual variability in them, as these covariates were monthly climatological averages.

Statistical output for this model:

Family: Tweedie(p=1.298)

Link function: log

Formula:

```
IndividualsCorrected ~ offset(log(SegmentArea)) + s(log10(pmax(10,
  Depth)), bs = "ts") + s(log10((pmax(0.3, pmin(Slope, 30))))),
  bs = "ts") + s(pmax(2.5, ClimSST_CMC), bs = "ts") + te(pmax(31.5,
  ClimSSS_HYCOM), (I(DistTo300m/1000)), bs = "ts") + s(pmax(3,
  pmin(ClimBotT_HYCOM, 25)), bs = "ts") + s(pmin(I(DistToCan/1000),
  350), bs = "ts") + s(log10(pmax(0.002, ClimTKE)), bs = "ts") +
  s(pmin(I(ClimDistToAEddy/1000), 450), bs = "ts") + s(pmin(I(ClimDistToFront063/1000),
  75), bs = "ts") + s(log10(pmax(0.01, ClimMnkEpi)), bs = "ts")
```

Parametric coefficients:

```
      Estimate Std. Error t value Pr(>|t|)
(Intercept) -21.0441      0.1231  -170.9   <2e-16 ***
---
```

Signif. codes: 0 '***' 0.001 '**' 0.01 '*' 0.05 '.' 0.1 ' ' 1

Approximate significance of smooth terms:

	edf	Ref.df	F	p-value
s(log10(pmax(10, Depth)))	7.0828	9	13.149	< 2e-16
s(log10((pmax(0.3, pmin(Slope, 30)))))	0.8606	9	0.575	0.010042
s(pmax(2.5, ClimSST_CMC))	7.2930	9	13.030	< 2e-16
te(pmax(31.5, ClimSSS_HYCOM),I(DistTo300m/1000))	8.3797	24	4.817	< 2e-16
s(pmax(3, pmin(ClimBotT_HYCOM, 25)))	2.2444	9	1.748	0.000115
s(pmin(I(DistToCan/1000), 350))	4.0162	9	4.936	< 2e-16
s(log10(pmax(0.002, ClimTKE)))	5.2294	9	9.090	< 2e-16
s(pmin(I(ClimDistToAEddy/1000), 450))	4.8293	9	2.431	7.17e-05
s(pmin(I(ClimDistToFront063/1000), 75))	1.0392	9	1.996	7.42e-06
s(log10(pmax(0.01, ClimMnkEpi)))	4.7775	9	6.654	< 2e-16

```
s(log10(pmax(10, Depth)))      ***
s(log10((pmax(0.3, pmin(Slope, 30)))))  *
s(pmax(2.5, ClimSST_CMC))      ***
te(pmax(31.5, ClimSSS_HYCOM),I(DistTo300m/1000)) ***
s(pmax(3, pmin(ClimBotT_HYCOM, 25)))    ***
s(pmin(I(DistToCan/1000), 350))          ***
s(log10(pmax(0.002, ClimTKE)))          ***
s(pmin(I(ClimDistToAEddy/1000), 450))    ***
s(pmin(I(ClimDistToFront063/1000), 75))  ***
s(log10(pmax(0.01, ClimMnkEpi)))        ***
---
```

Signif. codes: 0 '***' 0.001 '**' 0.01 '*' 0.05 '.' 0.1 ' ' 1

R-sq.(adj) = 0.0528 Deviance explained = 50.2%

-REML = 9204.7 Scale est. = 31.678 n = 227125

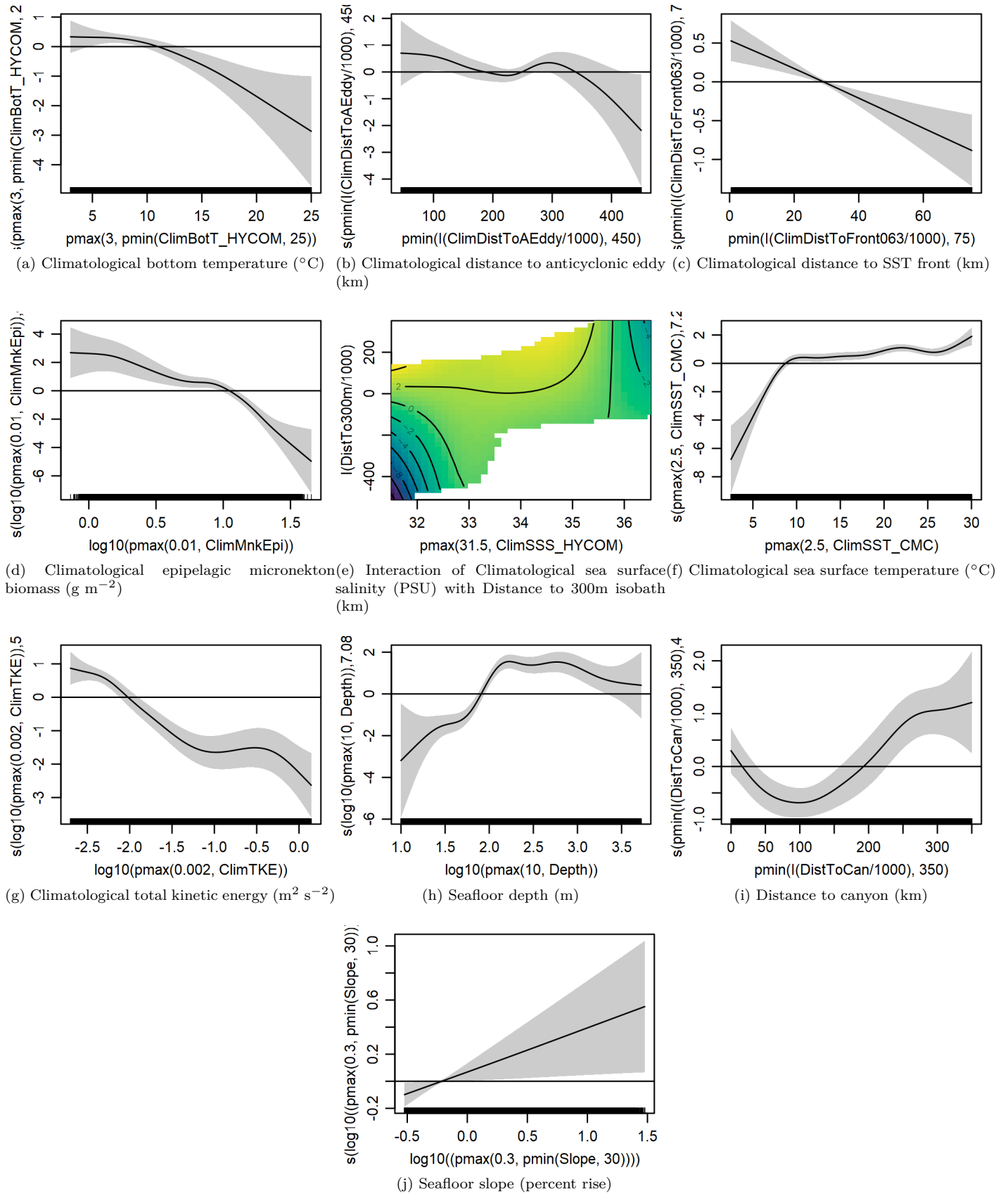


Figure 41: Functional plots for the final model for the region Surveyed Area (Excluding SE Shelf). Transforms and other treatments are indicated in axis labels. \log_{10} indicates the covariate was \log_{10} transformed. $pmax$ and $pmin$ indicate the covariate's minimum and maximum values, respectively, were Winsorized to the values shown. Winsorization was used to prevent runaway extrapolations during prediction when covariates exceeded sampled ranges, or for ecological reasons, depending on the covariate. $/1000$ indicates meters were transformed to kilometers for interpretation convenience.

Table 11: Covariates used in the final model for the region Surveyed Area (Excluding SE Shelf).

Covariate	Description
ClimBotT_HYCOM	Climatological monthly mean bottom temperature ($^{\circ}\text{C}$) from the HYCOM GOFS 3.1 1/12 $^{\circ}$ ocean model (Chassignet et al. (2009))
ClimDistToAEddy	Climatological monthly mean distance (km) to the edge of the closest anticyclonic mesoscale eddy of any age, derived with MGET (Roberts et al. (2010)) from the Aviso Mesoscale Eddy Trajectories Atlas (META2.0), produced by SSALTO/DUACS and distributed by AVISO+ (https://aviso.altimetry.fr) with support from CNES, in collaboration with Oregon State University with support from NASA, using the method of Schlax and Chelton (2016), based on Chelton et al. (2011)
ClimDistToFront063	Climatological monthly mean distance (km) to the closest sea surface temperature front detected in daily GHRSSST Level 4 CMC0.2deg and CMC0.1deg images (Brasnett (2008); Canada Meteorological Center (2012); Meissner et al. (2016); Canada Meteorological Center (2016)) with MGET's implementation of the Canny edge detector (Roberts et al. (2010); Canny (1986))
ClimMnkEpi	Climatological monthly mean micronekton biomass available in the epipelagic zone, expressed as wet weight (g m^{-2}), from SEAPODYM (Lehodey et al. (2008); Lehodey et al. (2015)), provided by E.U. Copernicus Marine Service. doi: 10.48670/moi-00020 . Computed as the sum of the SEAPODYM mnkc_epi, mnkc_mumeso, and mnkc_hmlmeso variables.
ClimSSS_HYCOM	Climatological monthly mean sea surface salinity (PSU) from the HYCOM GOFS 3.1 1/12 $^{\circ}$ ocean model (Chassignet et al. (2009))
ClimSST_CMC	Climatological monthly mean sea surface temperature ($^{\circ}\text{C}$) from GHRSSST Level 4 CMC0.2deg and CMC0.1deg (Brasnett (2008); Canada Meteorological Center (2012); Meissner et al. (2016); Canada Meteorological Center (2016))
ClimTKE	Climatological monthly mean total kinetic energy ($\text{m}^2 \text{s}^{-2}$) derived from Aviso Ssalto/Duacs global gridded L4 reprocessed geostrophic currents, produced and distributed by E.U. Copernicus Marine Service. doi: 10.48670/moi-00148
Depth	Depth (m) of the seafloor, from SRTM30_PLUS (Becker et al. (2009))
DistTo300m	Distance (km) to the 300m isobath, derived from SRTM30_PLUS (Becker et al. (2009))
DistToCan	Distance (km) to the closest submarine canyon, derived from the Harris et al. (2014) geomorphology
Slope	Slope (percent rise) of the seafloor, derived from SRTM30_PLUS (Becker et al. (2009))

4.2 Diagnostic Plots

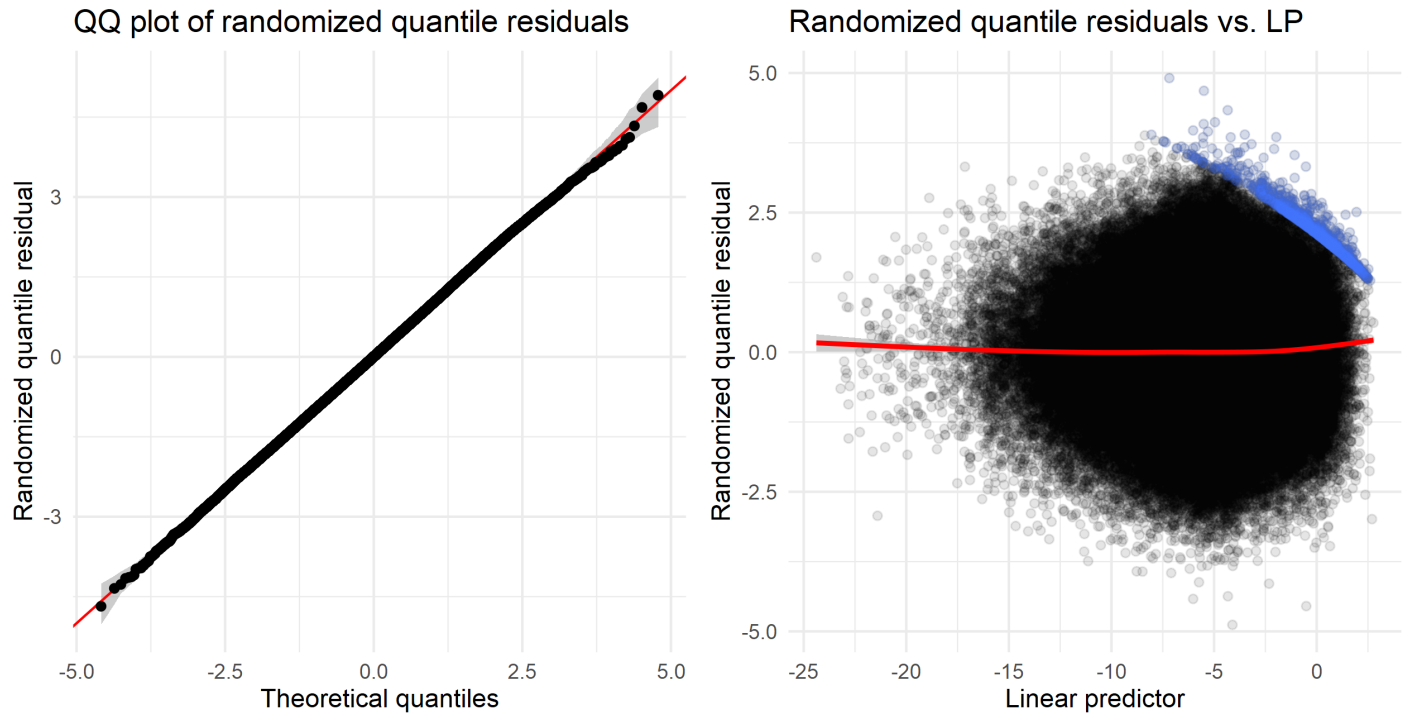


Figure 42: Residual plots for the final model for the region Surveyed Area (Excluding SE Shelf).

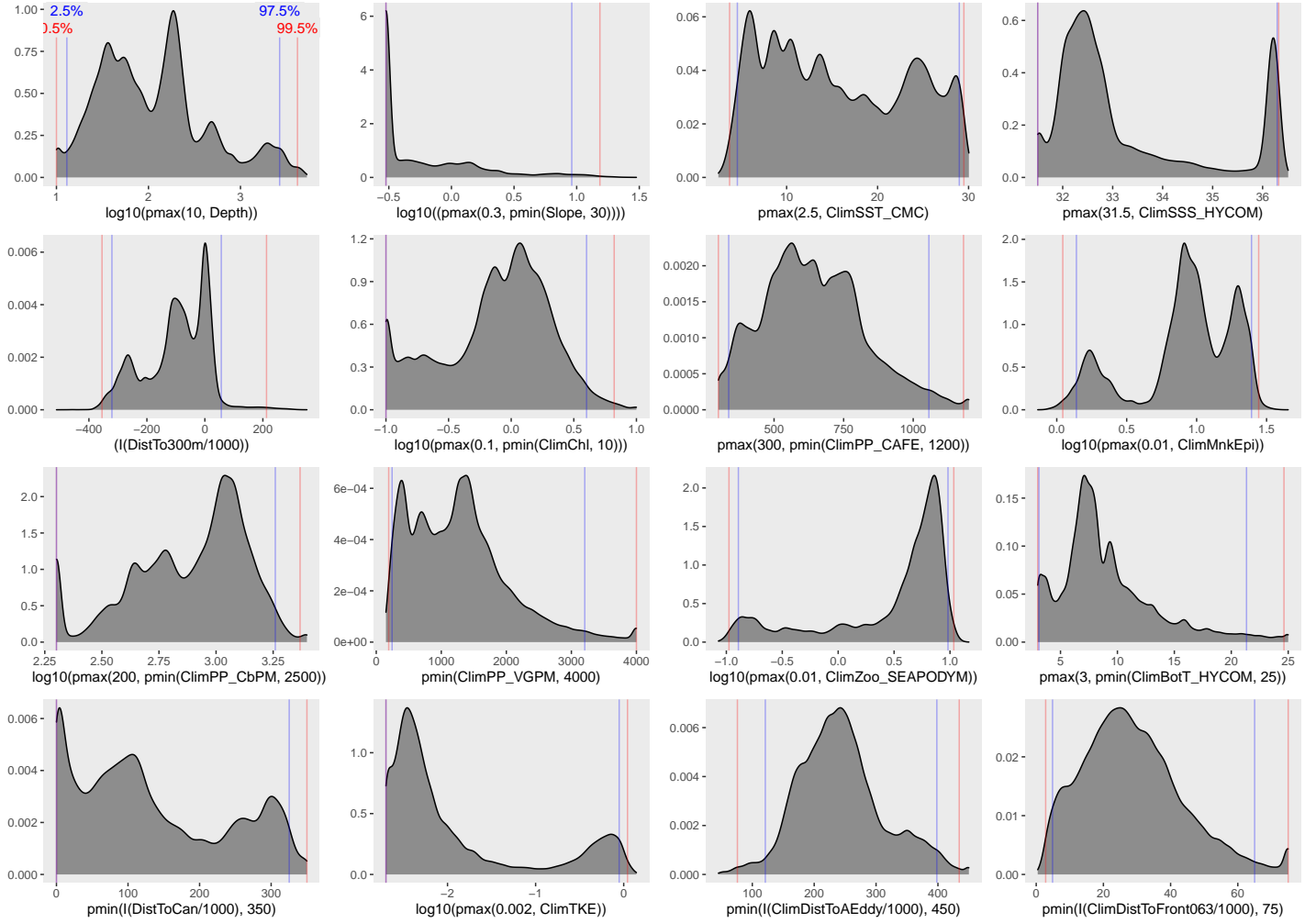


Figure 43: Density histograms showing the distributions of the covariates considered during the final model selection step. The final model may have included only a subset of the covariates shown here (see Figure 41), and additional covariates may have been considered in preceding selection steps. Red and blue lines enclose 99% and 95% of the distributions, respectively. Transforms and other treatments are indicated in axis labels. \log_{10} indicates the covariate was \log_{10} transformed. $pmax$ and $pmin$ indicate the covariate's minimum and maximum values, respectively, were Winsorized to the values shown. Winsorization was used to prevent runaway extrapolations during prediction when covariates exceeded sampled ranges, or for ecological reasons, depending on the covariate. $/1000$ indicates meters were transformed to kilometers for interpretation convenience.

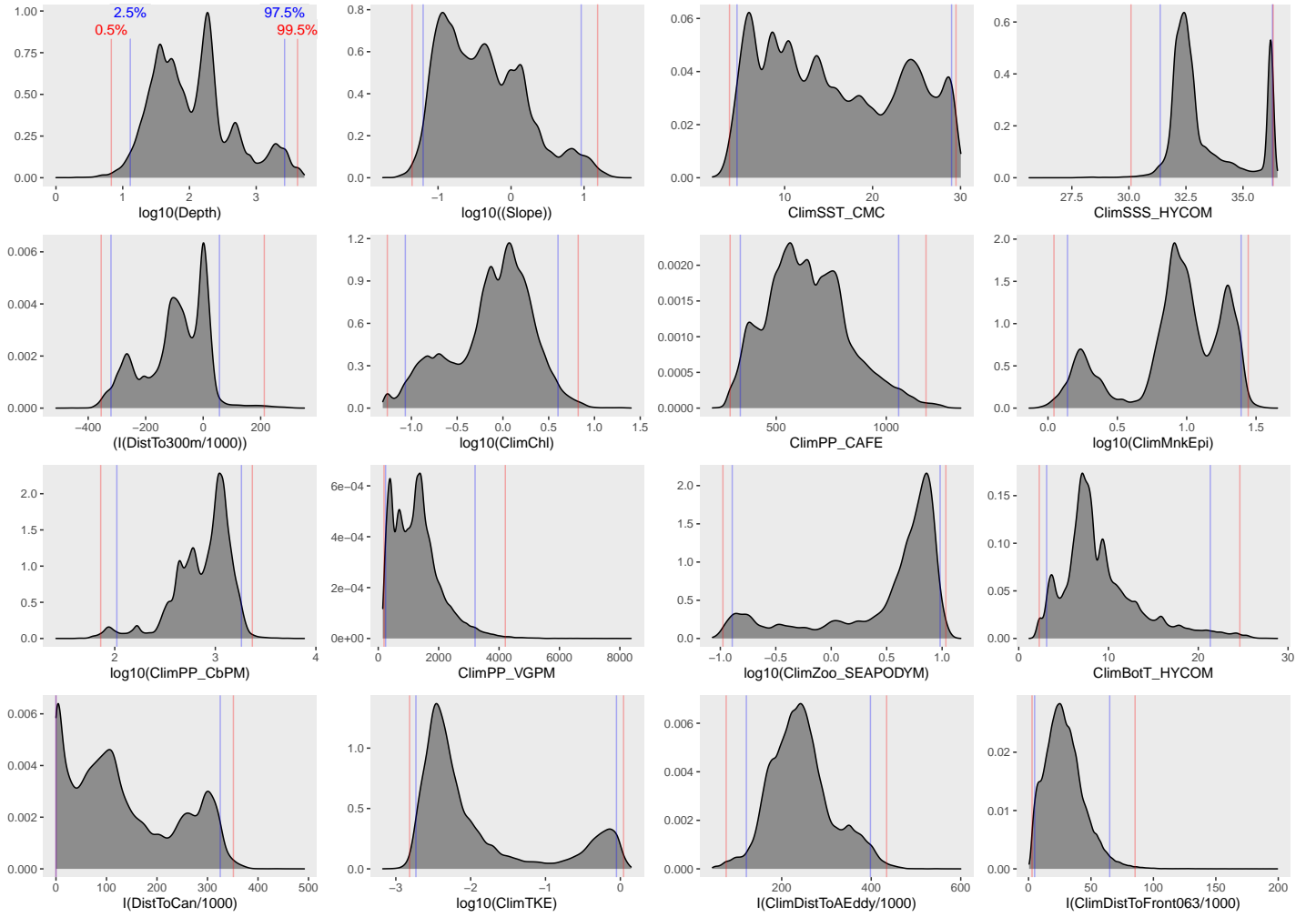


Figure 44: Density histograms shown in Figure 43 replotted without Winsorization, to show the full range of sampling represented by survey segments.

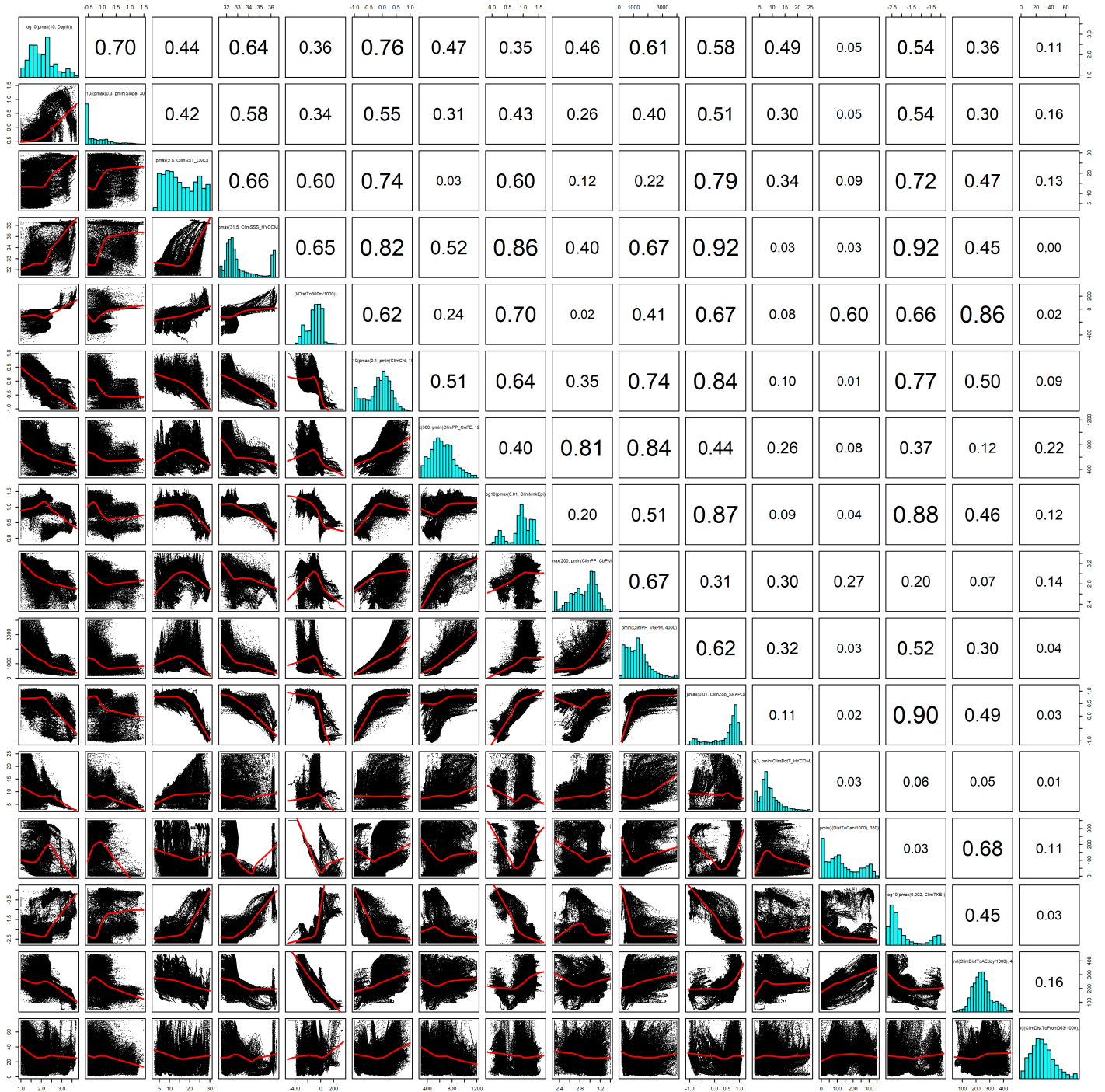


Figure 45: Scatterplot matrix of the covariates considered during the final model selection step. The final model may have included only a subset of the covariates shown here (see Figure 41), and additional covariates may have been considered in preceding selection steps. Covariates are transformed and Winsorized as shown in Figure 43. This plot is used to check simple correlations between covariates (via pairwise Pearson coefficients above the diagonal) and visually inspect for concurvity (via scatterplots and red lowess curves below the diagonal).

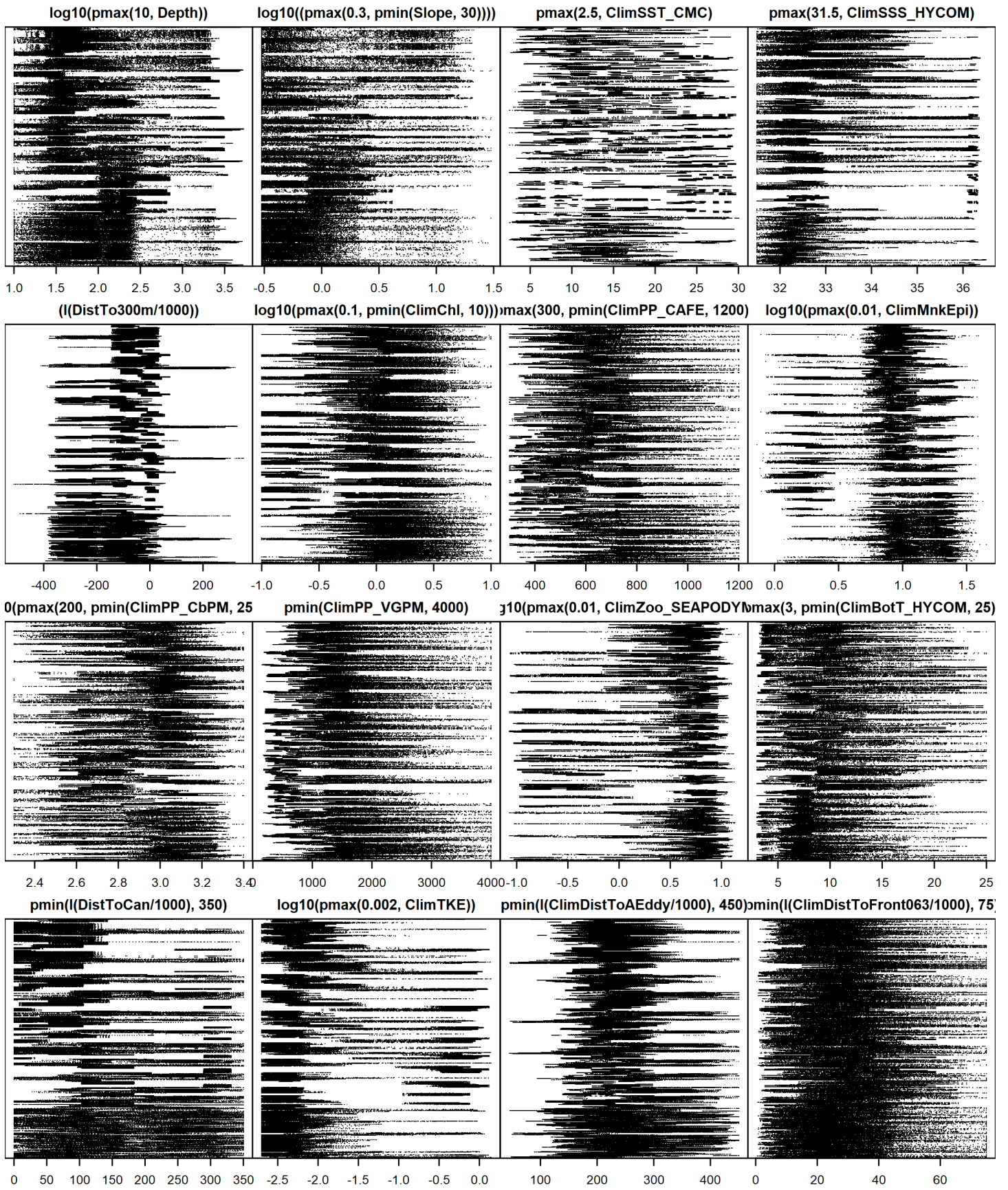


Figure 46: Dotplot of the covariates considered during the final model selection step. The final model may have included only a subset of the covariates shown here (see Figure 41), and additional covariates may have been considered in preceding selection steps. Covariates are transformed and Winsorized as shown in Figure 43. This plot is used to check for suspicious patterns and outliers in the data. Points are ordered vertically by segment ID, sequentially in time.

4.3 Extrapolation Diagnostics

4.3.1 Univariate Extrapolation

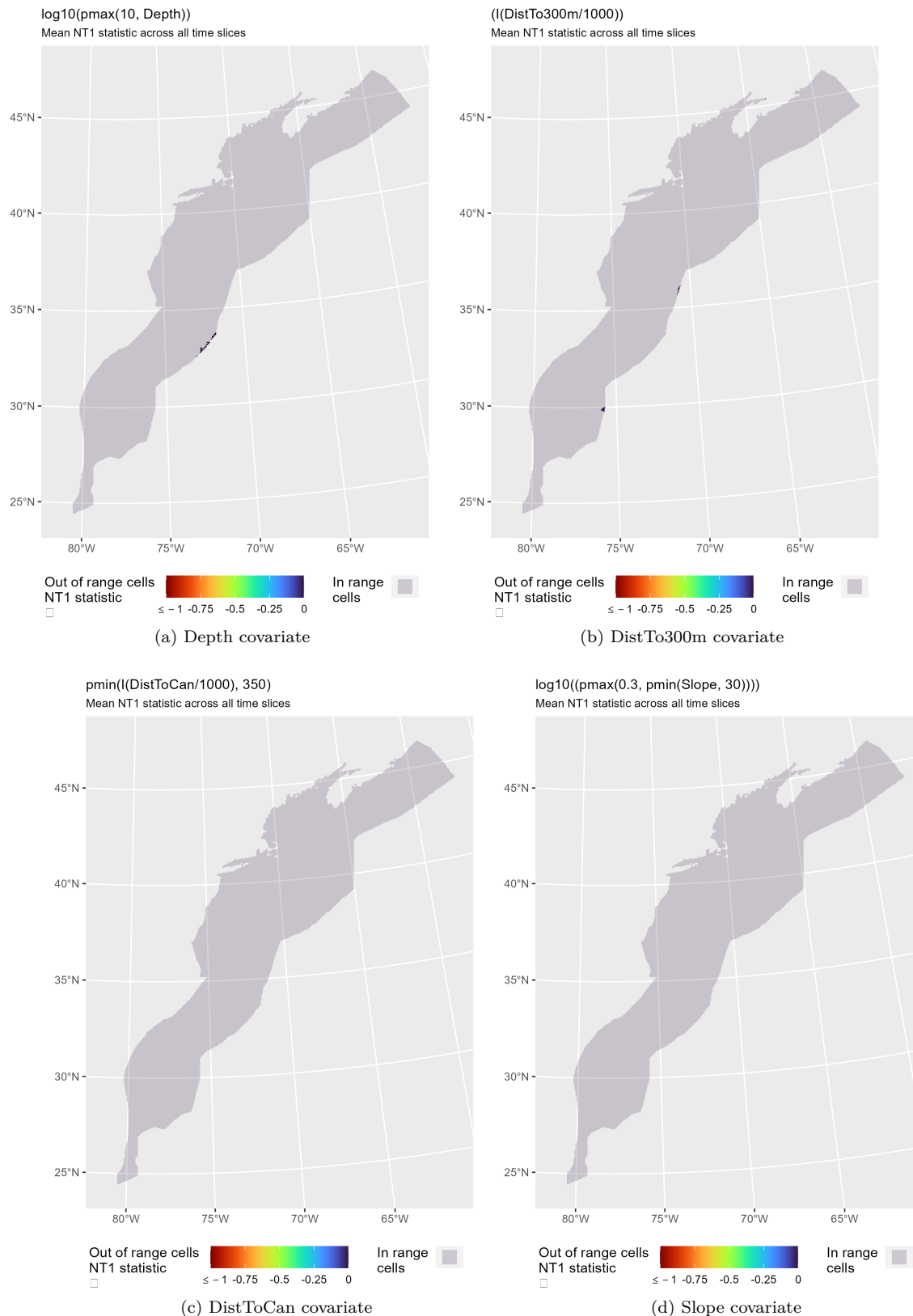


Figure 47: NT1 statistic (Mesgaran et al. (2014)) for static covariates used in the model for the region Surveyed Area (Excluding SE Shelf). Areas outside the sampled range of a covariate appear in color, indicating univariate extrapolation of that covariate occurred there. Areas within the sampled range appear in gray, indicating it did not occur.

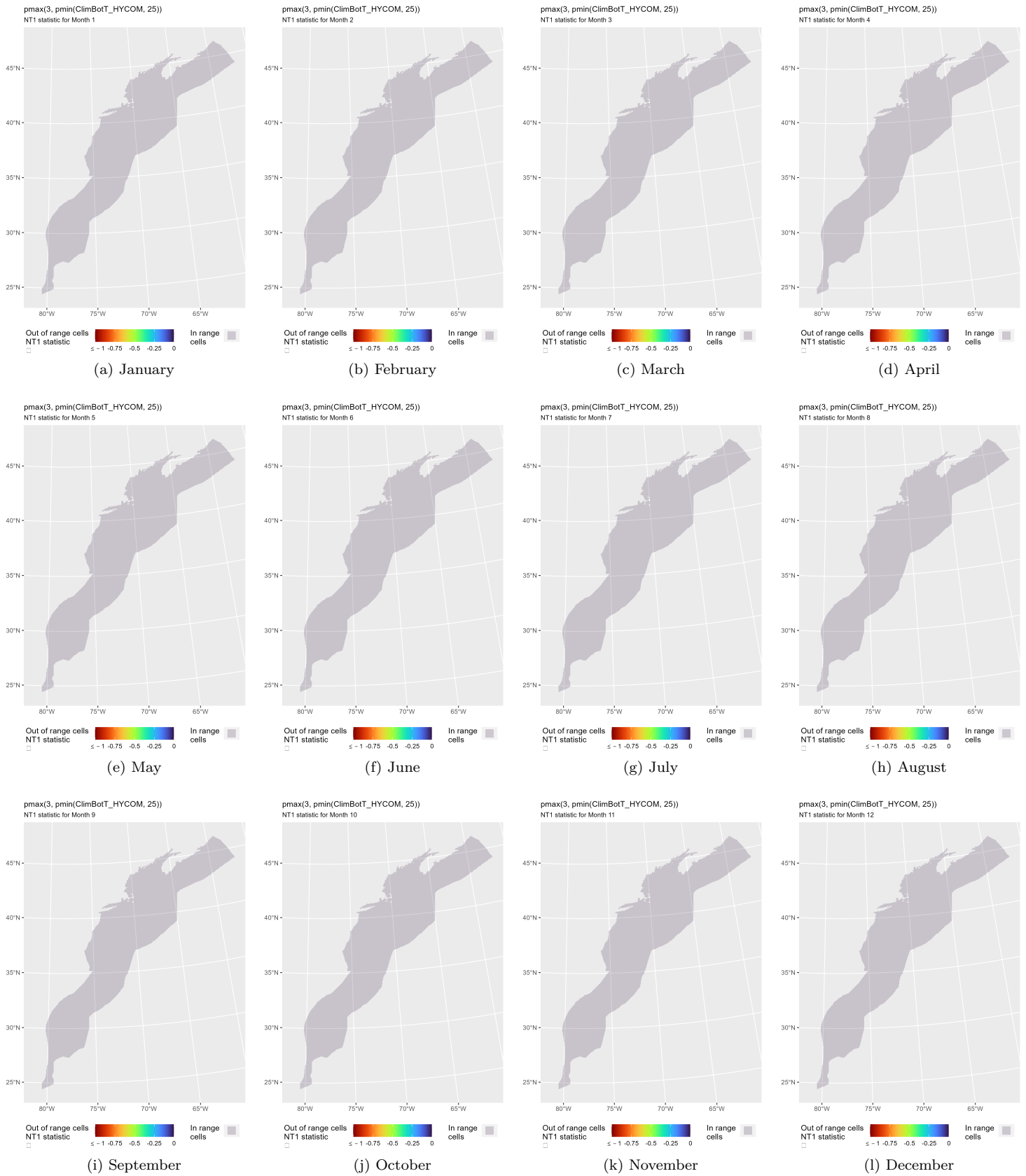


Figure 48: NT1 statistic (Mesgaran et al. (2014)) for the ClimBotT_HYCOM covariate in the model for the region Surveyed Area (Excluding SE Shelf). Areas outside the sampled range of a covariate appear in color, indicating univariate extrapolation of that covariate occurred there during the month. Areas within the sampled range appear in gray, indicating it did not occur.

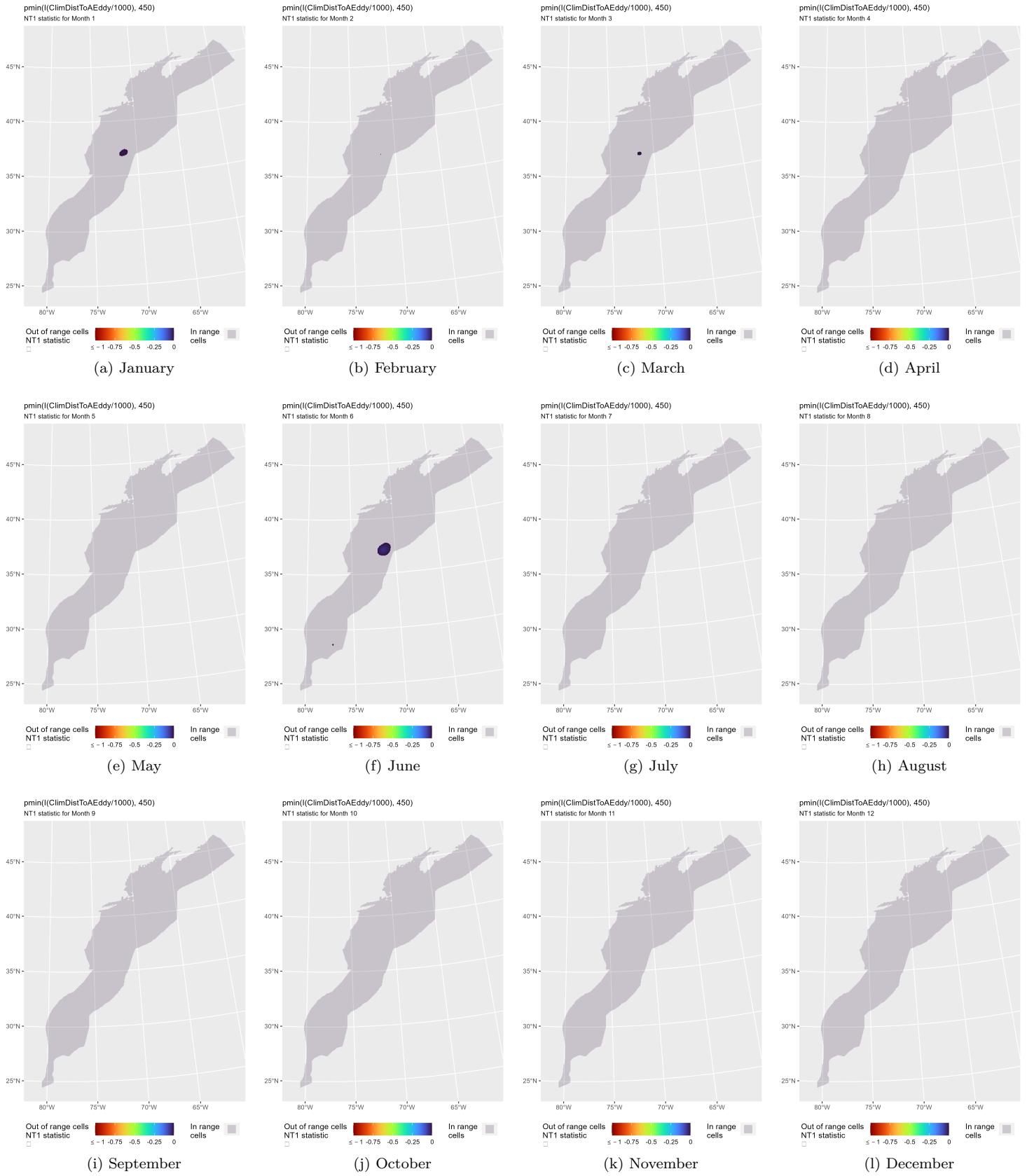


Figure 49: NT1 statistic (Mesgaran et al. (2014)) for the ClimDistToAEddy covariate in the model for the region Surveyed Area (Excluding SE Shelf). Areas outside the sampled range of a covariate appear in color, indicating univariate extrapolation of that covariate occurred there during the month. Areas within the sampled range appear in gray, indicating it did not occur.

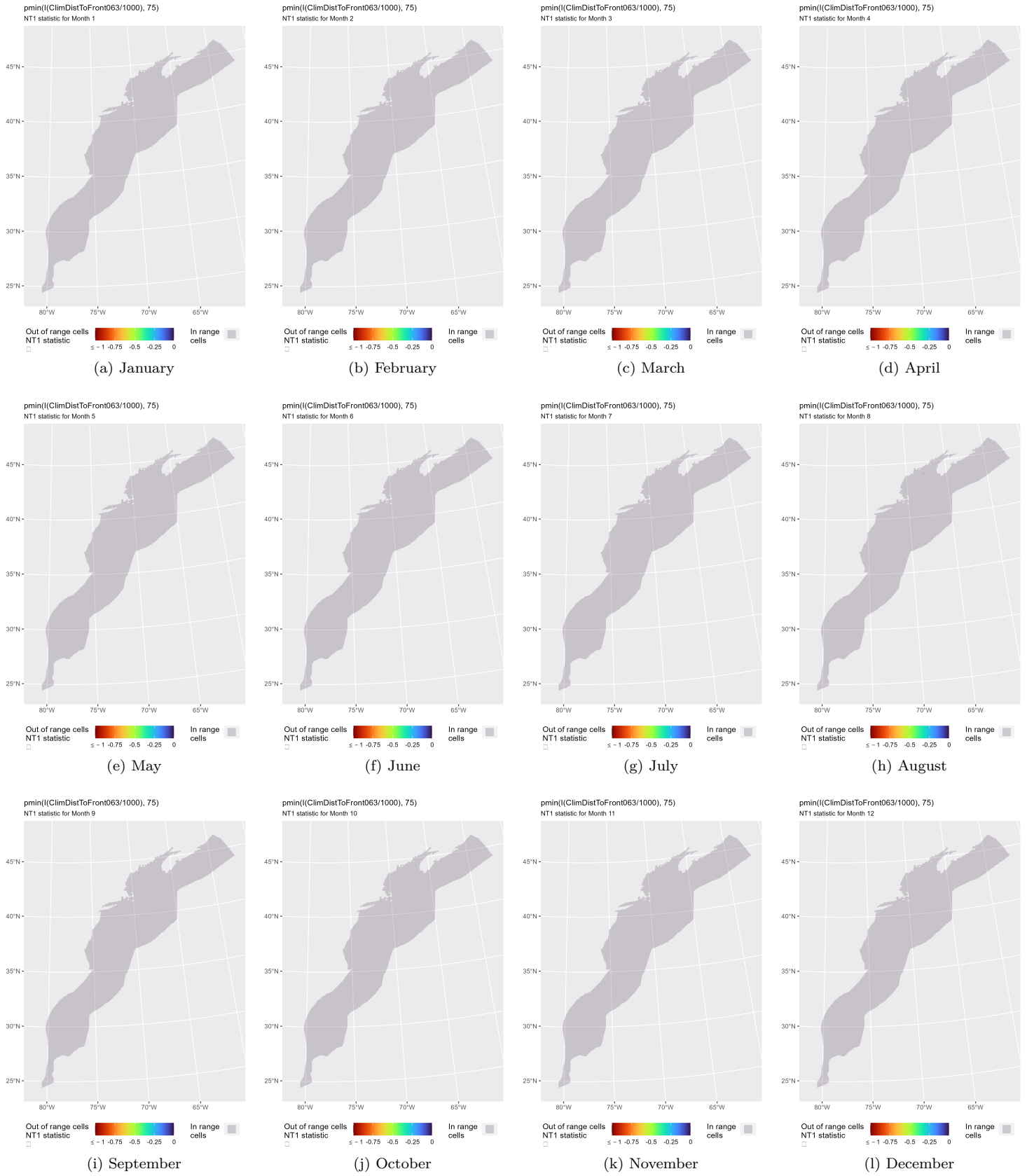


Figure 50: NT1 statistic (Mesgaran et al. (2014)) for the ClimDistToFront063 covariate in the model for the region Surveyed Area (Excluding SE Shelf). Areas outside the sampled range of a covariate appear in color, indicating univariate extrapolation of that covariate occurred there during the month. Areas within the sampled range appear in gray, indicating it did not occur.

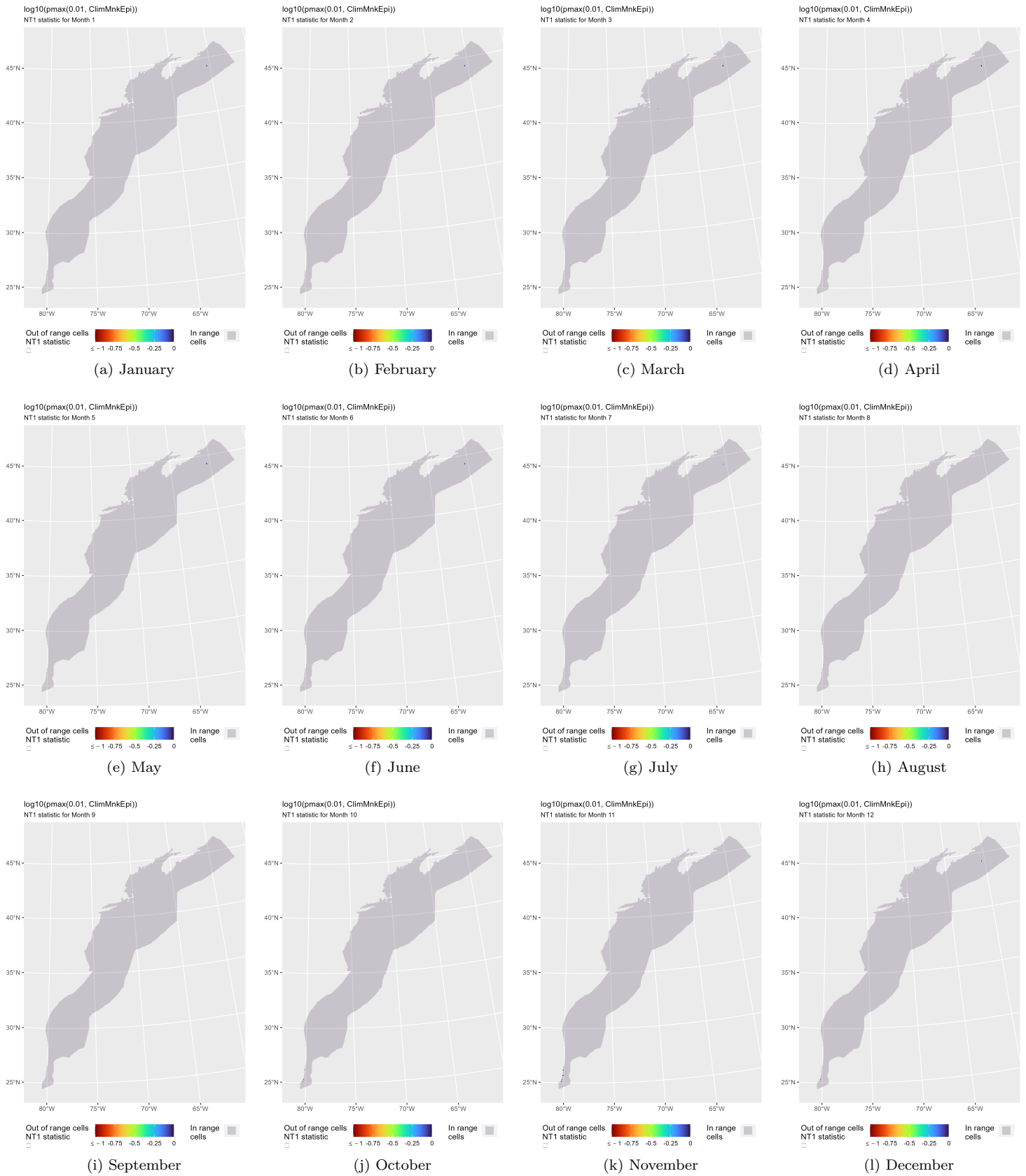


Figure 51: NT1 statistic (Mesgaran et al. (2014)) for the ClimMnkEpi covariate in the model for the region Surveyed Area (Excluding SE Shelf). Areas outside the sampled range of a covariate appear in color, indicating univariate extrapolation of that covariate occurred there during the month. Areas within the sampled range appear in gray, indicating it did not occur.

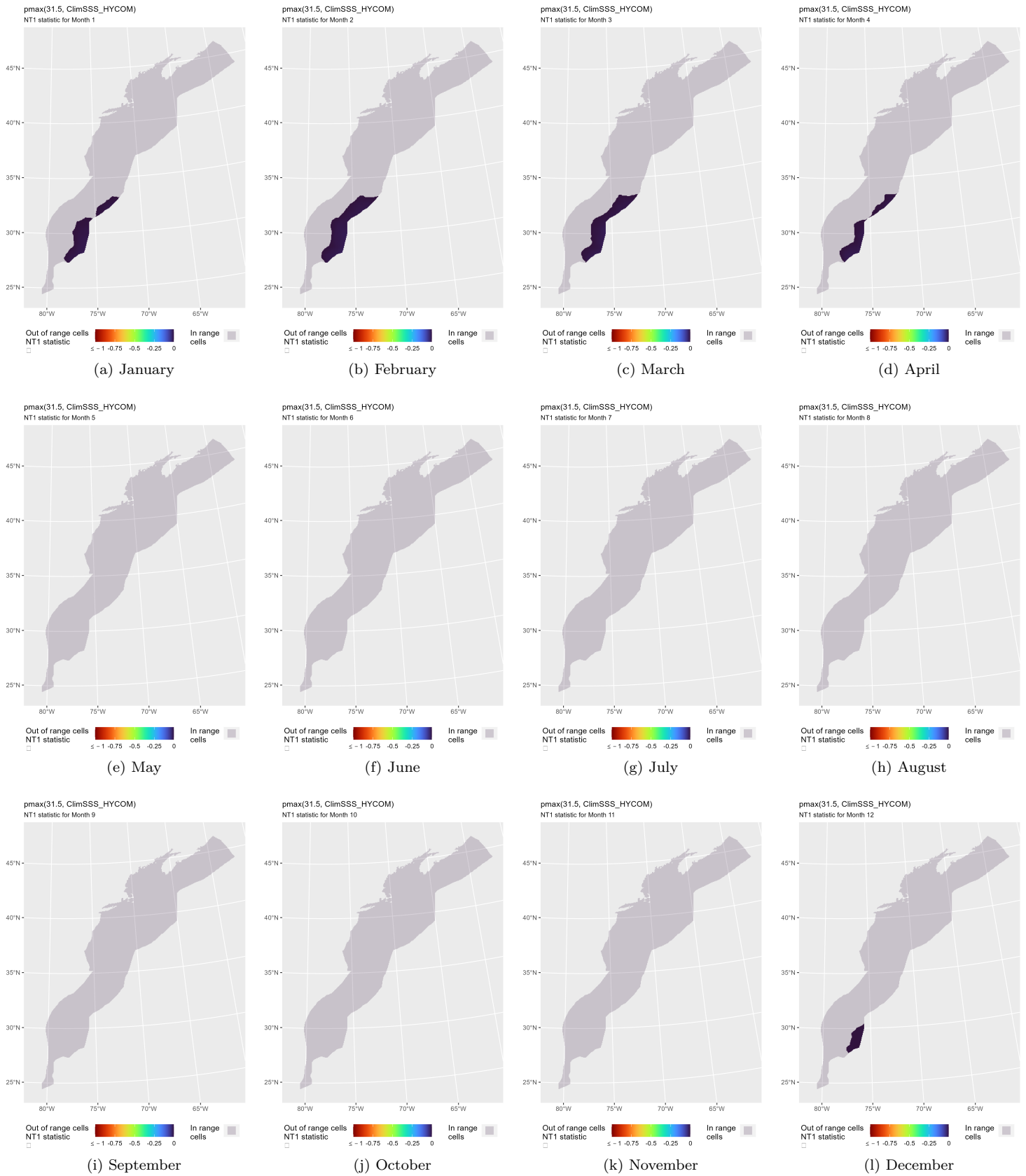


Figure 52: NT1 statistic (Mesgaran et al. (2014)) for the ClimSSS_HYCOM covariate in the model for the region Surveyed Area (Excluding SE Shelf). Areas outside the sampled range of a covariate appear in color, indicating univariate extrapolation of that covariate occurred there during the month. Areas within the sampled range appear in gray, indicating it did not occur.

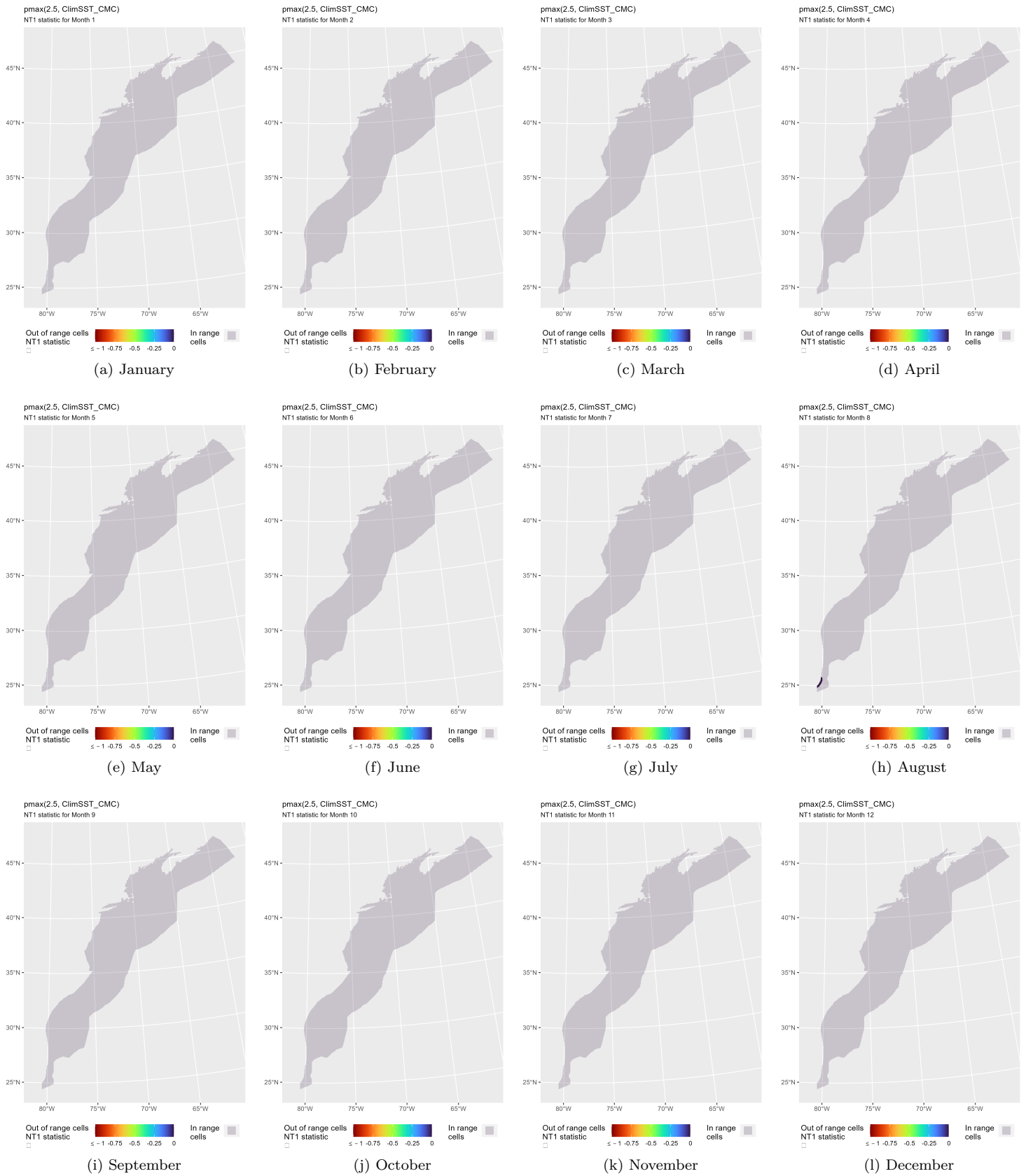


Figure 53: NT1 statistic (Mesgaran et al. (2014)) for the ClimSST_CMC covariate in the model for the region Surveyed Area (Excluding SE Shelf). Areas outside the sampled range of a covariate appear in color, indicating univariate extrapolation of that covariate occurred there during the month. Areas within the sampled range appear in gray, indicating it did not occur.

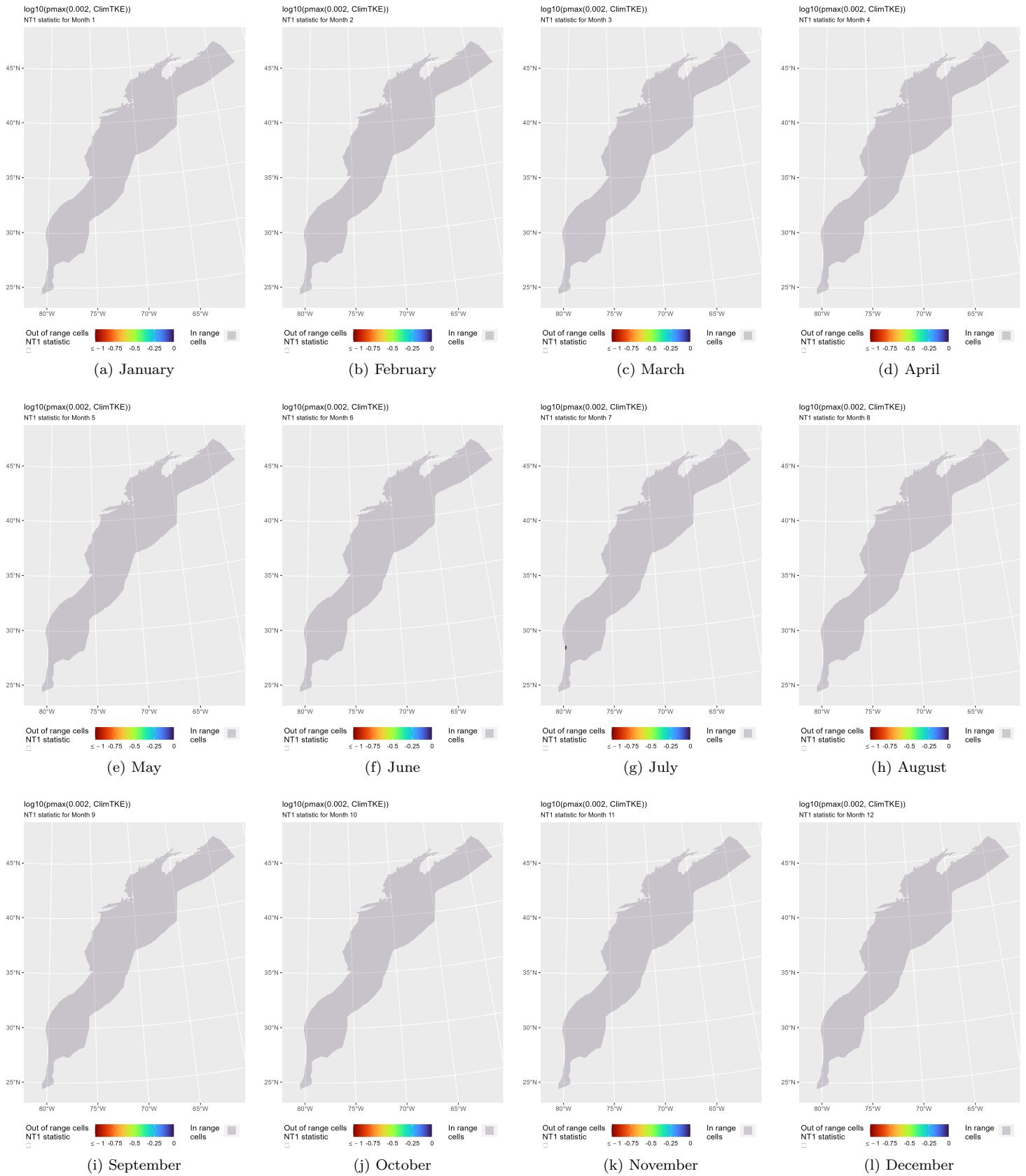


Figure 54: NT1 statistic (Mesgaran et al. (2014)) for the ClimTKE covariate in the model for the region Surveyed Area (Excluding SE Shelf). Areas outside the sampled range of a covariate appear in color, indicating univariate extrapolation of that covariate occurred there during the month. Areas within the sampled range appear in gray, indicating it did not occur.

4.3.2 Multivariate Extrapolation

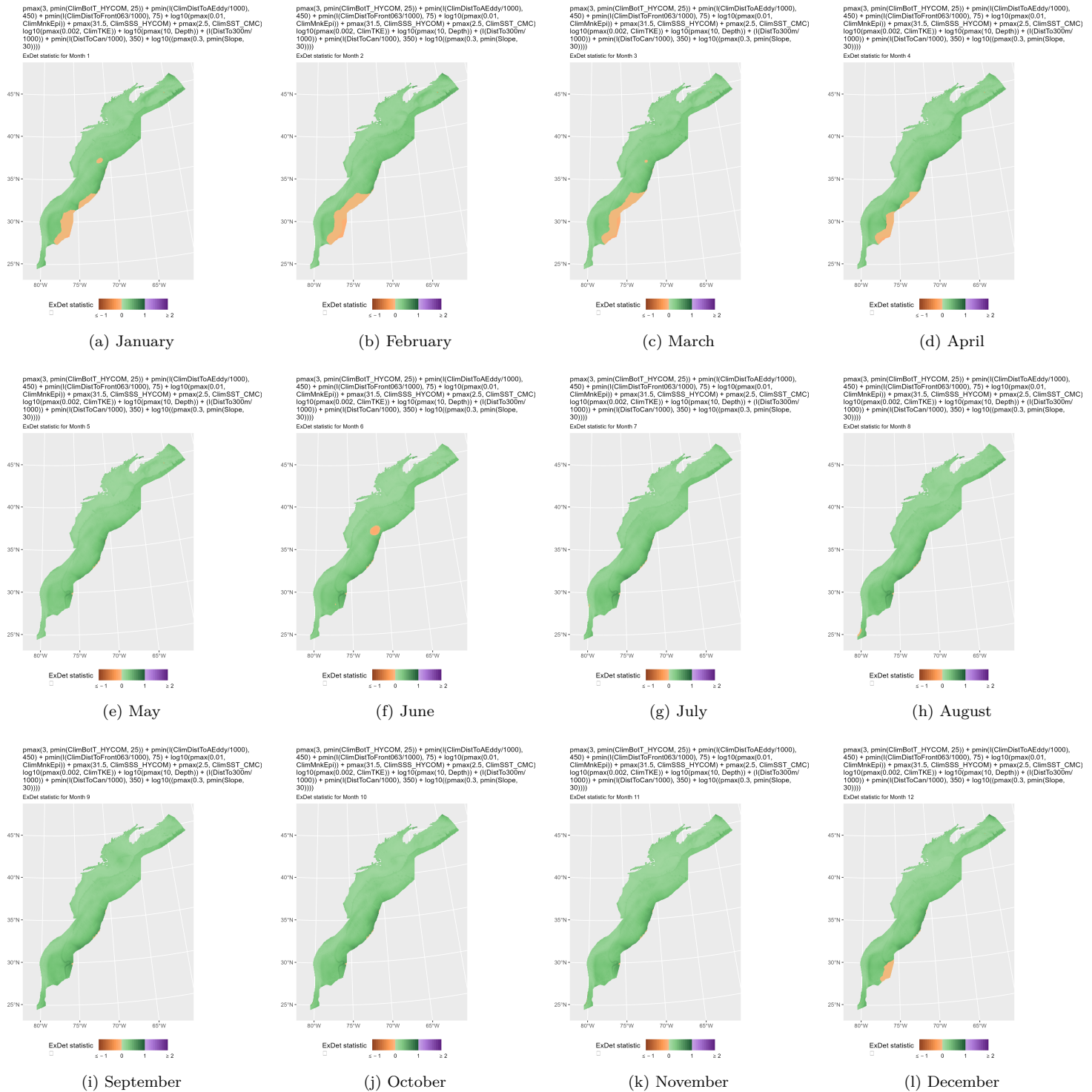


Figure 55: ExDet statistic (Mesgaran et al. (2014)) for all of the covariates used in the model for the region Surveyed Area (Excluding SE Shelf). Areas in orange ($\text{ExDet} < 0$) required univariate extrapolation of one or more covariates (see previous section). Areas in purple ($\text{ExDet} > 1$), did not require univariate extrapolation but did require multivariate extrapolation, by virtue of having novel combinations of covariates not represented in the survey data, according to the NT2 statistic (Mesgaran et al. (2014)). Areas in green ($0 \geq \text{ExDet} \leq 1$) did not require either type of extrapolation.

5 Predictions

Based on our evaluation of this model in the context of what is known of this species (see Section 4), we summarized its predictions into monthly climatological density and uncertainty surfaces, shown in the maps below.

5.1 Summarized Predictions

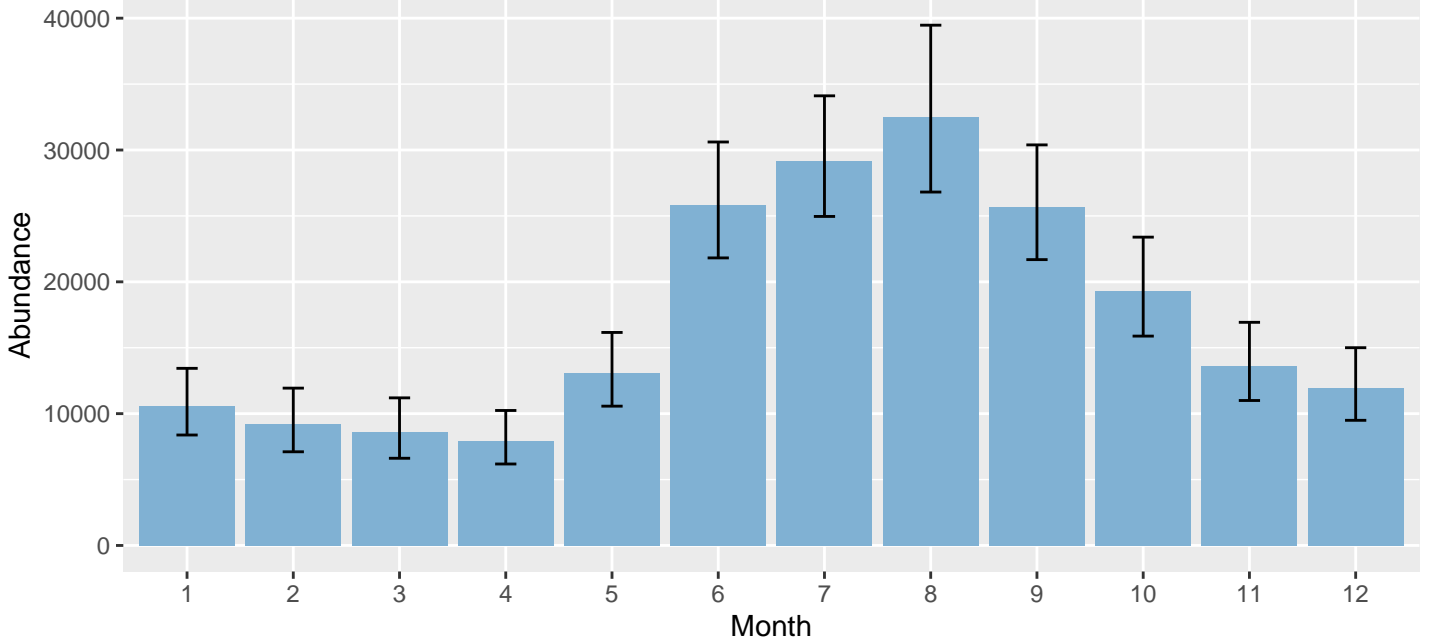


Figure 56: Mean monthly abundance for the prediction area for 1998-2019. Error bars are a 95% interval, made with a log-normal approximation using the prediction’s CV. The CV was estimated with the analytic approach given by Miller et al. (2022), Appendix S1, and accounts both for uncertainty in model parameter estimates and for temporal variability in dynamic covariates.

Table 12: Mean monthly abundance and density for the prediction area for 1998-2019. CV and intervals estimated as described for the previous figure.

Month	Abundance	CV	95% Interval	Area (km ²)	Density (individuals / 100 km ²)
1	10,611	0.121	8,380 - 13,437	1,273,075	0.83
2	9,211	0.133	7,108 - 11,936	1,273,075	0.72
3	8,607	0.135	6,617 - 11,197	1,273,075	0.68
4	7,956	0.129	6,181 - 10,240	1,273,075	0.62
5	13,068	0.109	10,568 - 16,159	1,273,075	1.03
6	25,839	0.087	21,814 - 30,607	1,273,075	2.03
7	29,179	0.080	24,960 - 34,110	1,273,075	2.29
8	32,529	0.099	26,810 - 39,467	1,273,075	2.56
9	25,670	0.086	21,685 - 30,387	1,273,075	2.02
10	19,274	0.099	15,882 - 23,391	1,273,075	1.51
11	13,646	0.110	10,999 - 16,930	1,273,075	1.07
12	11,935	0.117	9,495 - 15,003	1,273,075	0.94

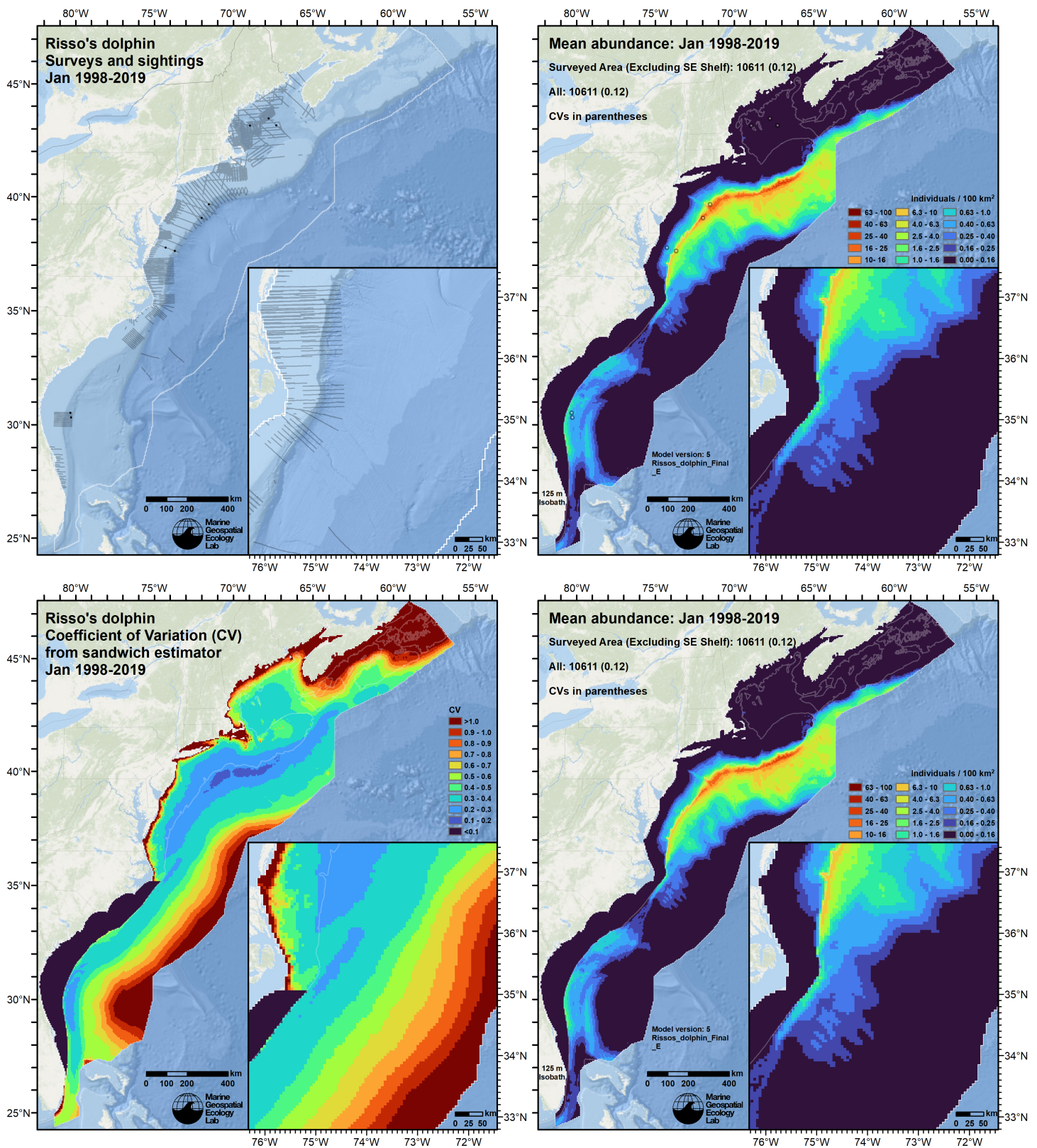


Figure 57: Survey effort and observations (top left), predicted density with observations (top right), predicted density without observations (bottom right), and coefficient of variation of predicted density (bottom left), for the month of January for the given era. Variance was estimated with the analytic approach given by Miller et al. (2022), Appendix S1, and accounts both for uncertainty in model parameter estimates and for temporal variability in dynamic covariates.

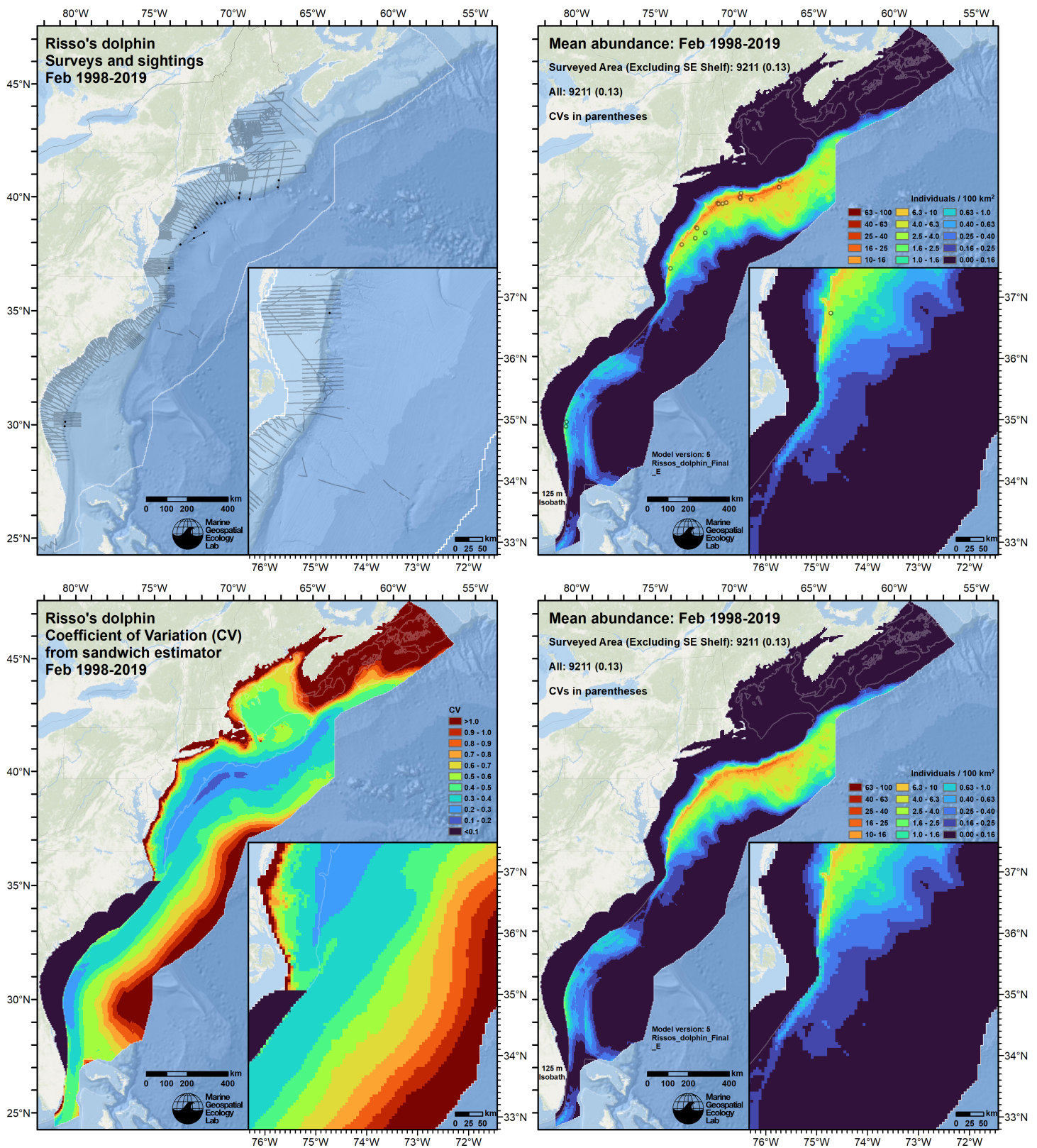


Figure 58: Survey effort and observations (top left), predicted density with observations (top right), predicted density without observations (bottom right), and coefficient of variation of predicted density (bottom left), for the month of February for the given era. Variance was estimated with the analytic approach given by Miller et al. (2022), Appendix S1, and accounts both for uncertainty in model parameter estimates and for temporal variability in dynamic covariates.

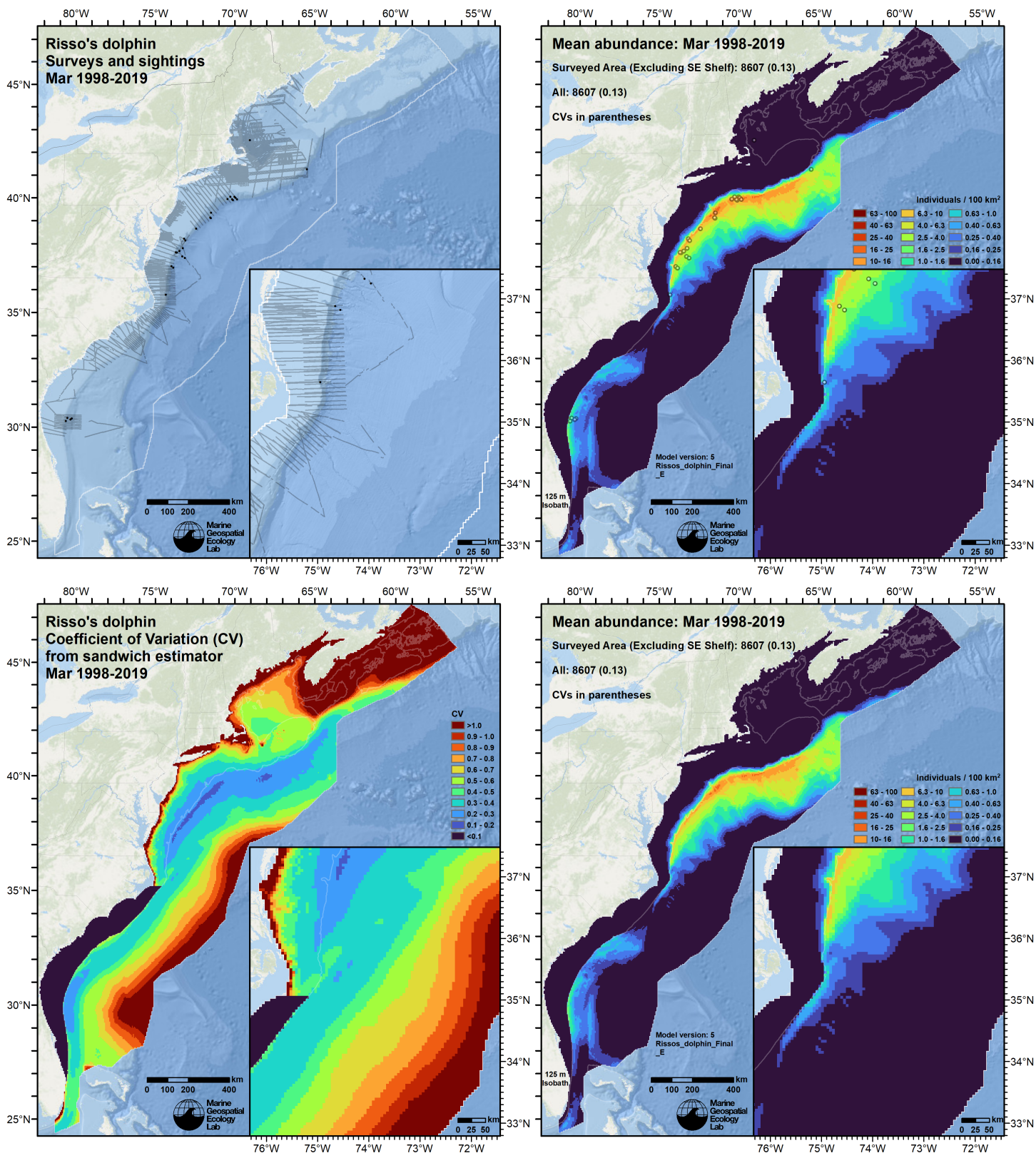


Figure 59: Survey effort and observations (top left), predicted density with observations (top right), predicted density without observations (bottom right), and coefficient of variation of predicted density (bottom left), for the month of March for the given era. Variance was estimated with the analytic approach given by Miller et al. (2022), Appendix S1, and accounts both for uncertainty in model parameter estimates and for temporal variability in dynamic covariates.

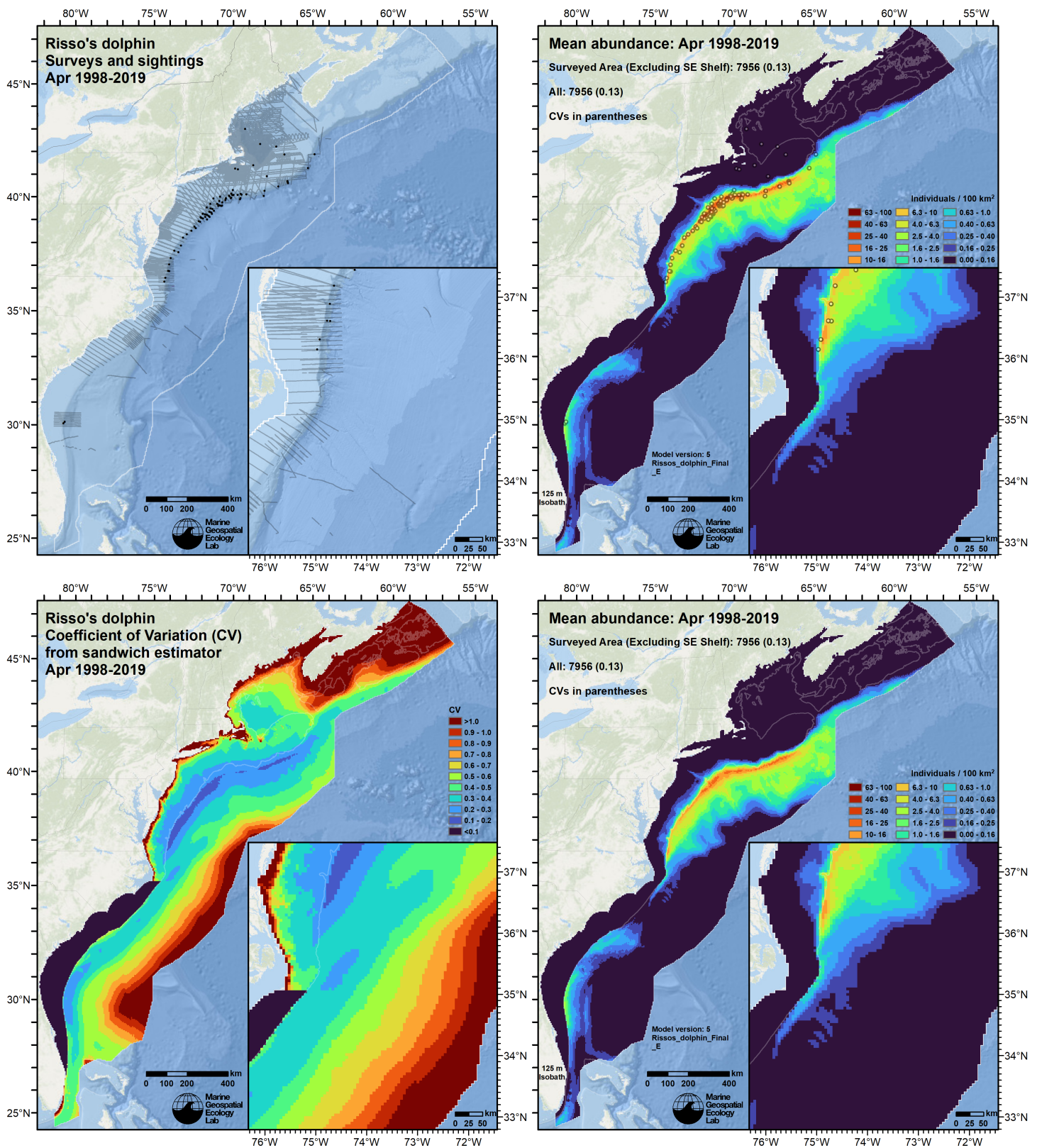


Figure 60: Survey effort and observations (top left), predicted density with observations (top right), predicted density without observations (bottom right), and coefficient of variation of predicted density (bottom left), for the month of April for the given era. Variance was estimated with the analytic approach given by Miller et al. (2022), Appendix S1, and accounts both for uncertainty in model parameter estimates and for temporal variability in dynamic covariates.

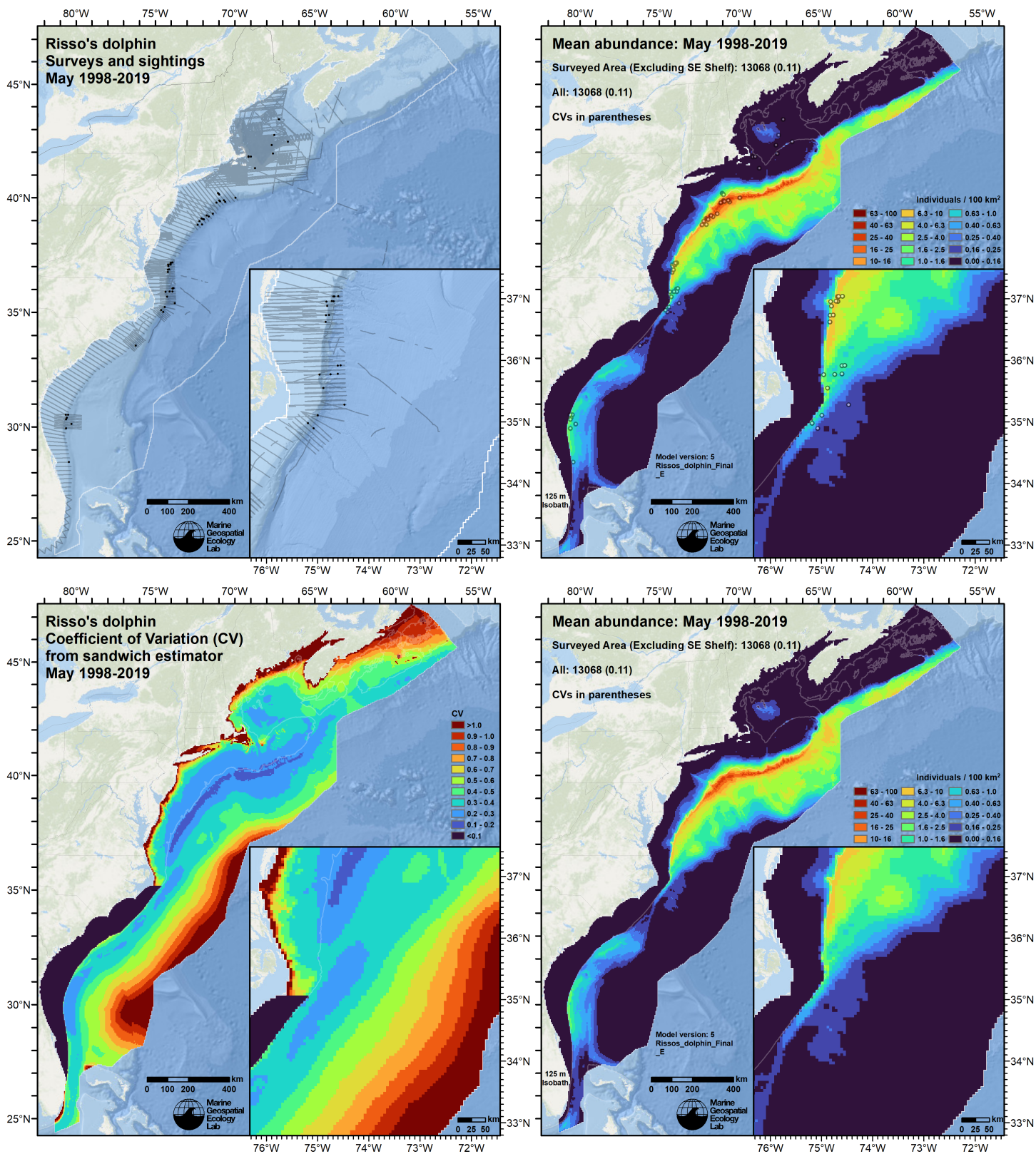


Figure 61: Survey effort and observations (top left), predicted density with observations (top right), predicted density without observations (bottom right), and coefficient of variation of predicted density (bottom left), for the month of May for the given era. Variance was estimated with the analytic approach given by Miller et al. (2022), Appendix S1, and accounts both for uncertainty in model parameter estimates and for temporal variability in dynamic covariates.

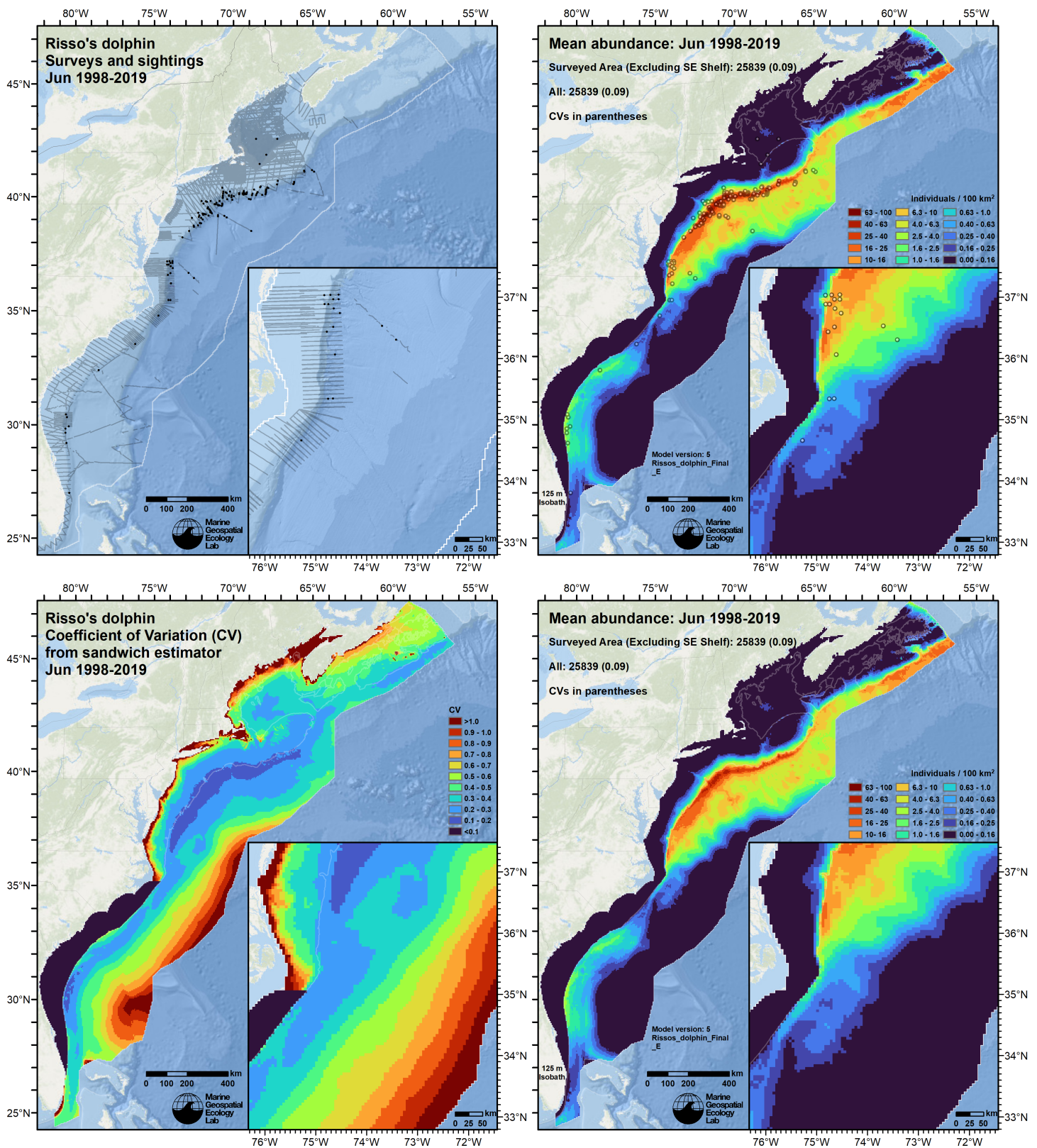


Figure 62: Survey effort and observations (top left), predicted density with observations (top right), predicted density without observations (bottom right), and coefficient of variation of predicted density (bottom left), for the month of June for the given era. Variance was estimated with the analytic approach given by Miller et al. (2022), Appendix S1, and accounts both for uncertainty in model parameter estimates and for temporal variability in dynamic covariates.

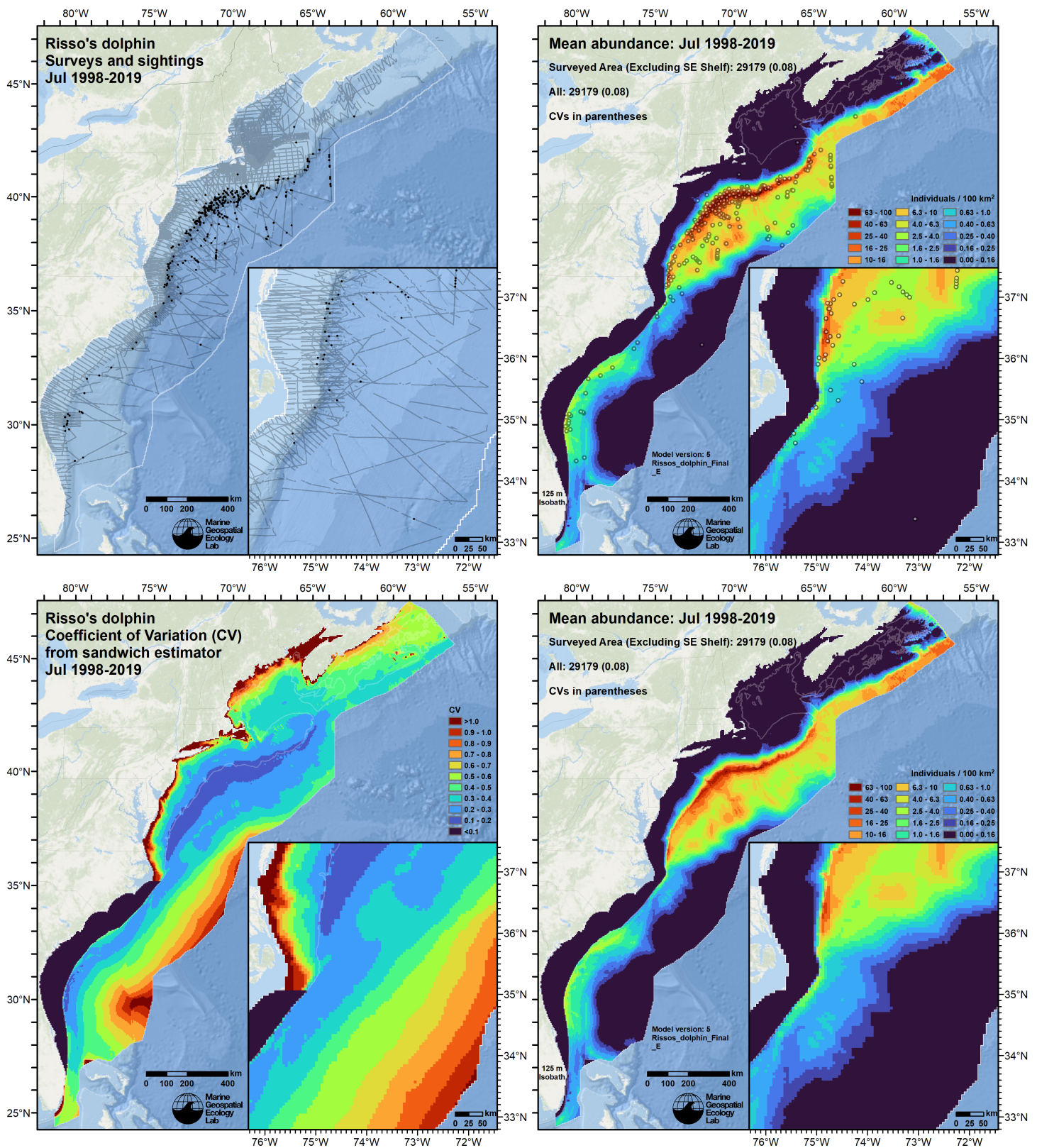


Figure 63: Survey effort and observations (top left), predicted density with observations (top right), predicted density without observations (bottom right), and coefficient of variation of predicted density (bottom left), for the month of July for the given era. Variance was estimated with the analytic approach given by Miller et al. (2022), Appendix S1, and accounts both for uncertainty in model parameter estimates and for temporal variability in dynamic covariates.

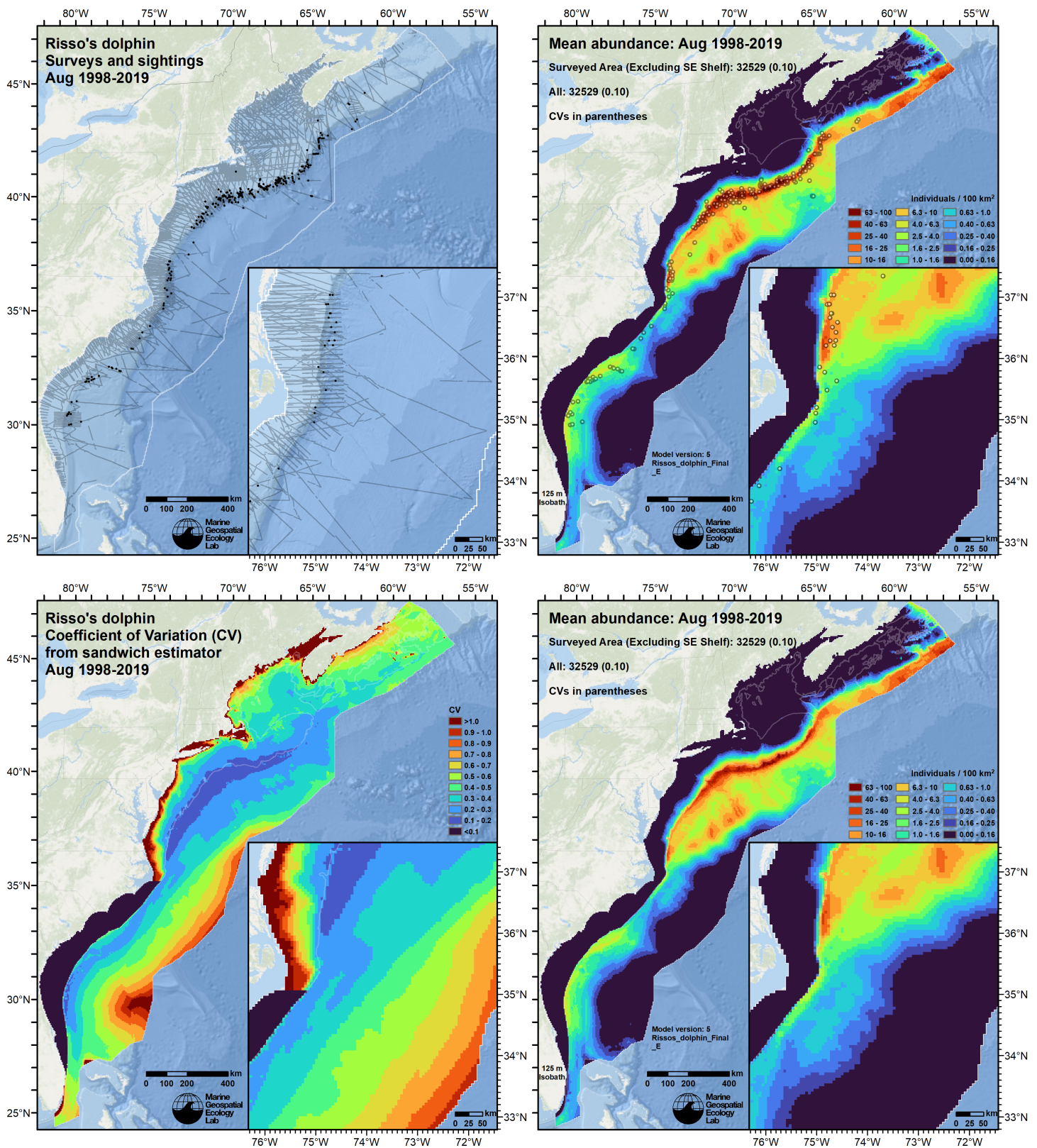


Figure 64: Survey effort and observations (top left), predicted density with observations (top right), predicted density without observations (bottom right), and coefficient of variation of predicted density (bottom left), for the month of August for the given era. Variance was estimated with the analytic approach given by Miller et al. (2022), Appendix S1, and accounts both for uncertainty in model parameter estimates and for temporal variability in dynamic covariates.

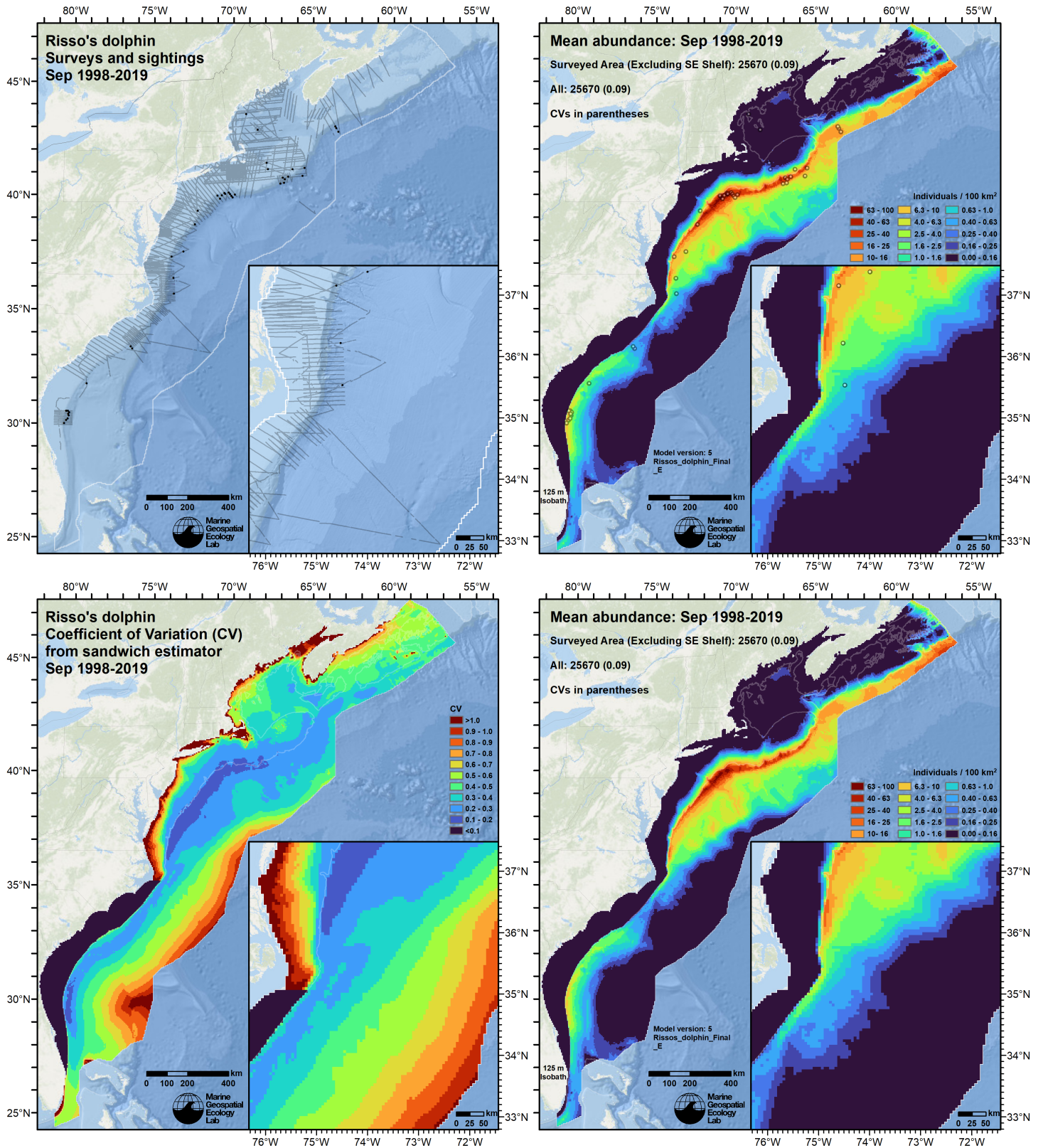


Figure 65: Survey effort and observations (top left), predicted density with observations (top right), predicted density without observations (bottom right), and coefficient of variation of predicted density (bottom left), for the month of September for the given era. Variance was estimated with the analytic approach given by Miller et al. (2022), Appendix S1, and accounts both for uncertainty in model parameter estimates and for temporal variability in dynamic covariates.

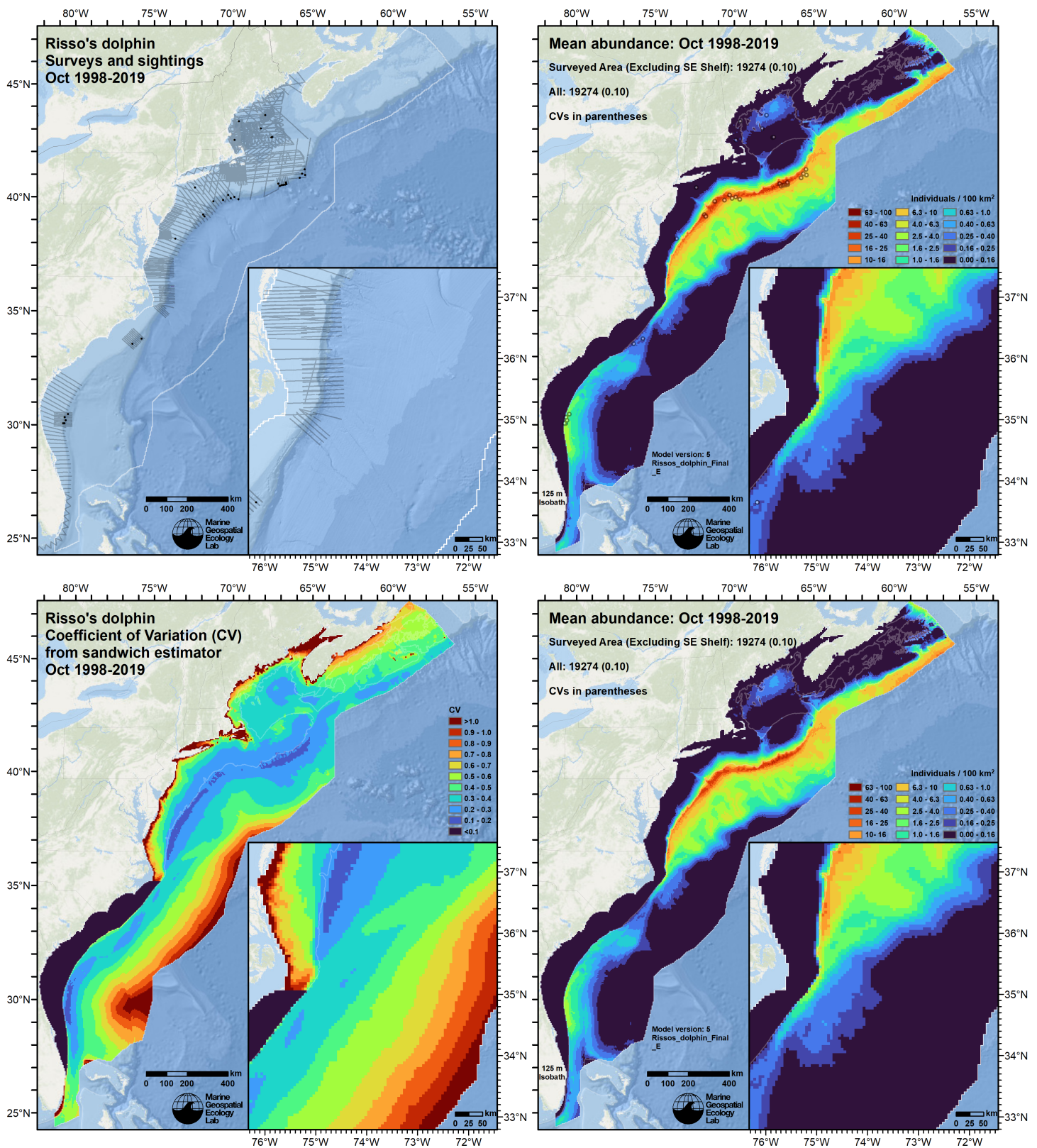


Figure 66: Survey effort and observations (top left), predicted density with observations (top right), predicted density without observations (bottom right), and coefficient of variation of predicted density (bottom left), for the month of October for the given era. Variance was estimated with the analytic approach given by Miller et al. (2022), Appendix S1, and accounts both for uncertainty in model parameter estimates and for temporal variability in dynamic covariates.

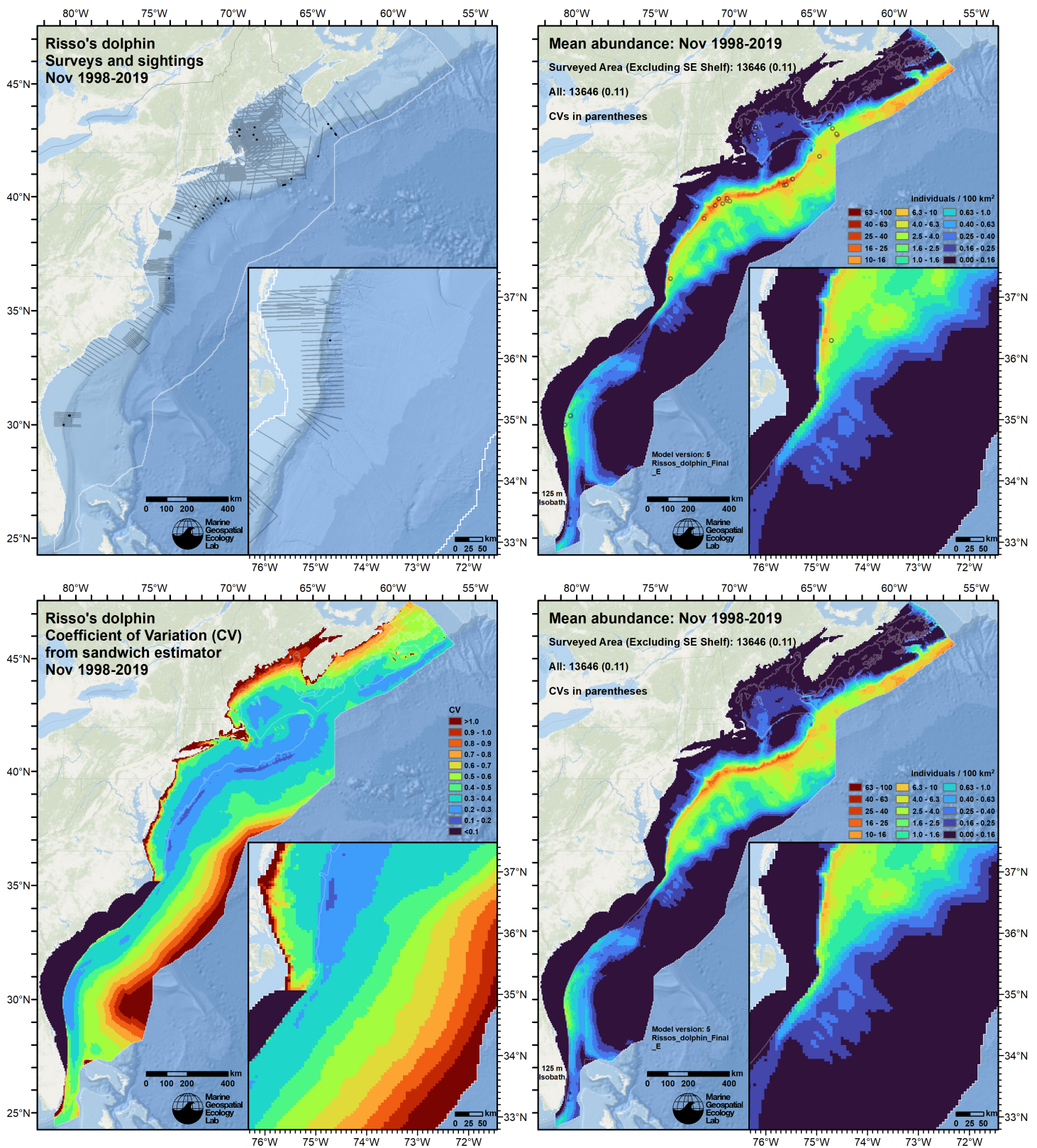


Figure 67: Survey effort and observations (top left), predicted density with observations (top right), predicted density without observations (bottom right), and coefficient of variation of predicted density (bottom left), for the month of November for the given era. Variance was estimated with the analytic approach given by Miller et al. (2022), Appendix S1, and accounts both for uncertainty in model parameter estimates and for temporal variability in dynamic covariates.

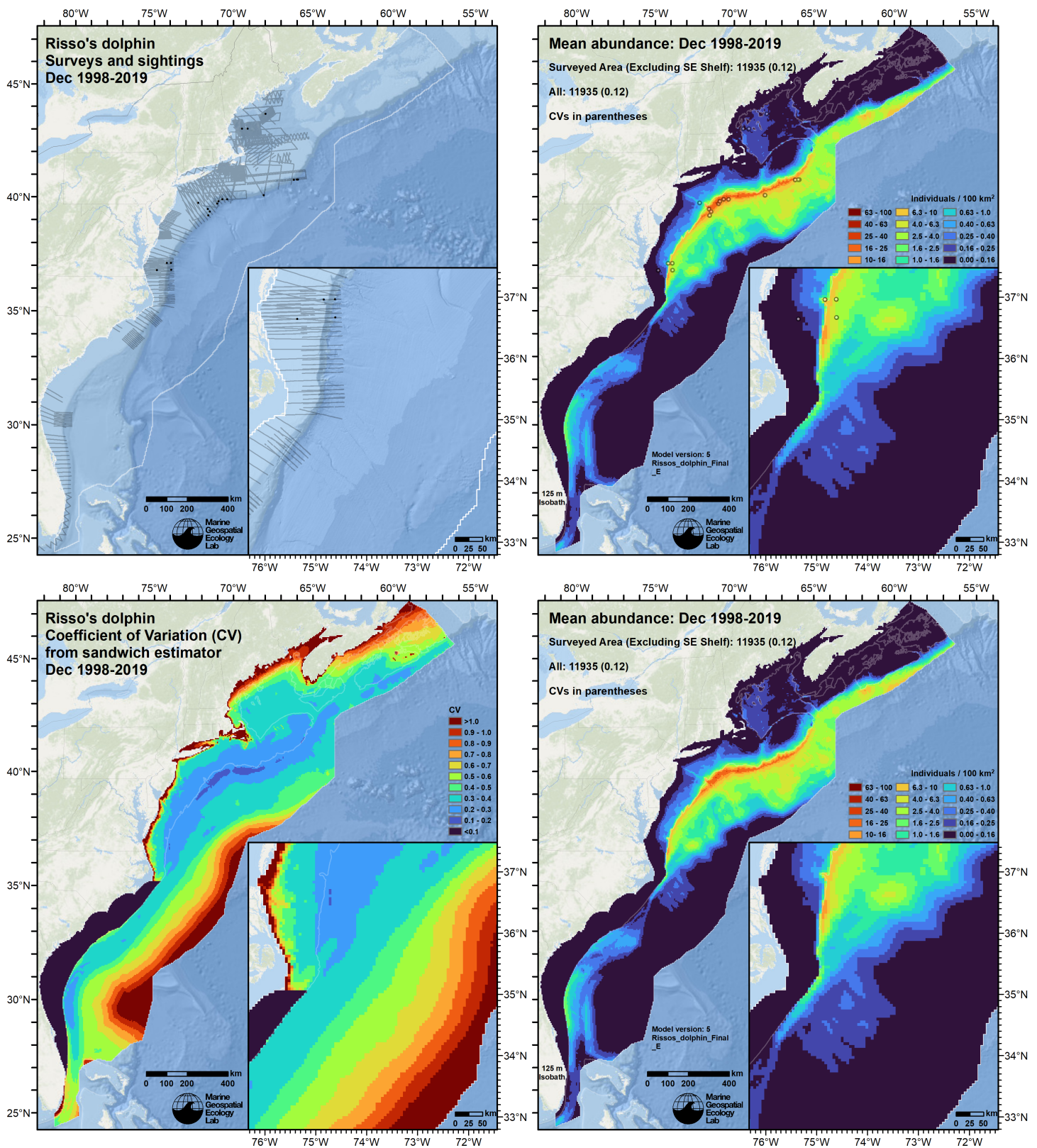


Figure 68: Survey effort and observations (top left), predicted density with observations (top right), predicted density without observations (bottom right), and coefficient of variation of predicted density (bottom left), for the month of December for the given era. Variance was estimated with the analytic approach given by Miller et al. (2022), Appendix S1, and accounts both for uncertainty in model parameter estimates and for temporal variability in dynamic covariates.

5.2 Abundance Comparisons

5.2.1 NOAA Stock Assessment Report

Table 13: Comparison of regional abundance estimates from the 2021 NOAA Stock Assessment Report (SAR) (Hayes et al. (2022)) to estimates from this density model extracted from roughly comparable zones (Figure 69 below). The SAR estimates were based on a single year of surveying, while the model estimates were taken from the multi-year mean density surfaces we provide to model users (Section 5.1).

2021 Stock Assessment Report			Density Model		
Month/Year	Area	N _{est}	Period	Zone	Abundance
Jun-Sep 2016	Central Virginia to lower Bay of Fundy ^a	22,175	Jun-Sep 1998-2019	NEFSC	18,529
Jun-Sep 2016	Florida to central Virginia ^b	7,245	Jun-Sep 1998-2019	SEFSC	3,869
Jun-Sep 2016	Bay of Fundy/Scotian Shelf ^c	6,073	Jun-Sep 1998-2019	Canada ^d	5,789
Jun-Sep 2016	Total	35,493	Jun-Sep 1998-2019	Total	28,187

^a Estimate originally from Palka (2020).

^b Estimate originally from Garrison (2020).

^c Estimate originally from Lawson and Gosselin (2018).

^d Our Canada zone is roughly comparable to the SAR's Bay of Fundy/Scotian Shelf area (excluding the Gulf of St. Lawrence).

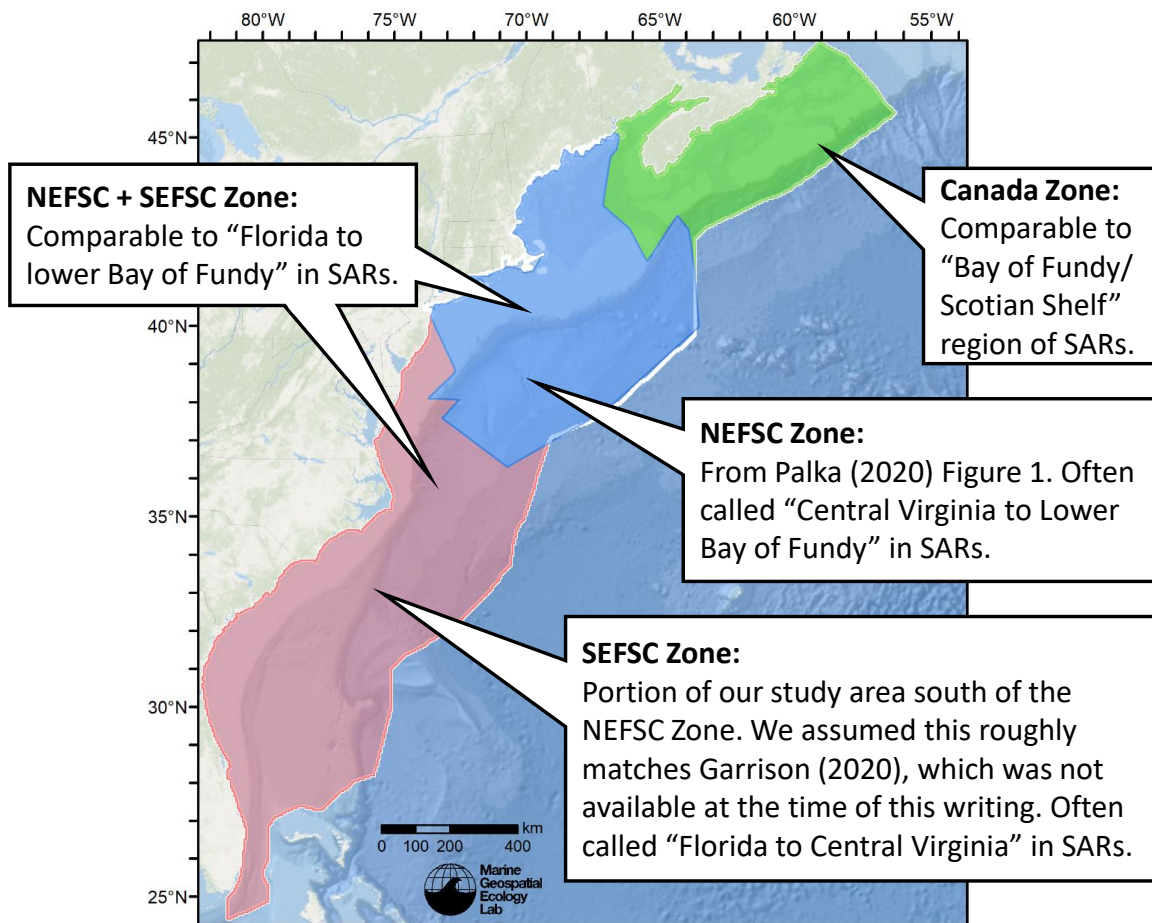


Figure 69: Zones for which we extracted abundance estimates from the density model for comparison to estimates from the NOAA Stock Assessment Report.

5.2.2 Previous Density Model

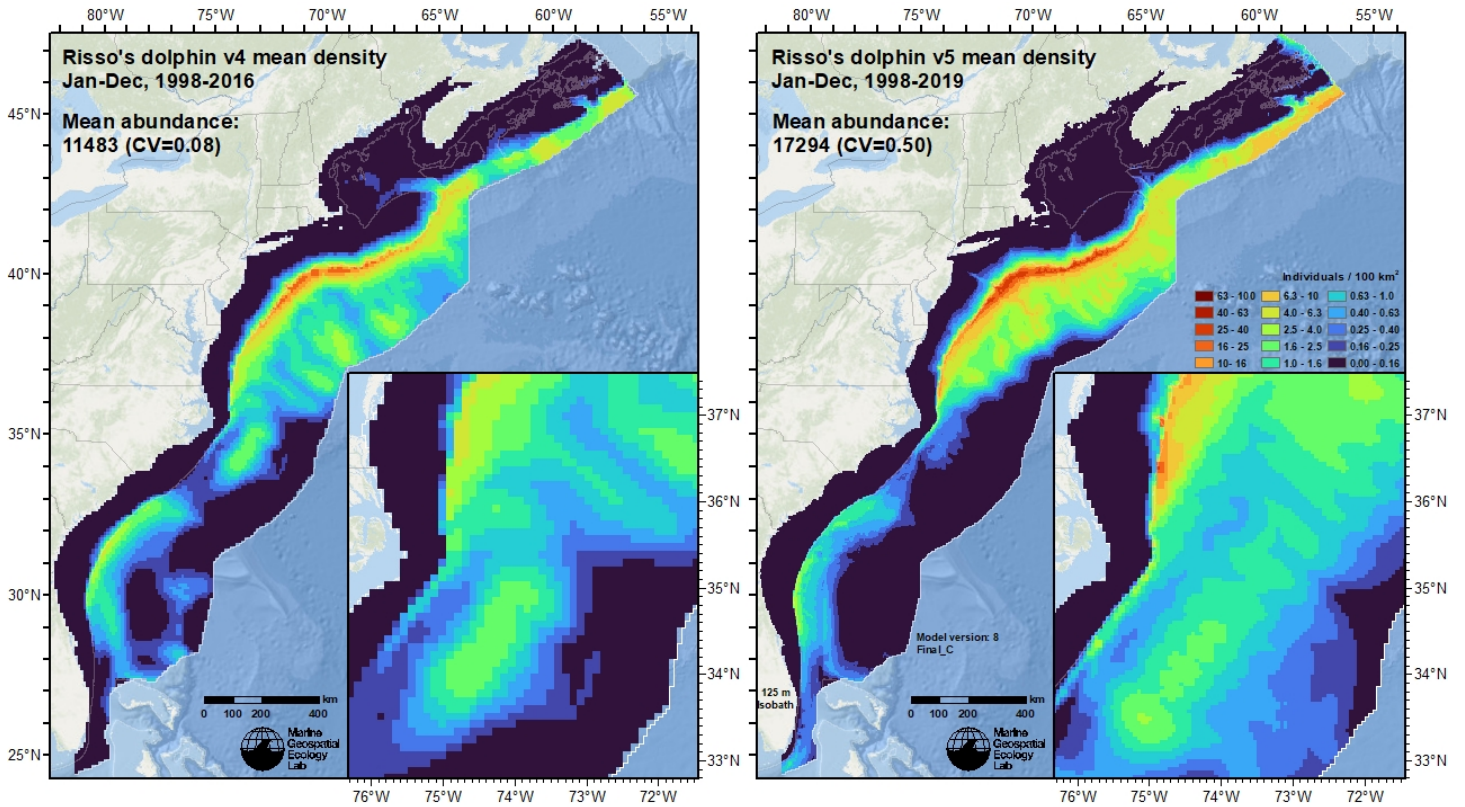


Figure 70: Comparison of the mean density predictions from the previous model (left) released by Roberts et al. (2017) to those from this model (right).

6 Discussion

The mean abundance predicted was 17,294 animals with highest abundance predicted at the slope and offshore of the slope in the north and along the slope between the shelf and Blake Plateau in the south. Monthly predicted abundance showed strong seasonal variation, with the lowest abundance of 7,956 animals predicted in April and the highest abundance of 32,529 animals predicted in August and waning throughout fall and spring, corresponding largely to seasonal variation reported by Hayes et al. (2022) and Cohen et al. (2022). In the northern portion of the study area abundance clearly increases beginning in May and extending to the northernmost edge of the study area in June through October, then decreases in winter months. In the Gulf of Maine, Risso's dolphins are predicted in May and June and then from September through January at varying abundance, suggesting seasonal preferences in use of the area. In the southern portions of the study area, Risso's dolphins are predicted year-round with the highest abundances predicted in summer months, again corresponding to patterns reported by Cohen et al. (2022).

The extrapolation statistics show some extrapolation in univariate space. Depth and distance to 1500 m isobath show a few out of range cells at the outer easternmost edge of the mid-Atlantic Bight (Figure 47). The HYCOM sea surface salinity covariate showed a fairly large block of extrapolation at the southeastern edge of the study area in winter and spring where no surveys covered the high salinity conditions at that time of year (Figure 52). Finally, the distance to anticyclonic eddy covariate showed some univariate extrapolation in January, March and June (Figure 49). In this case distances “inside” the eddy ring are negative values, and the extrapolation cells indicate very large eddies, with large cores that are far from the ring in the negative direction. This is unlikely to be a major issue, but the functional relationship to the anticyclonic eddy covariate showed a rising relationship as distance to the eddy gets smaller (Figure 41). Even larger values will result with this extrapolation in these “big” eddies. Because the slope of the rising relationship was relatively flat, the resulting contribution to density remained controlled, and the large eddies needed to trigger the extrapolation were infrequent and as such, unlikely to have yielded a big effect in the final model.

In comparison to the SAR estimate (22,175) the Risso's dolphin abundance predicted for the NEFSC region by this model (18,529) was similar, with our estimate being 16% (3,646 animals) lower than the SAR. For the SEFSC region, the SAR estimate (7,254) was 47% (1,465 animals) higher than the abundance predicted by this model (3,869). For the Canada

region, the SAR estimate (6,073) was within 5% (284 animals) of this model's estimate (5,789). The total SAR estimate for all regions (35,493) predicted 7,306 (21%) more animals than this model (28,187). Differences may be because the SAR estimates are based on a single year of summer survey data, whereas our estimates, although extracted for the same months, are influenced by additional surveys, seasons, and years.

In comparison to the Roberts et al. (2017) model, mean predicted abundance was 34% (6,441 animals) higher in the new model. The general pattern of prediction was similar; however, this model predicted lower abundance in the mid-Atlantic and southern offshore regions.

It should be noted that Risso's dolphin clicks can be classified to species. As such, it may be possible to include acoustic surveys in Risso's dolphin models in the future.

References

- Barco SG, Burt L, DePerte A, Digiovanni R Jr. (2015) Marine Mammal and Sea Turtle Sightings in the Vicinity of the Maryland Wind Energy Area July 2013-June 2015, VAQF Scientific Report #2015-06. Virginia Aquarium & Marine Science Center Foundation, Virginia Beach, VA
- Barlow J, Rankin S (2007) False killer whale abundance and density: Preliminary estimates for the PICEAS study area south of Hawaii and new estimates for the US EEZ around Hawaii.
- Becker JJ, Sandwell DT, Smith WHF, Braud J, Binder B, Depner J, Fabre D, Factor J, Ingalls S, Kim S-H, Ladner R, Marks K, Nelson S, Pharaoh A, Trimmer R, Von Rosenberg J, Wallace G, Weatherall P (2009) Global Bathymetry and Elevation Data at 30 Arc Seconds Resolution: SRTM30_PLUS. *Marine Geodesy* 32:355–371. doi: [10.1080/01490410903297766](https://doi.org/10.1080/01490410903297766)
- Benoit-Bird K, Southall B, Moline M (2019) Dynamic foraging by Risso's dolphins revealed in four dimensions. *Mar Ecol Prog Ser* 632:221–234. doi: [10.3354/meps13157](https://doi.org/10.3354/meps13157)
- Brasnett B (2008) The impact of satellite retrievals in a global sea-surface-temperature analysis. *Quarterly Journal of the Royal Meteorological Society* 134:1745–1760. doi: [10.1002/qj.319](https://doi.org/10.1002/qj.319)
- Buckland ST, Anderson DR, Burnham KP, Laake JL, Borchers DL, Thomas L (2001) *Introduction to Distance Sampling: Estimating Abundance of Biological Populations*. Oxford University Press, Oxford, UK
- Burt ML, Borchers DL, Jenkins KJ, Marques TA (2014) Using mark-recapture distance sampling methods on line transect surveys. *Methods in Ecology and Evolution* 5:1180–1191. doi: [10.1111/2041-210X.12294](https://doi.org/10.1111/2041-210X.12294)
- Canada Meteorological Center (2012) GHRSST Level 4 CMC0.2deg Global Foundation Sea Surface Temperature Analysis Version 2.0. PODAAC, CA, USA. doi: [10.5067/GHCMC-4FM02](https://doi.org/10.5067/GHCMC-4FM02)
- Canada Meteorological Center (2016) GHRSST Level 4 CMC0.1deg Global Foundation Sea Surface Temperature Analysis Version 3.0. PODAAC, CA, USA. doi: [10.5067/GHCMC-4FM03](https://doi.org/10.5067/GHCMC-4FM03)
- Cañadas A, Roberts JJ, Yack TM, Halpin PN (2021) Development of Exploratory Marine Species Density Models in the NAVEUR/C6F Study Area. Report prepared for Naval Facilities Engineering Command, Atlantic under Contract No. N62470-15-D-8006, Task Order 18F4048. Duke University Marine Geospatial Ecology Lab, Durham, NC
- Canny JF (1986) A computational approach to edge detection. *IEEE Transactions on Pattern Analysis and Machine Intelligence* 8:679–698. doi: [10.1016/B978-0-08-051581-6.50024-6](https://doi.org/10.1016/B978-0-08-051581-6.50024-6)
- Carretta JV, Lowry MS, Stinchcomb CE, Lynn MS, E. CR (2000) Distribution and abundance of marine mammals at San Clemente Island and surrounding offshore waters: Results from aerial and ground surveys in 1998 and 1999. NOAA Administrative Report LJ-00-02. NOAA National Marine Fisheries Service, Southwest Fisheries Center, La Jolla, CA
- Chassignet E, Hurlburt H, Metzger EJ, Smedstad O, Cummings J, Halliwell G, Bleck R, Baraille R, Wallcraft A, Lozano C, Tolman H, Srinivasan A, Hankin S, Cornillon P, Weisberg R, Barth A, He R, Werner F, Wilkin J (2009) US GODAE: Global Ocean Prediction with the HYbrid Coordinate Ocean Model (HYCOM). *Oceanog* 22:64–75. doi: [10.5670/oceanog.2009.39](https://doi.org/10.5670/oceanog.2009.39)
- Chelton DB, Schlax MG, Samelson RM (2011) Global observations of nonlinear mesoscale eddies. *Progress in Oceanography* 91:167–216. doi: [10.1016/j.pocean.2011.01.002](https://doi.org/10.1016/j.pocean.2011.01.002)
- Cohen RE, Frasier KE, Baumann-Pickering S, Wiggins SM, Rafter MA, Baggett LM, Hildebrand JA (2022) Identification of western North Atlantic odontocete echolocation click types using machine learning and spatiotemporal correlates. *PLoS ONE* 17:e0264988. doi: [10.1371/journal.pone.0264988](https://doi.org/10.1371/journal.pone.0264988)

- Cole T, Gerrior P, Merrick RL (2007) [Methodologies of the NOAA National Marine Fisheries Service Aerial Survey Program for Right Whales \(*Eubalaena glacialis*\) in the Northeast U.S., 1998-2006](#). U.S. Department of Commerce, Woods Hole, MA
- Cotter MP (2019) Aerial Surveys for Protected Marine Species in the Norfolk Canyon Region: 2018–2019 Final Report. HDR, Inc., Virginia Beach, VA
- Foley HJ, Paxton CGM, McAlarney RJ, Pabst DA, Read AJ (2019) Occurrence, Distribution, and Density of Protected Species in the Jacksonville, Florida, Atlantic Fleet Training and Testing (AFTT) Study Area. Duke University Marine Lab, Beaufort, NC
- Garrison LP (2020) [Abundance of cetaceans along the southeast U.S. East coast from a summer 2016 vessel survey. PRD Contribution # PRD-2020-04](#). NOAA National Marine Fisheries Service, Southeast Fisheries Science Center, Miami, FL
- Garrison LP, Martinez A, Maze-Foley K (2010) [Habitat and abundance of cetaceans in Atlantic Ocean continental slope waters off the eastern USA](#). Journal of Cetacean Research and Management 11:267–277.
- Geo-Marine, Inc. (2010) [New Jersey Department of Environmental Protection Baseline Studies Final Report Volume III: Marine Mammal and Sea Turtle Studies](#). Geo-Marine, Inc., Plano, TX
- Hamazaki T (2002) [Spatiotemporal prediction models of cetacean habitats in the mid-western North Atlantic ocean \(from Cape Hatteras, North Carolina, USA to Nova Scotia, Canada\)](#). Marine Mammal Science 18:920–939.
- Harris PT, Macmillan-Lawler M, Rupp J, Baker EK (2014) Geomorphology of the oceans. Marine Geology 352:4–24. doi: [10.1016/j.margeo.2014.01.011](#)
- Hayes SA, Josephson E, Maze-Foley K, Rosel PE, Wallace J, Brossard A, Chavez-Rosales S, Cole TVN, Garrison LP, Hatch J, Henry A, Horstman SC, Litz J, Lyssikatos MC, Mullin KD, Murray K, Orphanides C, Ortega-Ortiz J, Pace RM, Palka DL, Powell J, Rappucci G, Soldevilla M, Wenzel FW (2022) [US Atlantic and Gulf of Mexico Marine Mammal Stock Assessments 2021](#). NOAA National Marine Fisheries Service, Northeast Fisheries Science Center, Woods Hole, MA
- Jefferson TA, Weir CR, Anderson RC, Ballance LT, Kenney RD, Kiszka JJ (2014) Global distribution of Risso’s dolphin *Grampus griseus*: A review and critical evaluation. Mammal Review 44:56–68. doi: [10.1111/mam.12008](#)
- Laake JL, Calambokidis J, Osmek SD, Rugh DJ (1997) Probability of Detecting Harbor Porpoise From Aerial Surveys: Estimating $g(0)$. Journal of Wildlife Management 61:63–75. doi: [10.2307/3802415](#)
- Lawson JW, Gosselin J-F (2018) Estimates of cetacean abundance from the 2016 NAISS aerial surveys of eastern Canadian waters, with a comparison to estimates from the 2007 TNASS. NAMMCO SC/25/AE/09. In: Proceedings of the NAMMCO 25th Scientific Committee (SC). North Atlantic Marine Mammal Commission, Bergen-Tromsø, Norway,
- Lehodey P, Senina I, Murtugudde R (2008) A spatial ecosystem and populations dynamics model (SEAPODYM)–Modeling of tuna and tuna-like populations. Progress in Oceanography 78:304–318. doi: [10.1016/j.pocean.2008.06.004](#)
- Lehodey P, Conchon A, Senina I, Domokos R, Calmettes B, Jouanno J, Hernandez O, Kloser R (2015) Optimization of a micronekton model with acoustic data. ICES Journal of Marine Science 72:1399–1412. doi: [10.1093/icesjms/fsu233](#)
- Leiter S, Stone K, Thompson J, Accardo C, Wikgren B, Zani M, Cole T, Kenney R, Mayo C, Kraus S (2017) North Atlantic right whale *Eubalaena glacialis* occurrence in offshore wind energy areas near Massachusetts and Rhode Island, USA. Endang Species Res 34:45–59. doi: [10.3354/esr00827](#)
- Mallette SD, Lockhart GG, McAlarney RJ, Cummings EW, McLellan WA, Pabst DA, Barco SG (2014) Documenting Whale Migration off Virginia’s Coast for Use in Marine Spatial Planning: Aerial and Vessel Surveys in the Proximity of the Virginia Wind Energy Area (VA WEA), VAQF Scientific Report 2014-08. Virginia Aquarium & Marine Science Center Foundation, Virginia Beach, VA
- Mallette SD, Lockhart GG, McAlarney RJ, Cummings EW, McLellan WA, Pabst DA, Barco SG (2015) Documenting Whale Migration off Virginia’s Coast for Use in Marine Spatial Planning: Aerial Surveys in the Proximity of the Virginia Wind Energy Area (VA WEA) Survey/Reporting Period: May 2014 - December 2014, VAQF Scientific Report 2015-02. Virginia Aquarium & Marine Science Center Foundation, Virginia Beach, VA
- Mallette SD, McAlarney RJ, Lockhart GG, Cummings EW, Pabst DA, McLellan WA, Barco SG (2017) [Aerial Survey Baseline Monitoring in the Continental Shelf Region of the VACAPES OPAREA: 2016 Annual Progress Report](#). Virginia Aquarium & Marine Science Center Foundation, Virginia Beach, VA
- Marsh H, Sinclair DF (1989) Correcting for Visibility Bias in Strip Transect Aerial Surveys of Aquatic Fauna. The Journal of Wildlife Management 53:1017. doi: [10.2307/3809604](#)
- McAlarney R, Cummings E, McLellan W, Pabst A (2018) Aerial Surveys for Protected Marine Species in the Norfolk Canyon Region: 2017 Annual Progress Report. University of North Carolina Wilmington, Wilmington, NC

- McLellan WA, McAlarney RJ, Cummings EW, Read AJ, Paxton CGM, Bell JT, Pabst DA (2018) Distribution and abundance of beaked whales (Family Ziphiidae) Off Cape Hatteras, North Carolina, U.S.A. *Marine Mammal Science*. doi: [10.1111/mms.12500](https://doi.org/10.1111/mms.12500)
- Meissner T, Wentz FJ, Scott J, Vazquez-Cuervo J (2016) Sensitivity of Ocean Surface Salinity Measurements From Spaceborne L-Band Radiometers to Ancillary Sea Surface Temperature. *IEEE Trans Geosci Remote Sensing* 54:7105–7111. doi: [10.1109/TGRS.2016.2596100](https://doi.org/10.1109/TGRS.2016.2596100)
- Mesgaran MB, Cousens RD, Webber BL (2014) Here be dragons: A tool for quantifying novelty due to covariate range and correlation change when projecting species distribution models. *Diversity Distrib* 20:1147–1159. doi: [10.1111/ddi.12209](https://doi.org/10.1111/ddi.12209)
- Miller DL, Becker EA, Forney KA, Roberts JJ, Cañadas A, Schick RS (2022) Estimating uncertainty in density surface models. *PeerJ* 10:e13950. doi: [10.7717/peerj.13950](https://doi.org/10.7717/peerj.13950)
- Mullin KD, Fulling GL (2003) [Abundance of cetaceans in the southern U.S. North Atlantic Ocean during summer 1998](#). *Fishery Bulletin* 101:603–613.
- O’Brien O, Pendleton DE, Ganley LC, McKenna KR, Kenney RD, Quintana-Rizzo E, Mayo CA, Kraus SD, Redfern JV (2022) Repatriation of a historical North Atlantic right whale habitat during an era of rapid climate change. *Sci Rep* 12:12407. doi: [10.1038/s41598-022-16200-8](https://doi.org/10.1038/s41598-022-16200-8)
- Palka D (2020) [Cetacean Abundance in the US Northwestern Atlantic Ocean Summer 2016](#). *Northeast Fish Sci Cent Ref Doc. 20-05*. NOAA National Marine Fisheries Service, Northeast Fisheries Science Center, Woods Hole, MA
- Palka D, Aichinger Dias L, Broughton E, Chavez-Rosales S, Cholewiak D, Davis G, DeAngelis A, Garrison L, Haas H, Hatch J, Hyde K, Jech M, Josephson E, Mueller-Brennan L, Orphanides C, Pegg N, Sasso C, Sigourney D, Soldevilla M, Walsh H (2021) [Atlantic Marine Assessment Program for Protected Species: FY15 – FY19 \(OCS Study BOEM 2021-051\)](#). U.S. Department of the Interior, Bureau of Ocean Energy Management, Washington, DC
- Palka DL (2006) [Summer abundance estimates of cetaceans in US North Atlantic navy operating areas \(NEFSC Reference Document 06-03\)](#). U.S. Department of Commerce, Northeast Fisheries Science Center, Woods Hole, MA
- Palka DL, Chavez-Rosales S, Josephson E, Cholewiak D, Haas HL, Garrison L, Jones M, Sigourney D, Waring G, Jech M, Broughton E, Soldevilla M, Davis G, DeAngelis A, Sasso CR, Winton MV, Smolowitz RJ, Fay G, LaBrecque E, Leiness JB, Dettloff K, Warden M, Murray K, Orphanides C (2017) [Atlantic Marine Assessment Program for Protected Species: 2010-2014 \(OCS Study BOEM 2017-071\)](#). U.S. Department of the Interior, Bureau of Ocean Energy Management, Washington, DC
- Payne PM (1984) Distribution and density of cetaceans, marine turtles, and seabirds in the shelf waters of the northeastern United States, June 1980 - December 1983, based on shipboard observations. 294.
- Quintana-Rizzo E, Leiter S, Cole T, Hagbloom M, Knowlton A, Nagelkirk P, O’Brien O, Khan C, Henry A, Duley P, Crowe L, Mayo C, Kraus S (2021) Residency, demographics, and movement patterns of North Atlantic right whales *Eubalaena glacialis* in an offshore wind energy development area in southern New England, USA. *Endang Species Res* 45:251–268. doi: [10.3354/esr01137](https://doi.org/10.3354/esr01137)
- Read AJ, Barco S, Bell J, Borchers DL, Burt ML, Cummings EW, Dunn J, Fougères EM, Hazen L, Hodge LEW, Laura A-M, McAlarney RJ, Peter N, Pabst DA, Paxton CGM, Schneider SZ, Urian KW, Waples DM, McLellan WA (2014) [Occurrence, distribution and abundance of cetaceans in Onslow Bay, North Carolina, USA](#). *Journal of Cetacean Research and Management* 14:23–35.
- Redfern JV, Kryc KA, Weiss L, Hodge BC, O’Brien O, Kraus SD, Quintana-Rizzo E, Auster PJ (2021) Opening a Marine Monument to Commercial Fishing Compromises Species Protections. *Front Mar Sci* 8:645314. doi: [10.3389/fmars.2021.645314](https://doi.org/10.3389/fmars.2021.645314)
- Roberts JJ, Best BD, Dunn DC, Trembl EA, Halpin PN (2010) Marine Geospatial Ecology Tools: An integrated framework for ecological geoprocessing with ArcGIS, Python, R, MATLAB, and C++. *Environmental Modelling & Software* 25:1197–1207. doi: [10.1016/j.envsoft.2010.03.029](https://doi.org/10.1016/j.envsoft.2010.03.029)
- Roberts JJ, Best BD, Mannocci L, Fujioka E, Halpin PN, Palka DL, Garrison LP, Mullin KD, Cole TVN, Khan CB, McLellan WA, Pabst DA, Lockhart GG (2016) Habitat-based cetacean density models for the U.S. Atlantic and Gulf of Mexico. *Scientific Reports* 6:22615. doi: [10.1038/srep22615](https://doi.org/10.1038/srep22615)
- Roberts JJ, Mannocci L, Halpin PN (2017) Final Project Report: Marine Species Density Data Gap Assessments and Update for the AFTT Study Area, 2016-2017 (Opt. Year 1), Document Version 1.4. Duke University Marine Geospatial Ecology Lab, Durham, NC
- Roberts JJ, Yack TM, Halpin PN (2023) Marine mammal density models for the U.S. Navy Atlantic Fleet Training and Testing (AFTT) study area for the Phase IV Navy Marine Species Density Database (NMSDD), Document Version 1.3. Duke University Marine Geospatial Ecology Lab, Durham, NC

- Robertson FC, Koski WR, Brandon JR, Thomas TA, Trites AW (2015) [Correction factors account for the availability of bowhead whales exposed to seismic operations in the Beaufort Sea](#). *Journal of Cetacean Research and Management* 15:35–44.
- Ryan C, Boisseau O, Cucknell A, Romagosa M, Moscrop A, McLanaghan R (2013) [Final report for trans-Atlantic research passages between the UK and USA via the Azores and Iceland, conducted from R/V Song of the Whale 26 March to 28 September 2012](#). Marine Conservation Research International, Essex, UK
- Schlax MG, Chelton DB (2016) [The "Growing Method" of Eddy Identification and Tracking in Two and Three Dimensions](#). College of Earth, Ocean and Atmospheric Sciences, Oregon State University, Corvallis, OR
- Stone KM, Leiter SM, Kenney RD, Wikgren BC, Thompson JL, Taylor JKD, Kraus SD (2017) Distribution and abundance of cetaceans in a wind energy development area offshore of Massachusetts and Rhode Island. *J Coast Conserv* 21:527–543. doi: [10.1007/s11852-017-0526-4](#)
- Waring GT, Fairfield CP, Ruhsam CM, Sano M (1992) Cetaceans associated with Gulf Stream features off the northeastern USA shelf. *ICES Marine Mammals Comm* CM 29.
- Waring GT, Fairfield CP, Ruhsam CM, Sano M (1993) Sperm whales associated with Gulf Stream features off the northeastern USA shelf. *Fisheries Oceanography* 2:101–105. doi: [10.1111/j.1365-2419.1993.tb00126.x](#)
- Whitt AD, Powell JA, Richardson AG, Bosyk JR (2015) [Abundance and distribution of marine mammals in nearshore waters off New Jersey, USA](#). *Journal of Cetacean Research and Management* 15:45–59.
- Winn HE (1982) CeTAP: A Characterization of Marine Mammals and Turtles in the Mid- and North Atlantic Areas of the U.S. Outer Continental Shelf: Final Report. University of Rhode Island Graduate School of Oceanography, Kingston, RI
- Wood SN (2011) Fast stable restricted maximum likelihood and marginal likelihood estimation of semiparametric generalized linear models. *Journal of the Royal Statistical Society: Series B (Statistical Methodology)* 73:3–36. doi: [10.1111/j.1467-9868.2010.00749.x](#)
- Zoidis AM, Lomac-MacNair KS, Ireland DS, Rickard ME, McKown KA, Schlesinger MD (2021) Distribution and density of six large whale species in the New York Bight from monthly aerial surveys 2017 to 2020. *Continental Shelf Research* 230:104572. doi: [10.1016/j.csr.2021.104572](#)